Title	Optical Properties of Rare-Earth-Doped Y3Al5012 Single-Crystals Grown by a Floating Zone Method and Transparent Ceramics
Author(s)	関田, 正實
Citation	大阪大学, 1993, 博士論文
Version Type	VoR
URL	https://doi.org/10.11501/3065992
rights	
Note	

Optical Properties of Rare-Earth-Doped $Y_3Al_5O_{12}$ Single-Crystals Grown by a Floating Zone Method and Transparent Ceramics

by

Masami Sekita

Dissertation in Physics
(Osaka University)

1992

CONTENTS

Page

List of Tables **Page**

List of Figures Page

Abstract

Optical properties have been investigated on Nd-ion doped $Y_3Al_5O_{12}$ single crystals grown by a floating zone method using an optical image furnace and undoped and rare-earth-doped transparent $Y_3Al_5O_{12}$ ceramics prepared by a urea precipitation method, which are new techniques developed in recent years.

We have measured for the first time optical spectra and emission lifetimes of the $Nd:Y_3Al_5O_{12}$ single crystals grown by the floating zone method and the transparent $Nd:Y_3Al_5O_{12}$ ceramics. In both cases, crystal-strain may affect the spectroscopic properties and the energy-level structures of Nd^{3+} ion. However, it is found that those are almost the same as in the case of single crystals grown by the Czochralski method.

From decomposition of the absorption and emission spectra, induced emission cross sections are calculated to be 5.3, 7.0, and 7.5 X 10^{-19} cm^2 for the single crystals and 4.9 X 10^{-19} cm^2 for the transparent ceramic $Nd:Y_3Al_5O_{12}$, respectively. These values are found to be comparable to those reported so far for the single crystals grown by the Czochralski method. A concentration quenching phenomenon is observed in the concentration dependence of the emission lifetimes at the 1064-nm laser wavelength for the transparent $Nd:Y_3Al_5O_{12}$ ceramics. The lifetime of the ceramics is 219 μs for 1 at.% Nd ion concentration, whose value is slightly smaller than the reported values of 226-257 μs for the single crystals.

Undoped and rare-earth-(Pr, Nd, Eu, and Er) doped transparent $Y_3Al_5O_{12}$ ceramics have been prepared under improved synthetic conditions, and their optical spectra have been measured. It is found that absorption coefficient of the undoped ceramic $Y_3Al_5O_{12}$ is 0.258 cm^{-1} and almost independent of wavelength, which gives transmittance to be, for example, 97.5 % for a disk of 1 mm thickness. Peaks in the absorption and emission spectra of Pr-doped $Y_3Al_5O_{12}$ are assigned to the transitions in $4f^2$ configuration. It is also found that the transitions from the multiplets with total angular momentum J=0 to multiplets with even J momentum are strong as predicted by Judd-Ofelt theory.

Another $Nd:Y_3Al_5O_{12}$ ceramic is also synthesized. Overall and detailed structures of the absorption and emission spectra of the $Nd:Y_3Al_5O_{12}$ ceramic are the same as those of the samples which were synthesized earlier and used for the estimation of the induced emission cross section. However, an absorption coefficient at non-absorbing wavelength by Nd^{3+} ion is reduced from 3.5-4 cm^{-1} to 1.2 cm^{-1} without subtracting Fresnel surface loss. A Stark splitting scheme of Nd^{3+} ion in the ceramic is compared with that reported for the $Nd:Y_3Al_5O_{12}$ single-crystal, and the agreement is found to be fairly good. A simple calculation of population inversion threshold of the $Nd:Y_3Al_5O_{12}$ ceramic reveals that the threshold value is about 25 times larger than that of the single-crystal $Nd:Y_3Al_5O_{12}$ to realize the population inversion.

Absorption and emission peaks of Er-doped $Y_3Al_5O_{12}$ ceramic are assigned to the transitions in $4f^{11}$ configuration. Comparison is also made between measured Stark splitting of Er^{3+} ion in the $Er:Y_3Al_5O_{12}$ ceramic and that of the single crystal, and it is found to be in fair agreement for the Stark splitting scheme between them. The transition energies in the absorption and emission spectra agree well with those reported for the single-crystal $Er:Y_3Al_5O_{12}$ and the other hosts within 30 cm^{-1}.

Peaks in the emission, absorption, and excitation spectra of Eu-doped $Y_3Al_5O_{12}$ ceramic are assigned to the transitions in $4f^6$ configuration. The transition energies are in very good agreement with those of the single-crystal $Eu:Y_3Al_5O_{12}$ within 8 and 3 cm^{-1} for the emission and the absorption and excitation peaks, respectively. Although no broadband is present in the excitation spectrum, a broadband absorption is observed in the absorption spectrum at around 280 nm. Origin of this broad absorption band is discussed in some detail.

The basic optical properties of the rare-earth ions in the transparent $Y_3Al_5O_{12}$ ceramics are found to be almost the same as those of the rare-earth ions in the $Y_3Al_5O_{12}$ single crystals.

Chapter 1. Introduction

Optical properties of trivalent rare-earth (RE^{3+}) ions have attracted much interest of many theoretical and experimental investigators for a long time. This is mainly due to the fact that the absorption and emission spectra of RE^{3+} ions consist of several groups of many sharp lines even in solid state materials. These groups have been assigned to the transitions within the $4f^n$ configurations of RE^{3+} ions which are shielded by the outer $5s^25p^6$ shells. Since chemical properties of RE ions, however, are very close to each other, the techniques of separation and purification of RE ions have been established rather in recent years. Therefore, reliable optical investigations have been carried out within only about these three decades. The recent progress of the optical investigations on the RE^{3+} ions is mainly due to these techniques together with the success of growing single crystals of good optical quality.

Among the RE^{3+} ions, a Nd^{3+} ion has been studied to considerable extent due to the successful laser oscillation of $Nd{:}Y_3Al_5O_{12}$ (Nd:YAG) by Geusic, Marcos, and van Uitert[1] in 1964. Today, the Nd:YAG lasers are used widely in such diverse fields as range finding, resistor trimming, medical operations, laser annealing, etc. Currently, this laser host material is mostly in the form of single crystals which are almost entirely grown by the Czochralski (CZ) method from a melt. This method provides relatively large single crystals of application quality, however, there are some disadvantages with it. For example, an expensive Ir crucible is required, and contamination from it is hardly avoided. Also longer time is necessary to grow large crystals. A floating zone (FZ) method using an optical image furnace has been developed as an alternative technique for growing Nd:YAG single crystals.[2] This method previously proved itself applicable to growth of $Y_3Fe_5O_{12}$ (YIG).[3] Although the single crystals grown by this technique are relatively small (typically 6 mm in diameter and 60 mm in length), it takes far shorter time to prepare single crystals, which is one of the most important advantages, than the time necessary for the growth by the CZ method. Kimura grew Nd:YAG single crystals of optical quality good enough for quality evaluation by the FZ method.[4]

Although the crystals are grown rather close to thermally equilibrium state in the conventional CZ method, the molten zone in the FZ method is approximately 5 mm in length at around the focus point of the ellipsoidal reflector of the furnace. This gives rise to larger temperature gradient at around the molten portion while growing the single crystal. It is conceivable that this larger temperature gradient may introduce thermal crystal-strain, which will affect the electronic structure of the dopant ions through a crystal-field at around the ions, in the grown YAG crystals.

The investigations on translucent or transparent ceramics, which had began with the U.S. Patent on Al_2O_3 by Coble[5] in 1962, had successfully resulted in the laser oscillation of Nd^{3+} ion in Y_2O_3-ThO_2 transparent ceramics by Greskovich and Chernoch[6] in 1973. Since then, a number of ceramics have been reported to be translucent so far, for example, Y_2O_3-ThO_2 ceramics,[6] $(Pb,La)(Zr,Ti)O_3$ (PLZT),[7] etc. Attempts have been made to prepare the YAG ceramics by hot-press[8] and wet chemical methods,[9-12] however, the absorption coefficients of the ceramic YAG were larger than 7 cm^{-1} at visible and near infrared wavelength regions and far from transparent form.[9] Recently, Haneda et al.[13] have developed a urea precipitation method and obtained almost transparent YAG ceramics of which absorption coefficients are 3.5 to 4 cm^{-1}. This technique provides YAG ceramics of high optical quality, and it is fit for large scale production since it requires no special technique. The Nd:YAG ceramics may become possible candidate for replacing Nd:YAG single crystals. They have further successfully reduced the absorption coefficient of Nd:YAG ceramic to 1.2 cm^{-1} and prepared the other rare-earth-doped YAG (RE:YAG) ceramics of similar quality.[14]

The purpose of this work is to make it clear that effects of the crystalline environment on the optical properties of RE^{3+} ions in the Nd:YAG single crystals grown by the FZ method and the transparent RE:YAG ceramics: line energies and linewidths, line shape, transition intensities, deduced energy-level structures and Stark splitting schemes, and concentration quenching phenomenon of Nd^{3+} ion. These properties can be discussed on the basis of the measurements of the static optical spectra and the Nd ion concentration dependence of the transient emission lifetimes. At the same time, the spectra of RE^{3+} ions are so sensitive to the local crystal-filed that we can evaluate the degree of crystallization of the host of Nd:YAG single crystals grown by the FZ method and the grains of RE:YAG ceramics through the analyses of the optical spectra. Another purpose of this study is to calculate an induced emission cross section, which is one of the important parameters to evaluate materials as laser media, of the single-crystal and ceramic YAGs by making use of the equation found by Kushida, Marcos, and Geusic[15].

Almost no optical investigation has been reported so far on the transparent ceramic YAGs doped with RE^{3+} ions nor other optically active ions only except a brief report on the transmission spectrum of the Nd:Y_2O_3-ThO_2.[6] On the Nd:YAG ceramics, we will estimate the threshold value of Nd laser oscillation using simple Fabry-Pérot-type resonator model. Since the Pr^{3+} ion is one of the most sensitive ions to host materials among the RE^{3+} ions, it is suitable for investigation of the crystal-field at around the ion. The Er^{3+} ion gives rise to substantial fine structures in both absorption and emission spectra. The Er^{3+} ion, therefore, seems to be suitable to compare the energy-level structure of a ceramic Er:YAG with that of Er^{3+} in a single-crystal YAG grown by the CZ method. Finally, a broad absorption peak is found at around 280 nm in the absorption spectrum of a Eu:YAG ceramic and the origin of the peak will be discussed in some detail.

In the next chapter, a review of earlier studies is presented on the optical investigations of RE:YAG single crystals together with a brief review on the single crystal growth by the FZ method and the preparation of the translucent or transparent ceramics. Chapter 3 contains the sample preparation techniques and the methods of optical experiments. In chapter 4, we will report the results of experiments and discuss the optical spectra together with the estimation of the induced emission cross section of the single crystals grown by the FZ method and the transparent ceramic Nd:YAGs. In this chapter, the spectral analyses will be also reported on the undoped, Pr-, Nd-, Er-, and Eu-doped ceramic YAGs.

Chapter 2. Historical Review

A garnet has been known for a long time as a group of compounds with a composition of $\{C\}_3[A]_2(D)_3O_{12}$ in the field of earth science. There have been a number of investigations on the garnet from the mineralogical and crystallographic points of view. Since comprehensive results of the investigations on the crystal structure of the garnet are summarized by Tolksdorf[16] in the Landorf-Börnstein series of reference, a review on the structure will not be presented in this chapter. The space group is analyzed to be a simple cubic with Ia3d (O_h^{10}).[16] Rare-earth ions are believed to replace the dodecahedral {C} site with a D_2 point symmetry, however, the site symmetry of the rare-earth ions will be discussed later. Successful laser oscillation reported by Geusic, Marcos, and van Uitert[1] for Nd-doped $Y_3Al_5O_{12}$ and $Y_3Ga_5O_{12}$ had initiated many investigations on not only optical but also the other physical properties of trivalent rare-earth (RE^{3+}) ions in the garnet crystals by a number of investigators. There are so many studies on the RE^{3+} ions in not only $Y_3Al_5O_{12}$ (YAG) but also gallium garnets, e. g., $Gd_3Ga_5O_{12}$, or mixed garnets, e. g., $Y_3(Al,Ga)_5O_{12}$, etc. that a review in section 2.1 will be mainly restricted to the optical investigations on the RE^{3+} ions in the YAG single crystals. We will review the investigations on single crystal growth by a new floating zone (FZ) method and transparent ceramics briefly in section 2.2.

2.1 Investigations on Nd- and rare-earth-doped $Y_3Al_5O_{12}$

Geusic, Marcos, and van Uitert[1] reported the pulsed and continuous laser operation of $Nd:Y_3Al_5O_{12}$ and $Nd:Y_3Ga_5O_{12}$ in 1964 as mentioned earlier. Although a solid state laser was first reported on the $Cr:Al_2O_3$ (ruby) by Maiman in 1960,[17] the Cr^{3+} ion forms a three-level laser system which requires high threshold energy of the laser oscillation with more than 1000 J.[17] The Nd^{3+} ion, however, forms a four-level laser system, in which population inversion can be easily realized since the population of the terminal level of the laser transition is very small at below room temperature. This fact results in far lower threshold energy values as 3.8 and 2.0 J, and 550 and 400 W rms for the pulsed and 60-cps CW laser operations, respectively.[1] This is major reason why the Nd:YAG system has been a subject of the intensive studies as laser materials. To reduce the threshold values, Kiss, and Duncan introduced Cr^{3+} ions in Nd:YAG system and successfully reduced the threshold energy value by a factor of 3.6.[18] This is realized by making use of an energy transfer phenomenon which is another subject of the numerous investigations[19] and will not be reviewed in this section further for the co-activation of Cr^{3+} ion to the Nd:YAG system.

The energy-level structure of RE^{3+} ions in the garnet crystal is one of the most important subject of investigations. Since the spectra of RE^{3+} ions consist of fine structures in the ultra-violet to near-infrared wavelength region, the energy-level structures of RE^{3+} ions in various solids and liquids deduced from the spectra have been studied extensively to establish a crystal-field theory by an operator equivalent method[20-23] until 1960s and by a tensor-operator technique[24-33] from 1960s. The site symmetry of RE^{3+} ions in $Y_3Fe_5O_{12}$ (YIG) was first reported by Geller and Gillo[34] that an Y^{3+} ion, which can be replaced by RE^{3+} ions, occupies the {C} site of the garnet structure with an orthorhombic D_2 (222) symmetry.

Koningstein and Geusic made the crystal-field calculations intensively on Nd^{3+} ion,[28] Eu^{3+} and Tb^{3+} ions,[29] and Er^{3+} ion[30] in YAG by assuming the site of RE^{3+} ions to be the D_2 symmetry. Although Sayetat[35] conducted detailed X-ray experiments later concluding that the site of Tb^{3+} ion is a monoclinic C_2 (2) symmetry in a $Tb_3Fe_5O_{12}$, all crystal-field calculations on the RE^{3+} ions in YAG have been made by assuming the D_2 symmetry as will be described below, and the results of the calculations are satisfactory to reproduce the observed energy-level structures of RE^{3+} ions in YAG to some extent. It is noted that all degeneracy of the multiplets of RE^{3+} ion in the D_2 symmetry is lifted, e. g., the multiplets of Nd^{3+} ion split into maximum $J+1/2$ Stark levels except the Kramers degeneracy. These calculations were based upon a point-charge model employed by Dillon, Jr. and Walker[36] who successfully interpreted ferromagnetic resonance spectra of RE^{3+} ions in YIG.

Their approximation is far simple compared with the crystal-field calculations through the tensor-operator method[37-44] using a parameter-fitting method by a least-mean-square procedure to minimize the standard deviation of the difference between the calculated and observed energy levels of the multiplets of RE^{3+} ions. The tensor-operator method gives rather better agreement; for example, Nekvasil[40] reported better standard deviation with 3.7 cm^{-1} for the Nd:YAG by comparing with the drawings of Koningstein and Geusic.[28] Morrison, Wortman, and Karayianis[41] made the crystal-field calculations on almost all RE^{3+} ions in YAG to obtain the standard deviation from 6.06 to 14.04 cm^{-1}. Although these calculations give better agreement between the calculated and observed energy levels, physical meaning of the parameters, usually expressed by B_{kq} (crystal-field parameters), used in the formula for the crystal-field calculations are not so clear especially for those with rank k=4 and 6. A major disadvantage concerned with the parameter-fitting theory is that it provides no information on the microscopic origin of the crystal-field,[42] e. g., the lack of basis allowing to extrapolate the parameters obtained for a particular RE^{3+} ion in one host garnet to other garnet structures.

On the other hand, a point-charge model employed by Koningstein and Geusic[28] conveys itself rather clear physical meanings. In general, the crystal-field potential of D_2 symmetry contains nine parameters to be adjustable. Among them, Koningstein and Geusic assumed that the crystal-field parameters of B_{20}, B_{22}, B_{40}, B_{44}, B_{60}, and B_{64} are important and those of B_{42}, B_{62}, and B_{66} are negligibly small (that is, the point symmetry of RE^{3+} ion is raised to a tetragonal D_{2d} symmetry). By making use of the operator equivalent constants,[20-22] they solved secular equations for some multiplets to determine the crystal-field parameters B_{kq}'s.[28-30] For example, the parameters with rank k = 2 and 4 of Nd^{3+} ion are determined through the energy levels of the multiplets with J=3/2 and 5/2 for the Nd:YAG to give best overall agreement of the calculated and observed energy levels.[28] Their method has some disadvantages such that the J-mixing effect, which may give better agreement,[45] is not taken into consideration, the wavefunctions are not intermediate-coupling ones which have been used in the later tensor-operator method,[37-44] etc., however, Grünberg et al.[39] confirmed that the simple point-charge model gives surprisingly successful results for the Dy:YAG by the calculations using both the point-charge model and the tensor-operator method in which many corrections such as mentioned above are taken into consideration. Therefore, we will compare the measured Stark splitting scheme of a Nd:YAG and an Er:YAG ceramic with their calculations[28,30] in chapter 4. The reported crystal-field parameters so far for the RE:YAG single crystals are summarized by Hüfner.[43]

The preceding review is concerned with a static interaction between 4f electrons of RE^{3+} ions and the surrounding lattice which gives rise to the crystal-field splitting of the multiplets. Another interaction is dynamic electron-phonon interaction which causes broadening of linewidths (acoustical phonons) observed in the optical spectra, and determines an emission lifetime of excited states (optical phonons). In a number of crystals, very strong emission can be observed from some multiplets of RE^{3+} ions, e. g., the transitions from $^4F_{3/2}$ to $^4I_{11/2}$ multiplets in the Nd:YAG laser. The emission lifetime is almost independent of temperature in many cases, which suggests that the decay of the emission is mainly governed by a radiative transition and a non-radiative transition through emission of multiple optical phonons is not so significant. The temperature dependence of the lifetimes of RE^{3+} ions in ionic crystals such as LaF_3 has been studied extensively. Typical example of the elaborate investigations on linewidths was reported by Yen, Scott, and Schawlow.[46]

Kushida[47] investigated the temperature dependence of the linewidths, line shape, and line energies of the transitions between several multiplets of Nd^{3+} ion in YAG and $Ca_5F(PO_4)_3$ (FAP) in great detail. These quantities are governed by not only the electron-electron and the electron-phonon interactions but also a static crystal-field strain. For laser materials, such quantities as the linewidths, line shape, etc. have significant meanings since these quantities are closely related to a light amplification gain, etc. and are important for evaluating the materials as laser media. From the theoretical considerations,[48] it has been revealed that a direct (one-phonon) and a Raman (two-phonon) process play a dominant role in a homogeneous line broadening and line shifts of the transitions of RE^{3+} ions. The temperature dependent linewidths are expressed by making use of the electron-phonon interaction hamiltonian with up to quadratic term of the crystal-field strain as

$$\Gamma(T) = \Gamma(0) + \Gamma^{D}(T) + \Gamma^{R}(T) , \tag{1}$$

where the first term is a residual width, the second is due to the one-phonon absorption or emission direct process, and the last denotes the Raman two-phonon process. This equation contains three parameters, i. e., two parameters for linear and quadratic coefficients of the strain term and a Debye temperature θ_D in the Raman-process term in the interaction hamiltonian. This expression is based upon a simple Debye model for the phonon distribution which will be described later.

According to Kushida,[47] line broadening mechanisms such that the Raman process gives rise to a Lorentzian line shape (a homogeneous broadening) due to an energy-independent damping factor, although a Gaussian shape (an inhomogeneous broadening) is expected for the mechanisms originated from statistical strains, multiple sites for Nd^{3+} ions, etc. Among three terms of eq. (1), the residual width $\Gamma(0)$ is mainly ascribed to an inhomogeneous strain broadening for the Nd:YAG since the lifetime broadening of Nd^{3+} ions is completely negligible due to the parity-forbidden nature of the transitions within the $4f^n$ configurations. This term is important only in the spectra at lower temperatures. As for the second term of the direct process $\Gamma^{D}(T)$, Kushida reported that it is difficult to explain the temperature dependence of the transitions from and/or to the ground $^4I_{9/2}$ multiplets without the $\Gamma^{D}(T)$ term.[47] This is due to the fact that there are many Stark levels above the lowest ground level within about 300 cm^{-1} which contribute to one-phonon resonance. Although the shapes of most lines measured were reported to be Lorentzian over wide range of the temperature, a peak at around 900 nm is found to be asymmetric with longer tail toward lower energy.[47] Kushida concluded that this asymmetric shape is ascribed to the resonant one-phonon emission due to the direct process.[47] It is noted that Pellegrino and Yen[49] pointed out that the $\Gamma^{D}(T)$ term is important mainly in the lower temperatures and the third term of the Raman process $\Gamma^R(T)$ is dominant for the linewidths at temperatures above about 50 °K. Kushida[47] obtained very good agreement between the theoretical calculations by eq. (1) and observed line broadening together with the line shifts for several transitions between the $^4I_{9/2}$ and $^4I_{11/2}$ and the $^4F_{3/2}$ multiplets of the Nd:YAG over very wide temperature range of 4.2-500 °K. The Debye temperatures thus determined is, e. g., θ_D = 500 °K and 900 °K for the transitions from the lowest ground level to the two Stark levels of $^4F_{3/2}$ multiplet, respectively.[47]

It is noted that actual phonon spectra of the crystals are usually so complex and far from the Debye model of phonon distribution that the Debye temperature θ_D in the theory does not always coincide with the temperature determined through specific-heat measurements. However, the excellent agreement of the Debye model of the temperature dependence of linewidths and line shifts has been obtained for Nd:YAG and Nd:FAP.[47] Pellegrino and Yen[49] derived that the homogeneous linewidths should be proportional to sound velocity v as v^{-5} from the simple Debye model. They carried out extensive experiments to determine the relationship between the homogeneous linewidth and sound velocity at higher temperature considering only Raman process for Nd^{3+} ion in twelve host materials. They found that the linewidths are proportional to $v^{-4.5\pm0.2}$ for the twelve hosts together with the data of Nd:YAG and Nd:FAP[47] by Kushida. Considering the difficulty and uncertainty in determining the sound velocity through the reported values of density, etc., the agreement is excellent between the calculations and experiments. This fact indicates that the simple Debye model of the phonon distribution is valid to explain the thermal behavior of the linewidths.

Among the factors which govern the linewidths, the inhomogeneous broadening mechanism is especially important for evaluating materials as laser media since the inhomogeneous broadening is closely related to the homogeneity of the crystal-field at around RE^{3+} ions. In the Nd:YAG system, the contribution of the crystal-field parameters of B_{20} and B_{22} was reported to be important for the inhomogeneous broadening of the spectral lines due to the fact that these two parameters are extremely sensitive to the exact position of the impurity ion[50] and accordingly to the crystal-strain. Therefore, the line broadening becomes a suitable measure to evaluate our Nd:YAG single crystals and the transparent Nd:YAG ceramics as will be discussed in chapter 4. Also we have to stress that it is indispensable to decompose the optical spectra for obtaining the accurate linewidths in order to discuss the mechanisms which govern the linewidths of the transitions between multiplets of Nd^{3+} ion.

A concentration quenching phenomenon can be frequently observed in fluorescent and laser materials such as emission intensity being not proportional to the impurity concentrations, a decrease in radiative lifetimes at higher impurity concentrations, etc. This phenomenon is not only important in an application of phosphor production but also an interesting subject of the basic physical investigations. The concentration quenching is especially important for the Nd lasers since this degrades performance of the lasers in several ways.[51] First, it decreases efficiency indirectly since the pumping energy absorbed by the Nd^{3+} ions should be kept low in order to minimize the quenching. Secondly, it results in the decrease of total amount of storable energy by increasing the decay rate of the excited Nd^{3+} ions. Third, the emission lifetime decreases with an increase of Nd ion concentrations, which results in an increase of the threshold energy values of laser oscillation. A number of investigations have been reported so far on the concentration quenching of RE^{3+} ions in LaF_3, Y_2O_3, etc.[52-59] This phenomenon is interpreted in terms of nonradiative energy transfer from the Nd^{3+} ion in the excited $^4F_{3/2}$ to the ground $^4I_{9/2}$ multiplets.[51] The nonradiative energy transfer was ascribed to an electric multipole (mainly dipole) interaction by the theory of Förster[60] and Dexter.[61]

Danielmeyer and Blätte[62] proposed three mechanisms for the concentration quenching in the Nd:YAG system by the energy transfer phenomena.[19] First is energy migration by which the excited energy is transferred to the next ion and so on until it is trapped in some lattice imperfection, etc., then the energy is dissipated without emitting photons (nonradiative transition). Second mechanism is cross relaxation by which the excited energy of one ion is transferred, at least in part, to another unexcited ion then it dissipate the energy. The last is Auger-process by which the excited energy of two ions is combined and dissipated through the nonradiative transition. These mechanisms may be valid if the resonant energy transfer is significant in the concentration quenching. In fact, the importance of the energy transfer has been proved by a number of investigators.[52-59] Danielmeyer and Blätte[62] examined these mechanisms based upon their detailed measurements on the optical spectra of Nd:YAG single crystals. They reported surprisingly large energy migration probability with 3×10^6/s and the diffusion length of about 500 A by assuming the electric dipole interaction,[62] which is far larger than the values of the donor-donor energy transfer in Er(1%):LaF_3 with 6.5×10^2/s and 11 A.[19]

On the cross relaxation mechanism, Danielmeyer and Blätte[62] derived an equation for the Nd ion concentration dependence of the radiative lifetimes (concentration quenching in lifetimes) by making use of branching ratios. Judd[63] and Ofelt[64] constructed a theory to calculate the relative emission intensities (branching ratios) for RE^{3+} ions in terms of only three parameters (Judd-Ofelt theory). It has been reported that the branching ratios are successfully interpreted by the Judd-Ofelt theory for the emission of RE^{3+} ions in many single crystals, powder materials, and glasses. The branching ratios of Nd:YAG were reported by Watts[65] and interpreted through the Judd-Ofelt theory by Krupke.[66] As for the Judd-Ofelt theory, we will discuss the theory relevant to a Pr:YAG ceramic later in subsection 4.4.2. The fit is excellent between the calculation and observed curve of the concentration dependence of the lifetimes.[62]

As for the Auger-type mechanism, the cross section for this mechanism becomes comparable to fluorescence cross section only for the dissipation rate of about 10^4/s for one Nd-ion pair.[66] This rate is equivalent to about 1 KJ for pulsed excitation, of which value is far beyond normal pumping limits. Therefore, the Auger-type mechanism can be ruled out for the concentration quenching in Nd:YAG. Thus, Danielmeyer and Blätte[62] concluded that the concentration quenching in the Nd:YAG system is due to the cross relaxation mechanism via $^4I_{15/2}$ multiplet and the energy exchange is ascribed to the electric dipole energy transfer between Nd-ion pair. It is noted that they further discussed rather primitive but excellent material design based upon their results of investigation. If the $^4I_{15/2}$ multiplets were shifted by only 200 cm^{-1} toward higher energy in some materials, the cross relaxation may be ruled out for the concentration quenching.[62] Therefore, deeper doping of Nd^{3+} ion is possible for the materials which may provide higher performance Nd laser. Unfortunately, this has not been realized by the materials available so far.

The value of an induced emission cross section is particularly important since it is essential for evaluating laser-system parameters such as maximum gain, expected maximum power output, optimum mirror transmission, etc. There have been proposed to calculate the induced emission cross section by several methods in the literature.[67-72] The quantitative evaluation of the induced emission cross section of Nd:YAG system was first reported by Neeland and Evtuhov.[68] They calculated the value of the cross section through two methods. First method is to calculate the cross section by measuring the ratios of fluorescent intensities from the upper laser-level to the ground level and to the lower laser-level together with the measurement of the absorption cross section from the ground level. Second is based upon the measurement of the initial state lifetime of the laser-related transition and the determination of the fluorescence branching ratios for the state. Their results for the cross section of Nd:YAG were 2.7×10^{-19} and 3.5×10^{-19} cm^2 by the first and the second method, respectively.[68]

Kushida, Marcos, and Geusic[15] pointed out inaccuracy of the values reported by Neeland and Evtuhov[68] since they did not take into account of the overlap of laser transitions which originate from the two Stark levels of $^4F_{3/2}$ multiplet. Kushida, Marcos, and Geusic also employed these two methods, however, they took into account of such important physical processes as overlap of two transitions at laser wavelength which are indispensable for evaluating the accurate induced emission cross sections.[15] For the first method, they found a useful relationship between the ratio of emission intensities and that of the induced emission cross sections under the assumption of Lorentzian line shape and by making use of the relationship[48] between the Einstein's *A* coefficient and the induced emission cross section as follows;[15]

$$I_R / I_\ell = (\nu_R / \nu_\ell)^3 \sigma_R / \sigma_\ell, \qquad (2)$$

where I denotes the emission intensity, ν is transition energy, and σ the induce emission cross section. By taking into consideration of the overlap of the two transitions from the two Stark levels of $^4F_{3/2}$ multiplet in thermal equilibrium, they also carefully corrected reabsorption for the absorption from the ground to the emitting levels. The value of the induced emission cross section thus determined is 8.8 X 10^{-19} cm^2.[15]

Kushida, Marcos, and Geusic also evaluated the cross section through radiative transition probability determined from the branching ratios and fluorescence lifetime.[15] In this method, the values of the accurate branching ratios are important. The intensity of the emission of fluorescent material is one of the most difficult quantities to measure and determine accurately. Also such approximation is usually employed that the emission from the excited $^4F_{3/2}$ multiplet to $^4I_{15/2}$ multiplet, which is observed in a medium infrared wavelength region, is negligible. Therefore, this method is more or less inaccurate due to the difficulty to determine the accurate branching ratios of Nd:YAG emission. Kushida, Marcos, and Geusic[15] reported the value of the induced emission cross section calculated through this method as 8.9 X 10^{-19} cm^2, whose value agrees quite well with the value obtained by the method using eq. (2). Despite of the excellent agreement of this method, we will evaluate the induced emission cross sections of our Nd:YAG single crystals grown by FZ method and Nd:YAG ceramics by making use of eq. (2) since no approximation is employed for the calculation of the cross section.

We will finally present a brief review of some interesting investigations on the Nd:YAG system. The Nd ion lasers with 1064-nm wavelength have been now commercially available and used widely in many fields. The laser oscillation has been reported at the other wavelengths for the Nd:YAG system. The laser oscillation at 1318 to 1358 nm range was first reported by Deserno, Röss, and Zeidler.[73] The threshold value for the 1318-nm CW oscillation is 1.2 W and mean output is 110 mW while that for the 1064-nm CW laser is as low as 0.35 W and the output is as high as 440 mW.[73] Wallace and Harris[74] reported the laser oscillation at 946 nm with the threshold values for the pulsed oscillation as 14 to 38 J, although the value for the 1064-nm laser is only 2.0 J.[1] The laser at about 1300-nm wavelength range have been studied intensively so far, however, the investigations are still in a progressing stage since this wavelength range is suitable for the application of optical communication.

Kushida and Geusic reported optical refrigeration in the Nd:YAG single crystal for the first time.[75] The fluorescence wavelength is usually shorter than that of the pumping light in an emission process (Stokes shift). If the emission is achieved in shorter wavelength than that of the excitation light (anti-Stokes shift), the material should be cooled by extracting energy from the host material (the optical refrigeration). Kushida and Geusic observed this anti-Stokes fluorescence in the Nd:YAG crystal using intense light from the exciting Nd:YAG laser.[75] By assuming appropriate parameter values and conducting preliminary experiments on the heat leakage, the temperature reduction was predicted by 2.1 °C through theoretical calculations for the optical refrigeration at the atmospheric pressure. They carried out detailed experiments and determined the optical refrigeration of cooling down as about 0.6 °C for 100 W laser pumping power at the atmospheric pressure.[75] This value is about one-fourth of the predicted value and the possible explanations for the difference from the predicted value are due to the reabsorption of the anti-Stokes fluorescence and the nonradiative transition which were neglected in the theoretical calculations.[75] On the nonradiative transition, they concluded that the contribution is as small as 0.5 % in the Nd:YAG system and the fluorescent quantum efficiency is accordingly very close to unity as about 99.5 %. This value of the quantum efficiency will be used in the evaluation of the induced emission cross section in chapter 4.

2.2 Single crystals grown by a floating zone method and transparent ceramics

Oxide laser crystals have been almost entirely grown by the Czochralski (CZ) method from a melt. Attempts for alternative preparations have been made from 1960's by a floating zone (FZ) method[76] and transparent polycrystalline ceramics.[5] Although the crystals are grown from a melt in the CZ method, the single crystals are grown by traveling a melting zone from top to bottom of the raw material rods in the FZ method. In 1960's and 1970's, many methods had been proposed to create the floating zone such as thermally imaged arcs, electron beams, arc plasmas, plasma beams, etc.[77] The advantages and disadvantages of each method were pointed out by Shah and Wills in some detail.[78] In the past decades, however, the furnace for the FZ method employs mainly an ellipsoidal reflector system using a halogen or a Xe arc lamp as a source to create the floating zone in the raw material rod, and the basic system is available commercially in recent years.

Kimura et al. have carried out intensive investigations on single crystal growth by the FZ method using at first a commercially available optical image furnace. Although they successfully grew a single crystal of a peritectic compound YFe_2O_4,[79] many inventions and improvements have been indispensable for the commercially available apparatus to grow single crystals of better quality. Kimura et al. had successfully grown an $Y_3Fe_5O_{12}$ (YIG) single crystal by the FZ method.[3] This crystal may be easier to be grown by the FZ method since the crystal symmetry is simple cubic and efficient absorption of the heating radiation can be expected due to black body color. The quality of the grown crystals are comparable to the conventional flux-grown YIGs, however, the occurrence of foreign phases and voids were still observed in the grown crystals. Since then, they had tried to find the best growth conditions by observing the etching patterns of the grown crystals,[80] the shape of the solid-liquid interface, the variation of Al concentration added to improve the crystal quality, the strains in the grown crystals,[81] the etch pits of the section perpendicular to the growth direction,[82] etc. They found that the control of the solid-liquid interface is the most important factor to grow the YIG single crystal of good quality through these studies.[2,83] A heat reserving cylinder was introduced for this purpose.

As for $Y_3Al_5O_{12}$ (YAG) of the subject material of this study, several investigations have been reported on the single crystal growth of YAG by the FZ method,[84-87] however, it had not been successful to grow the YAG single crystal by the FZ method for a long time. Kimura et al. made detail analyses for the reasons why the YAG single crystal growth could not be successful upon the basis of their investigations and experiences of the other single crystal growth such as YIG, etc. By considering that the reason is mainly due to improper heat flow during the growth, they made further inventions and improvements on the furnace such as a heat reserving cap, a Pt after-heater, etc. and have successfully grown the undoped and Nd-doped YAG single crystals of good optical quality for the first time.[88]

Finally, we will briefly review the history of investigations on transparent or translucent ceramics. A number of ceramics are known to have a transparent or translucent form. The translucent aluminum oxide (Al_2O_3) ceramic was first reported by Coble.[5] At earlier stage of investigations, it was believed that high pressure was indispensable while sintering to produce transparent polycrystalline ceramics since high density was thought to be desirable (a hot-press method). Addition of a small amount of impurities (especially alkaline metal compounds) was found to be effective to obtain translucent ceramics. Benecke, Olson, and Pask obtained an MgO ceramic with about 99.5 % of the theoretical density by the hot-press method using a LiF impurity.[89] Haertling and Land successfully sintered almost transparent $(Pb,La)(Zr,Ti)O_8$ (PLZT) ceramics by the hot-press method.[7] This method has been also applied to ZnO ceramic, however, transparent one could be hardly obtained.[90,91]

At the same time, investigations to produce translucent or transparent ceramics by sintering without using high-pressure had started in 1960's and successfully resulted in the first and only ceramic laser of Y_2O_3-ThO_2 system by Greskovich and Chernoch[6]. Jorgensen and

Anderson[92] studied the sintering of Y_2O_3 ceramics without high-pressure and found that the addition of ThO_2 to Y_2O_3 inhibits grain growth during sintering and allows the sintering process to proceed to theoretical density. Although they used oxides as starting materials, Greskovich and Wood[93] used sulfate and oxalate compounds as starting materials and obtained the Y_2O_3-ThO_2 ceramics whose residual porosity is as low as about 2.5 X 10^{-7}. By this method, Greskovich and Chernoch[6] reported the first ceramic laser of 1 at.% Nd-doped ThO_2(10%)-Y_2O_3(89%) (Nd:NDY) system. Only a few optical properties were reported for the Nd:NDY ceramics.[6] Although fine structures of Nd absorption are partly observed in the transmission spectra of Nd:NDY ceramics, the linewidths of Nd ion absorption of the ceramics are far broader than those of the single-crystal Nd:YAG and nearly equal to those of the ED-2 glass. Also the fluorescence peak of the 1064-nm laser line was found to be rather weak and the most prominent peaks are at around 1075 nm.[6] The threshold values of the laser oscillation was reported as 16, 21, and 30 J (Ref. 6) while those of the single crystal was as low as 2.0 J.[1] The method without using high-pressure has been applied to $MgAl_2O_3$,[94] Al_2O_3,[95] Pb(Zr,Ti)O_3 (PZT),[96,97] etc. to produce transparent ceramics.

As for the YAG ceramics, Gazza and Dutta had pointed out the YAG ceramics as a possibly useful optical ceramic in a patent concerned with the hot-press method.[8] de With et al. studied intensively to synthesize the translucent YAG ceramics.[9-12] However, the absorption coefficient of their YAGs was as large as 7-16 cm^{-1}.[9] In the past decade, investigations have been extensively done to obtain transparent ceramics such as PZT,[8,97] PLZT,[98] YAG,[99] ZnO,[100] MgO,[101] Zn_2TiO_4,[102] etc., in our institute (National Institute for Research in Inorganic Materials, NIRIM). However, the absorption coefficient of YAG ceramics at that stage was more than 15 cm^{-1} and the ceramics were accordingly opaque.[99] Recently, Haneda et al.[13] have developed a urea precipitation method and obtained almost transparent YAG ceramics with absorption coefficient of less than 4 cm^{-1}. This method may provide the YAG ceramics of high optical quality, and it will be described in some detail in the following chapter.

Chapter 3. Experimental Procedure

3.1 Sample preparation

A schematic illustration of the optical image furnace used for growing Nd-doped $Y_3Al_5O_{12}$ (Nd:YAG) single crystals is shown in Fig. 1. In the figure, the heat reserving cylinder and cap and the Pt after-heater are especially important to obtain the single-crystal YAGs of good optical quality in order to prevent the improper heat flow during the crystal-growth and the grown crystal being broken by the thermal strain as reviewed in the preceding chapter. The crystals thus obtained are almost the same in diameter along the growth direction, uniform for the Nd distribution, and have no core which is always observed in the crystals grown by the conventional Czochralski (CZ) method.

Typical growth conditions for the Nd:YAG single crystals were as follows.[88] The starting materials were 99.99% pure Y_2O_3, Al_2O_3, and Nd_2O_3. 1 at.% of Nd_2O_3 on the rare-earth basis was added and well ground. The mixed powders were stuffed into a long rubber tube and pressed under hydrostatic pressure of 1000 kg/cm^2. The rod thus obtained was preheated for about 2 h at 1750 °C. The radiation source for the image furnace was a 10-KW Xe arc lamp. The growth procedures were similar to those reported by Kimura and Shindo,[3] except that the several improvements as describe above were employed for the optical image furnace to reduce a large thermal gradient at around crystal-melt interface[2] and the atmosphere was nitrogen. The growth rate was 1 mm/h. The shaft rotation rates were 40 rpm for the grown crystal side and 25 rpm for the raw material rod side. The typical size of the good optical part of the crystal was 6 mm in diameter and 60 mm in length. For optical measurements, a thin slab of about 1 mm thickness was cut from the rod and both surfaces were polished.

The samples of an undoped and rare-earth-(RE) doped YAG ceramics used in this study were prepared using the urea precipitation method by Haneda et al.[13,14] as described in the preceding chapter. Fine raw powders were obtained for synthesis of the transparent ceramic YAGs through neutralization by the urea for the acid solutions of Y, Al, and doped rare-earths. Although neutralization by the other alkali-solutions was too quick to obtain the fine raw materials, the urea neutralization method was found to control easily the reaction speed by adjusting the solution temperature and the holding time at the temperature, and to be suitable for the fine raw powder formation.

First, 30 *ml* of YCl_3 solution (all concentration is 1.00 mol/*l* for the following solutions), 50 *ml* of $AlCl_3$ solution, and 30 *ml* of $(NH_4)_2SO_4$ (the urea) were well mixed and de-ionized water was added to the solution to obtain a total amount of 1000 *ml* solution. At this stage, the proper amount of YCl_3 solution was replaced by $NdCl_3$ solution corresponding to Nd concentrations of 0.1, 0.2, 0.5, 1.0, 3.0, and 5.0 at.%. In the later preparation, 0.5 at.% of YCl_3 solution was replaced by chloride solutions of Pr, Nd, Eu, and Er in addition to the undoped sample. Next, 72 g urea and colloidal silica (SiO_2) were added, and well dispersed in the solution. The amount of the colloidal silica was 0.030 g and 0.036 g in the first preparation [hereafter former conditions] of Nd:YAG ceramics for evaluation of an induced emission cross section, etc. and in the later preparation [hereafter latter conditions] of RE-(= Pr, Nd, Er, and Eu) doped YAG ceramics for optical measurements, respectively. The purity was 99.99% for all starting materials. It is noted that addition of the silica is indispensable to obtain the transparent YAG ceramics, and the amount of the addition with less than 100 wt. ppm (0.072 g for 1.00 mol) and more than 3 wt.% (21.5 g) makes the ceramics opaque.[13,14]

The temperature of the solution was then raised to 95 °C and kept at the temperature for 2 h; then, the solution was cooled down to room temperature. The precipitated powder was filtrated from the solution, washed, dried, and calcined in air at 1000 °C for 5 h for the former conditions and at 1300 °C for 3 h for the latter conditions, respectively. The powder was isostatically pressed at 2000 kg/cm^2 into disks of 5 mm diameter by 1.5-2 mm thickness. This pressure can be reduced to 600-700 kg/cm^2, which can be easily attained by conventional piston cylinder instruments. It is noted that the pressure is only necessary to produce disks suitable for optical experiments and not essential to prepare a transparent ceramic, although many translucent ceramics have been synthesized using a hot-press method[7,89-91] in which the pressure plays an important role. Finally, the disks were sintered at 1700 °C for 3 h and 5 h in vacuum (10^{-6} Torr) for the former and the latter preparation, respectively. The raising rate of the temperature was 200 °C/h. It is also noted that undoped and RE-doped ceramic YAGs were synthesized simultaneously, however, only Eu-doped YAG was sintered at different time under the same condition in the latter preparation.

Haneda et al.[13,14] stress that the amount of the colloidal silica, the calcined temperature and time, and the final sintering time are especially important to prepare the transparent ceramic YAGs together with the purity of the starting materials. In the former synthetic conditions, absorption coefficient of Nd:YAG ceramics is about 4 cm^{-1} at non-absorbing wavelengths (background absorption) by the Nd^{3+} ion without subtracting loss and scattering factors such as Fresnel surface loss, etc. Under the latter synthetic conditions, however, the background absorption coefficient of the undoped and RE-doped ceramic YAGs has been reduced to far better values with about 1.2 cm^{-1}, although the reduction of the background absorption of the ceramic YAGs is still in a progressing stage.

3.2 Optical measurements

Optical absorption and emission measurements were carried out using a SPEX 1702 single-grating monochromator (0.75-m focal length and 1.1-nm/mm dispersion). Block diagrams of the experimental set up for the absorption and emission measurements are displayed in Figs. 2 and 3, respectively. The absorption spectra were measured using a 50-W halogen lamp as a light source and an HTV R928 photomultiplier tube (PMT) as a detector for 400-850 nm (280-550 nm only for Eu-doped YAG ceramic) wavelength range. A Toshiba VO-51 glass filter, which blocks light at shorter wavelengths than about 510 nm (henceforth called simply a cut glass filter), was placed in front of the entrance slit of the monochromator to eliminate the second-order light of shorter wavelengths while measuring the spectra at longer wavelengths than 600 nm. For near-infrared (IR) absorption spectra, 850-960 nm, a liquid-nitrogen (LN_2) cooled HTV R316 PMT was used as a detector together with an appropriate cut filter.

To measure the emission spectra at visible wavelengths (VIS spectra), a 365-nm line of an Ushio 150-W ultra-high-pressure Hg arc lamp and/or two resonance lines (313- and 365-nm) of Hg from a 150-W Hg-Xe arc lamp (HTV L2482) were used as an excitation source. The 365-nm Hg resonance line was used with a Toshiba UV-D36A glass filter and a 1-cm-thick $CuSO_4$ solution filter for the Nd:YAG single crystals grown by the floating method and the RE:YAG ceramics except the Pr-doped YAG (Pr:YAG) ceramic. The transmission characteristics of these filters are shown in Fig. 4. The 313-nm resonance line was used through two Corning C.S. 7-54 glass and a 1-cm-thick $NiSO_4$ solution filters for the Pr:YAG ceramic, since the emission by the 365-nm excitation was very weak. The transmission characteristics of these filters are displayed in Fig. 5. To prevent the scattered light of the excitation source at the sample surface, a Toshiba UV-39 cut glass filter was placed in front of the entrance slit of the monochromator. Also, the VO-51 cut glass filter was used to eliminate the second-order emission of wavelengths shorter than 500 nm while measuring the spectra from 550 to 700 nm.

To record the IR emission spectra, 640-1400 nm, a multiline Ar-ion laser (ILT 5490A) operating at 95 mW was used as an excitation source. The 1-cm-thick $CuSO_4$ solution filter was also used to prevent the spontaneous emission lines of Ar^+ of the laser at the IR-wavelength region. The IR detector was also the LN_2 cooled HTV R316 PMT and a Toshiba VO-59 cut glass filter was placed at the entrance slit of the monochromator.

Since the absorption of Eu-doped YAG (Eu:YAG) ceramic was very weak, an excitation spectrum was also measured. Block diagram of the experimental set up for the excitation experiment of Eu:YAG ceramic is shown in Fig. 6. Monochromatic light from a 150-W Xe lamp (HTV L2175) through the SPEX monochromator was focused on the sample. The emission of the sample was guided through an optical fiber to a small monochromator (ptr Optics MC1-02 with 74-mm focal length and 7.5-nm/mm dispersion) fixed at 590 nm (emission peak of $^5D_0$ to $^7F_1$ transition of Eu^{3+}

ion) and 610 nm ($^5D_0$ to $^7F_2$ transition) with 1-mm slit widths, and detected by the HTV R928 PMT.

In order to record the transient emission at the laser wavelength (1064 nm), an NRG-0.5-5-150 nitrogen laser, a DL-0.03 dye laser with less than 5-ns pulse width, and a PAR 162/164 analog boxcar integrator and/or an NF BX-531 digital boxcar integrator/averager with less than 100-ps sampling gate width were used in combination for the single crystal and the ceramic YAGs. An ethanol solution of the Rhodamine 6G was used in the dye laser. The detector for the 1064-nm emission was also the LN_2 cooled HTV R316 PMT. Block diagram of the experimental set up for the transient experiments is shown in Fig. 7.

For the emission intensities, a correction for the spectral sensitivity of the measuring system is necessary in order to determine the induced emission cross section as will be discussed in chapter 4. Using a standard lamp with a color temperature of 2856 °K, it was determined that the multiplication factor equals to 58.7 for the laser transition wavelength of 1064 nm. The excitation spectrum of Eu:YAG ceramic was also corrected except the spectral response of R928 PMT at the ultraviolet-wavelength region.

The stability and drift of the light sources were better than 0.3% for the halogen, the Hg-Xe arc, and the Xe arc lamps. Those of the Ar-ion laser were less than 1% for the IR emission measurements. The stability of the ultra-high-pressure Hg lamp and the nitrogen laser was less than a few %. The fluctuation and drift of these light sources were corrected by monitoring the source-intensity using a Si photodiode as shown in Figs. 2, 3, and 6 except the measurements by the nitrogen laser. Together with the on-line corrections during measurements, the data acquisition and averaging and the wavelength scan were done by a micro-computer system. Typical measuring conditions were that the sampling times was 20 times and the sampling was made every 0.1 nm. Typical slit widths were 6 μm for the absorption measurements and 60-90 μm for the emission and excitation experiments. All experiments were done at room temperature.

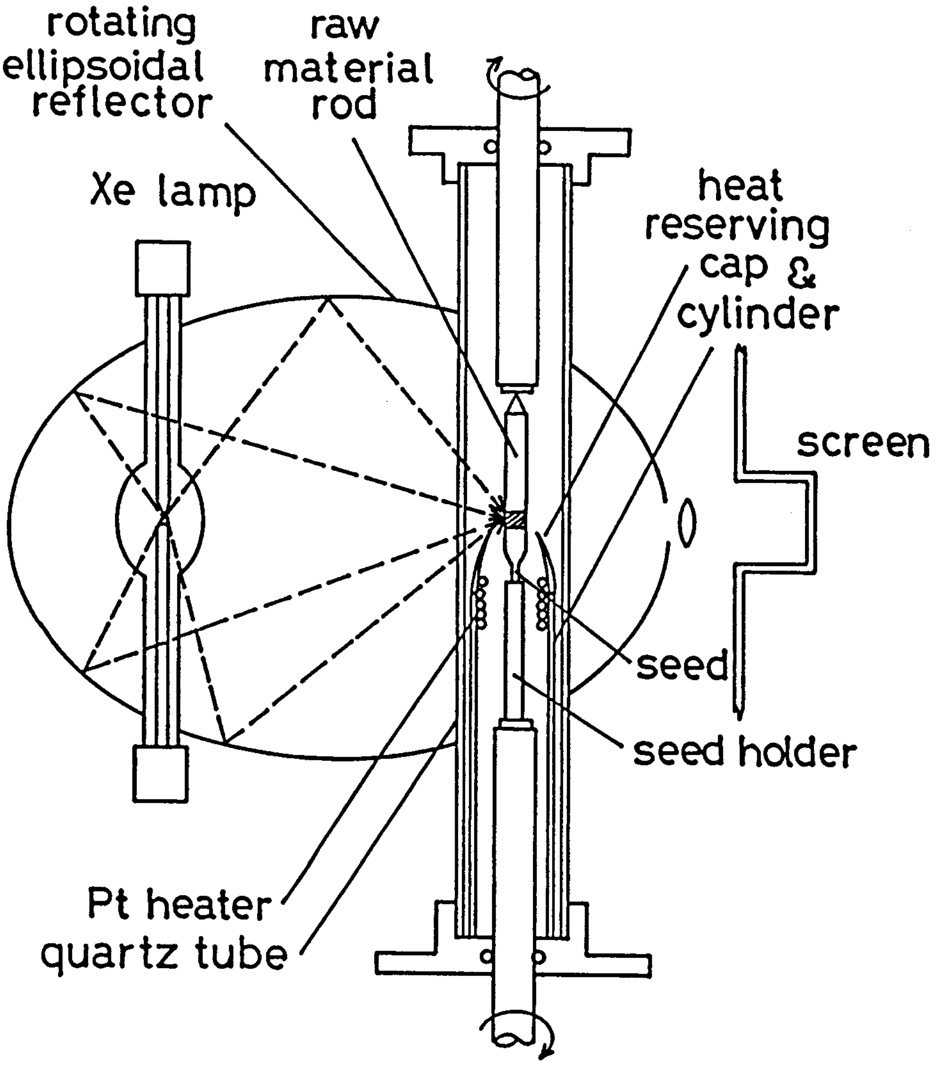

Fig. 1. Schematic illustration of optical image furnace. Shaded part of the rod indicates a molten zone.

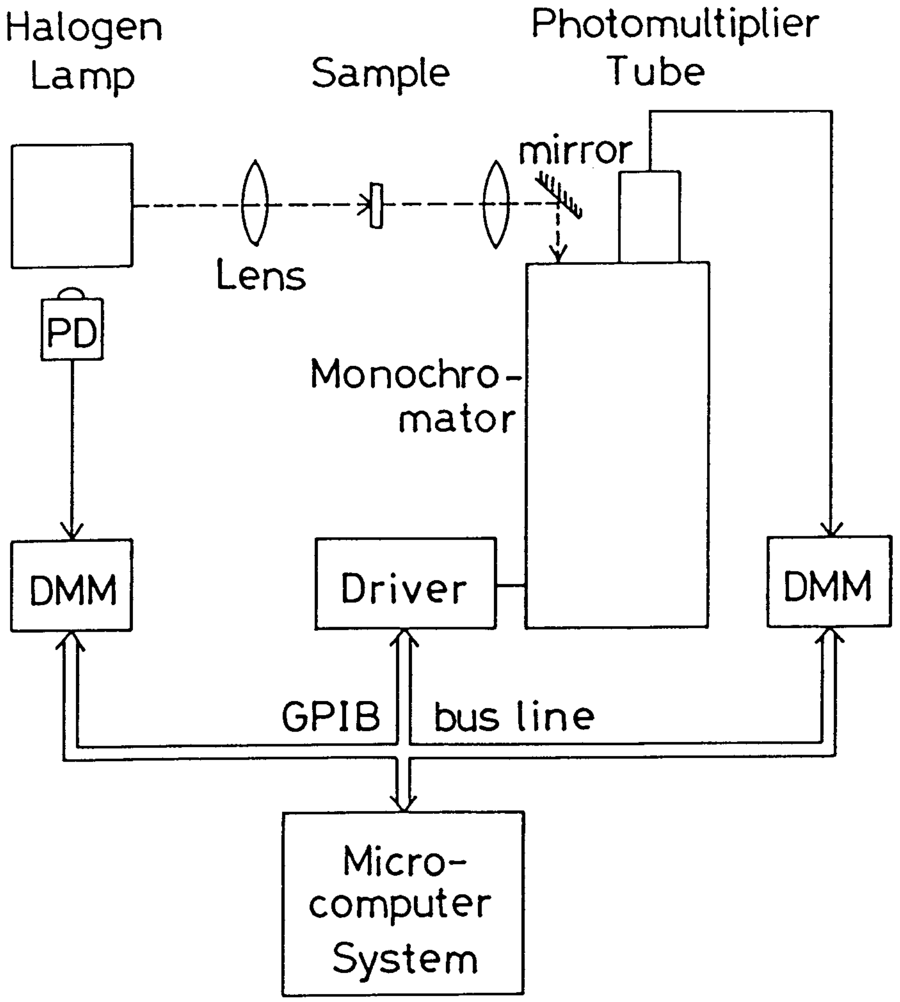

Fig. 2. Block diagram of the experimental set up for absorption measurements.

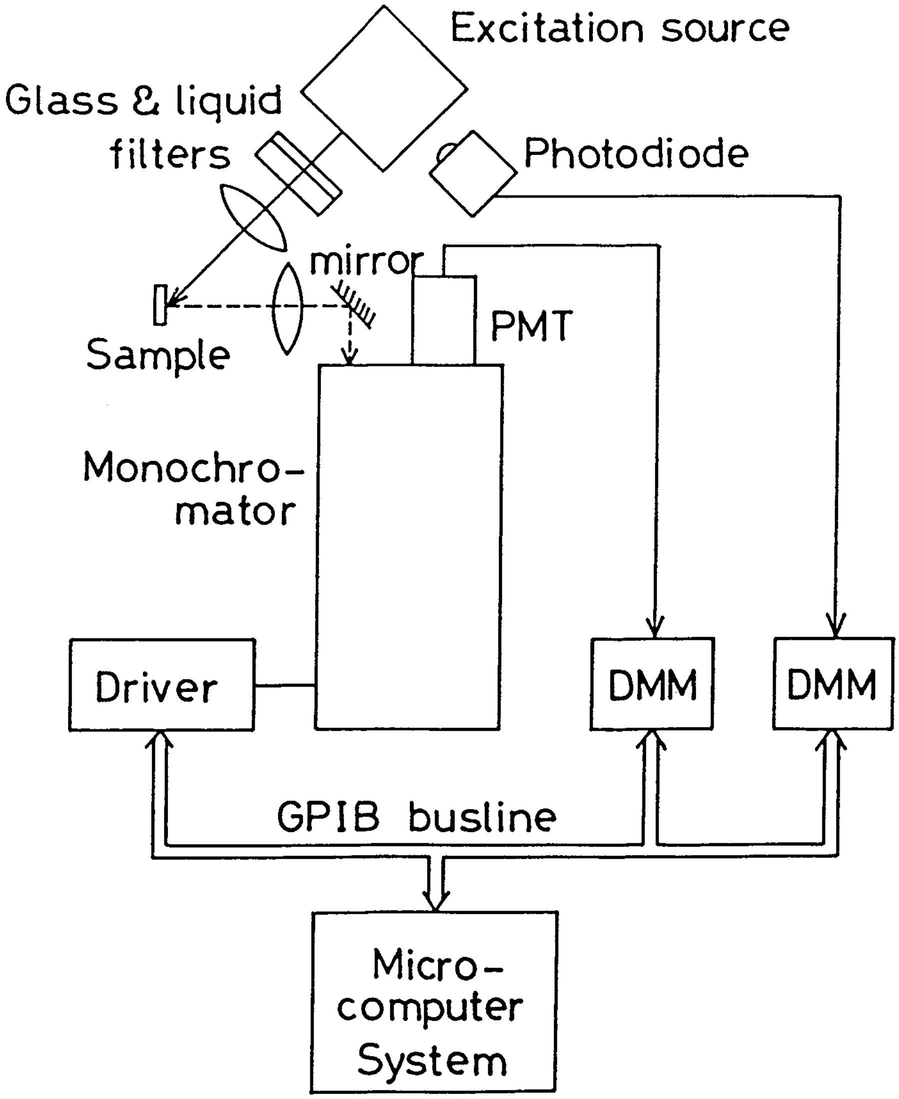

Fig. 3. Block diagram of the experimental set up for emission measurements. DMM denotes a digital multi-meter and PMT is a photomultiplier.

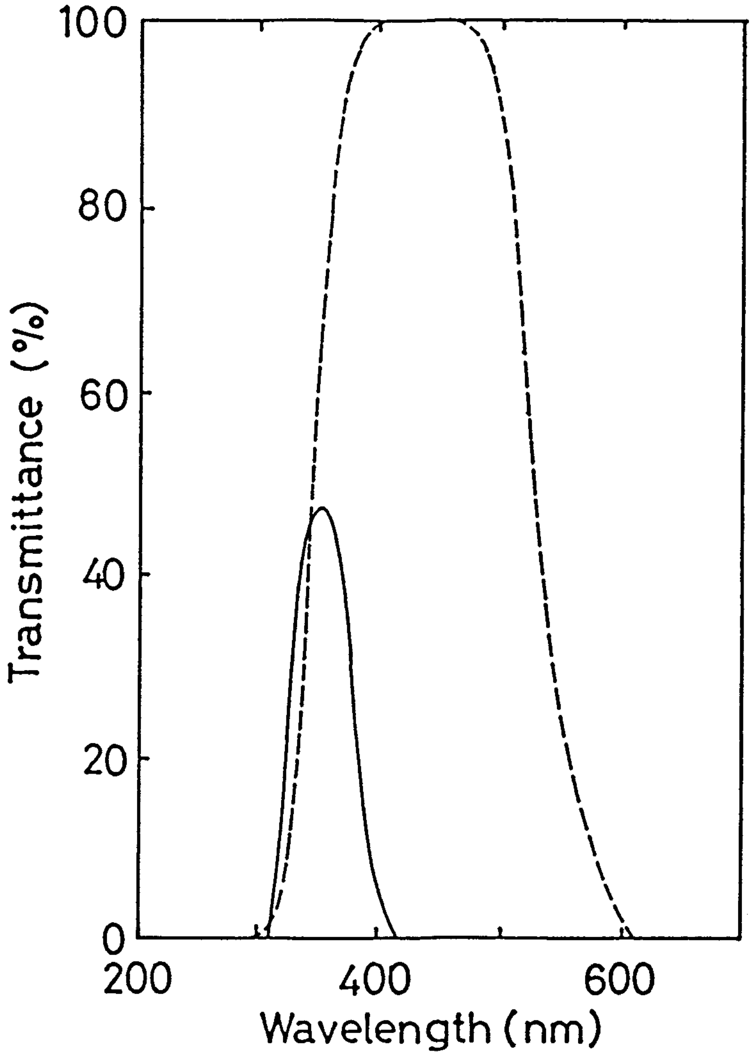

Fig. 4. Transmission characteristics of $CuSO_4$ liquid and UV-D36A glass filters. Broken line denotes the transmission spectrum of $CuSO_4$ and solid line is that of Toshiba UV-D36A glass filter.

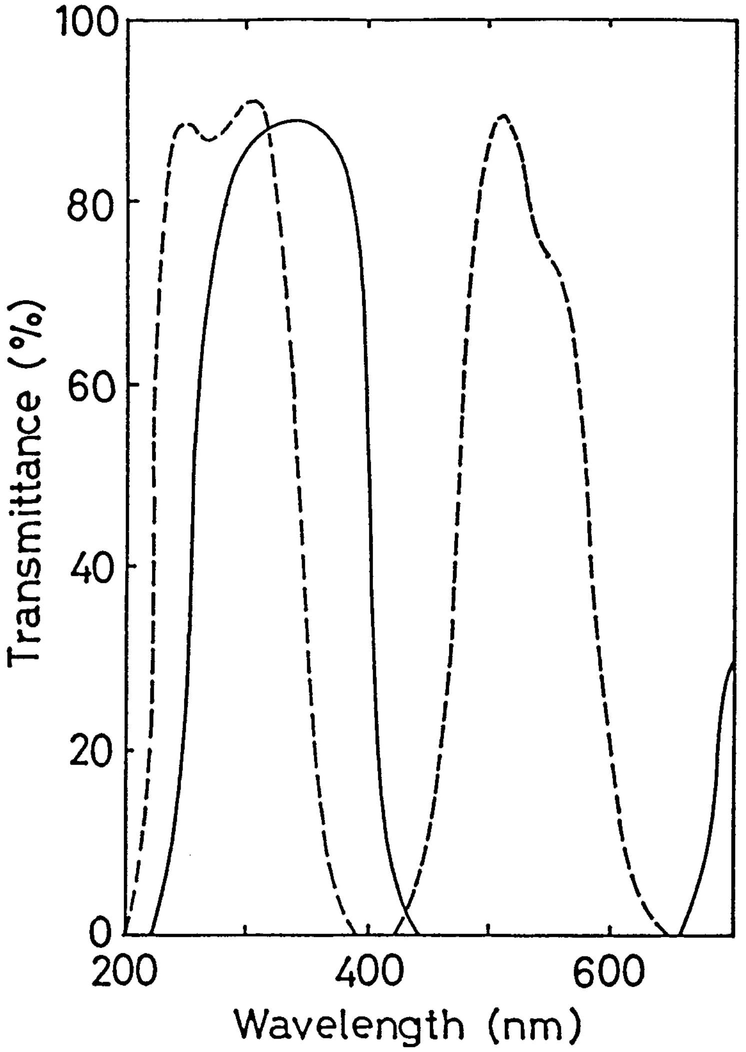

Fig. 5. Transmission characteristics of $NiSO_4$ liquid and C.S. 7-54 glass filters. Broken line denotes the transmission spectrum of $NiSO_4$ and solid line is that of Corning C.S. 7-54 glass filter.

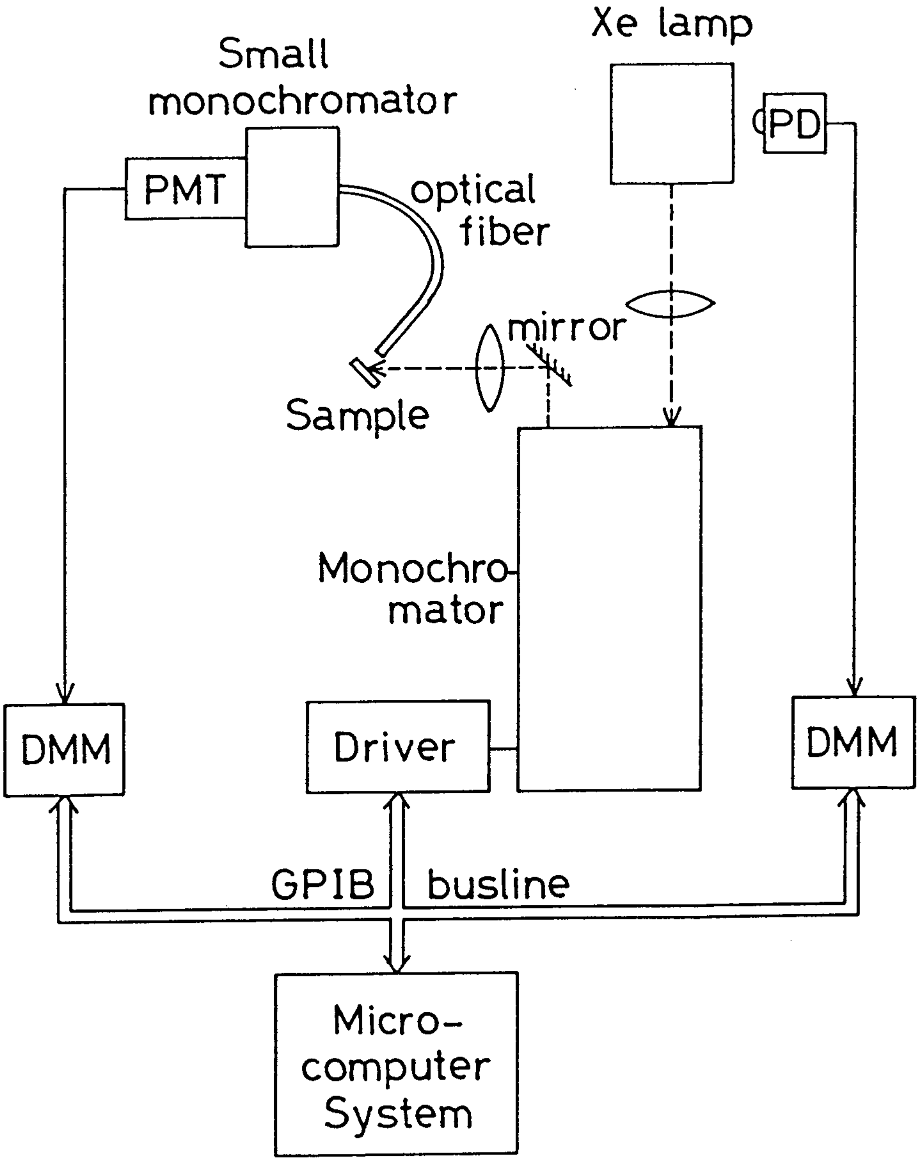

Fig. 6. Block diagram of the experimental set up for excitation measurements. PD denotes a photo-diode, PMT is a photomultiplier tube and DMM is a digital multi-meter.

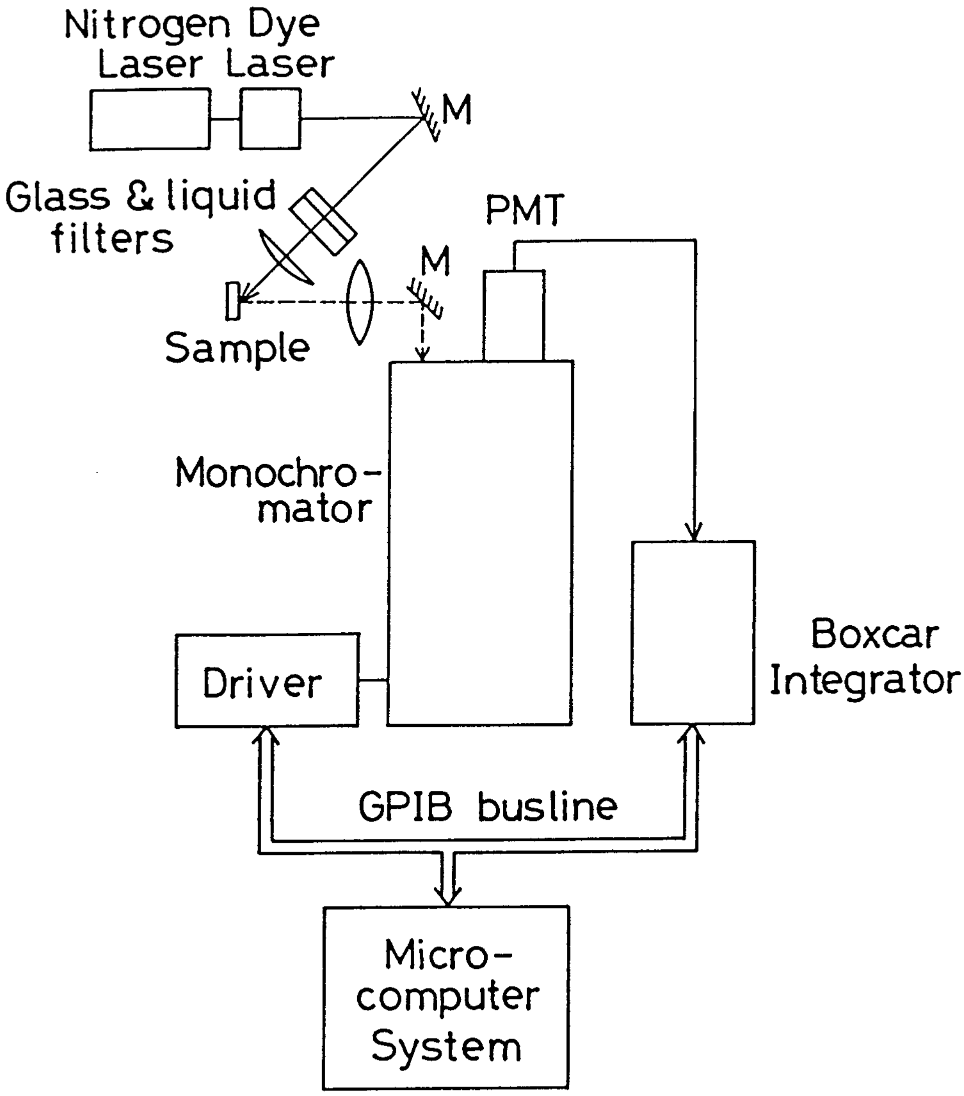

Fig. 7. Block diagram of the experimental set up for transient emission measurements. M denotes a mirror and PMT is a photomultiplier tube.

Chapter 4. Results and Discussion

In this chapter, we will report and discuss optical characteristics of the single crystals grown by the floating zone (FZ) method [hereafter FZ single crystals] and the transparent ceramic Nd:$Y_3Al_5O_{12}$ (Nd:YAG) in sections 4.1 and 4.2, respectively, comparing with the single crystal grown by the conventional Czochralski (CZ) method [hereafter CZ single-crystal]. In section 4.3, the induced emission cross sections of these single crystals and transparent ceramic Nd:YAGs will be evaluated in accordance with the equation found by Kushida, Marcos, and Geusic.[15] Since there has been almost no report on the optical study of rare-earth ions in transparent ceramics so far, we will report and discuss basic optical properties of undoped and rare-earth-(RE) doped transparent ceramic YAGs, of which degree of transparency has been considerably improved than that of Nd:YAG ceramics used for the investigations given in sections 4.2 and 4.3, in some detail in section 4.4.

4.1 Optical spectra of Nd:$Y_3Al_5O_{12}$ single crystals grown by a floating zone method

Among the FZ single crystals, optical measurements were carried out on three samples, namely, no. 0, no. 8, and no. 38 which showed good optical quality under a polarizing microscope. The absorption spectra of no. 8 crystal are shown in Figs. 8-10 for the wavelength region from 400 to 960 nm. In the figures, the multiplets are designated which are the final levels of transitions from $^4I_{9/2}$ ground multiplet. Koningstein and Geusic[28] reported the crystal-field parameters and the transition energies of CZ single-crystal Nd:YAG at 4.2 °K. Our data for the transition energies between multiplets were the same for the three samples and deviated by 0.3-0.5 nm toward longer wavelength from those reported by Koningstein and Geusic.[28] Also slight broadening of the linewidths was observed compared with the values calculated from their figures. This difference is due to the difference in measuring temperature with which the linewidths and line energies changes to some extent through several mechanisms as reviewed in chapter 2. All multiplets observed are split into maximum

J+1/2 Stark levels. This fact indicates that the site symmetry of Nd^{3+} ion is low and consistent with the D_2 point symmetry by which all degeneracy of the multiplets is lifted except the Kramers doublet. Detailed absorption measurements were carried forth for the transitions form $^4I_{9/2}$ to $^4F_{3/2}$ at 11423 cm^{-1} and from $^4I_{9/2}$ to $^4F_{3/2}$ at 11508 cm^{-1}, and the results for the absorption coefficients are given in Table 1.

The emission spectra of the no. 8 sample are shown in Figs. 11 and 12. Since the site symmetry of Nd^{3+} ion is low as mentioned above, the degeneracy is also fully removed in the emission spectra. This fact is clearly shown in Fig. 11, for example, all 10 lines were observed between the two Stark levels of $^4F_{3/2}$ and the five Stark levels of $^4I_{9/2}$ multiplets. The peak emission wavelengths are in good agreement with those reported by Koningstein and Geusic.[28] As will be described in section 4.3, it is necessary to decompose the spectra with considerable accuracy in order to evaluate the induced emission cross section. A program named LSAP (Line Shape Analysis Program) had been developed[103] for the purpose of the decomposition of the spectra with multiple peaks. We will discuss briefly the basic theory for the program by Jennrich and Sampson[104] later in this section. In Figs. 13 and 14, the results of the computer analyses are shown for the decomposition of the emission from $^4F_{3/2}$ to $^4I_{9/2}$ and $^4I_{11/2}$ transitions in the no. 8 sample, respectively. In the figures, the + marks denote the experimental data, and the solid lines are the component and composite spectra. The agreement between the experiments and calculations is good, and the spectra can be well decomposed by a Lorentzian line shape. This fact suggests that the Nd^{3+} ions are incorporated into a single site and the spectral widths are dominated by the homogeneous broadening mechanism.[47] In the figures, ℓ_1 and ℓ_2 denotes the emission peaks which contribute to the 1064-nm laser transition, and R_1 and R_2 are the reference lines which will be used for the evaluation of the induced emission cross section in section 4.3. The results for the three samples are given in Table 1 together with the absorption coefficients (α). The emission intensities are not corrected for the spectral sensitivity of the measuring system in the table.

From the results of the spectral measurements and the decomposition of the spectra, we can construct the energy-level structure of Nd^{3+} ion in the FZ single-crystal YAGs. The result is shown in Fig. 15. The transition numbers in the figure correspond to the peak numbers in Figs. 11 and 12. In the figure, the values in parentheses are the energies of CZ single-crystal reported by Koningstein and Geusic.[28] The energy levels were the same for the three crystals within 1 cm^{-1}, and in good agreement with those reported so far[15,28,42,65,69,105] within 4 cm^{-1}. In the figure, the meanings of the ℓ_1, ℓ_2, R_1, and R_2 are described as above.

Kushida[47] discussed the effect of static crystal-strain on the energy levels of $^4F_{3/2}$ multiplet in the crystal-field calculation by Koningstein and Geusic[28] in some detail. He concluded that the strain gives rise to an increase of the energy of the upper Stark level of $^4F_{3/2}$ multiplet, although the energy of another level of the multiplet will be decreased.[47] Thus, the strain may increase the energy separation between two Stark levels of $^4F_{3/2}$ multiplet. As described in chapter 1, the temperature gradient at around the crystal-melt interface in the FZ method is so larger than the conventional CZ method that the many crystal strains may remain in the FZ single crystals even after enough annealing of the crystals. The crystal-strain may cause the broadening of spectral linewidths through the electron-phonon interaction as reviewed in chapter 2. Also this may result in larger energy separation between two Stark levels of $^4F_{3/2}$ multiplet as mentioned above.[47] However, the observed separation is 85 cm^{-1} for the FZ single-crystal of which value is almost the same as the reported values of 84 cm^{-1} by Kushida[47], 86 cm^{-1} by Singh et al.,[105] and 84 cm^{-1} by Danielmeyer and Blätte[62] for the CZ single-crystal Nd:YAGs. The spectral linewidths of the ℓ_1 and ℓ_2 transitions of CZ single-crystal were reported as $\Delta\nu_{\ell_1} = 4.2$ cm^{-1} and $\Delta\nu_{\ell_2} = 5.2$ cm^{-1}.[15] Our results for the no. 8 sample are given in Table 1 as 4.53 and 4.95 cm^{-1}, respectively. These values are almost the same as those of CZ single-crystal.[15] Therefore, we can conclude that the crystal strains in the FZ single crystals do not affect the optical spectroscopic properties of Nd^{3+} ion in the FZ single-crystal Nd:YAGs.

Another interesting feature in the absorption spectrum is the asymmetric line shape of one line from the lowest ground level of $^4I_{9/2}$ to $^4F_{3/2}$ multiplets. As can be seen in Fig. 13, the number 8 absorption peak in the decomposed spectrum is considerably asymmetric with longer tail on the lower energy side compared with the other peaks which are well decomposed into simple Lorentzian line shape. Kushida reported this fact and discussed the origin of the asymmetric line shape in some detail[47] as reviewed in chapter 2. As discussed by Kushida,[47] we can also ascribe this asymmetry to the direct process term $\Gamma^D(T)$ in the Debye model for the electron-phonon interaction given in eq. (1) since there exist three levels which can contribute to the direct process above the ground level within only about 300 cm^{-1} as can be seen in Fig. 15.

The lifetime at the laser transition wavelength (1064 nm) was measured by excitation using the 0.5 MW nitrogen laser pumped dye laser with 588-nm wavelength at which there is a strong absorption from $^4I_{9/2}$ to $^2G_{7/2}$ and $^2G_{5/2}$ multiplets. The time dependence of the no. 8 sample is shown in Fig. 16. It can be seen from the figure that the emission decay is well expressed by a single exponential function. The values of the lifetime (time for the intensity to reduce to $1/e$ of the initial value) were 244 ± 5 μs, 226 ± 5 μs, and 253 ± 5 μs for the no. 0, no. 8, and no. 38 crystals, respectively. These values fall in the range reported so far from 230 to 257 μs as will be given in later in Table 4. Okamoto, Sekita, and Masui[19] studied the fluorescence decay of Er^{3+} ion in LaF_3 in some detail and found that the emission decays of Er^{3+} ion are considerably deviated from a simple exponential function due to energy migration among the excited states even at far lower concentration than 1 at.% in Er:LaF_3. The fact that the emission decay is well expressed by a single exponential function for the Nd:YAGs indicates that such mechanism as the energy migration does not work in the case of FZ single-crystal Nd(1%):YAGs.

Before closing this section, we will briefly describe the line shape analysis program (as called LSAP earlier) which was indispensable for the decomposition of the emission and absorption spectra of the single-crystal Nd:YAGs and the ceramic Nd:YAGs which will be discussed in the following section. The most commonly used and perhaps most important procedure of the least-mean-square fitting is the Gauss-Newton method which uses the step $\Delta f\ (\theta)$ for the stepwise regression during the fitting as calculated from the partial derivative of each function $f\ (\theta)$ of the error matrix. This step, however, results often in an increase in the residual sum of the differences between the calculated values and experimental data. Jennrich and Sampson[104] improved this Gauss-Newton method by introducing a fraction α ($0 < \alpha \leq 1$) by multiplying the step $\Delta f\ (\theta)$ calculated from the conventional Gauss-Newton method, i. e., $\alpha \cdot \Delta f\ (\theta)$ in place of $\Delta f\ (\theta)$. This factor α is adjusted during the iteration by changing the power n of 2^{-n} within the program.

The program was coded based upon this Jennrich and Sampson's theory.[104] By their method, the least-mean-square fitting calculation has been extremely improved in convergence of the iterations of the calculations. It is also noted that even erroneous initial estimates of the parameters for the program by more than 3 or 4 order of magnitude have resulted in the correct and unique minimum set of the parameters. The LSAP program is applicable to not only the optical spectra but also the other spectra. For example, the application to X-ray photoemission spectra of an alumino-silicate glass[106] has successfully elucidated the bonding state of Si ion in the glass, and the application to Raman spectra of monoclinic pyroxenes[107–109] has revealed for the first time that the Si and Al ions are in ordering state to some extent in the pyroxenes, which has not been able to be elucidated by the other method such as X-ray diffraction, neutron scattering measurements, etc. due to almost equal scattering factor of Al and Si ions.

Table 1. Spectral constants of absorption and emission of transitions between $^4I_{9/2,11/2}$ and $^4F_{3/2}$ multiplets. These values are obtained from the decomposition of the absorption and emission spectra as shown in Fig. 13 and 14. N_0 denotes the Nd concentration, α the absorption and emission coefficients, L the sample thickness, I the peak intensities, ν the central energy of the Lorentzian line shape function and $\Delta\nu$ the full width at half maximum of the peak intensity.

	no. 0	no. 8	no.38
N_0	1.4×10^{20}	1.4×10^{20}	1.4×10^{20}
α_{R_1}	0.83 cm^{-1}	0.74 cm^{-1}	0.93 cm^{-1}
α_{R_2}	2.89 cm^{-1}	2.98 cm^{-1}	2.69 cm^{-1}
L	0.1157 cm	0.3114 cm	0.1256 cm
I_{R_1}	2.38	4.29	4.02
ν_{R_1}	11423 cm^{-1}	11423 cm^{-1}	11423 cm^{-1}
$\Delta\nu_{R_1}$	13.22 cm^{-1}	14.00 cm^{-1}	14.44 cm^{-1}
I_{R_2}	5.05	6.71	6.43
ν_{R_2}	11508 cm^{-1}	11508 cm^{-1}	11508 cm^{-1}
$\Delta\nu_{R_2}$	14.69 cm^{-1}	18.90 cm^{-1}	18.59 cm^{-1}
I_{ℓ_1}	0.351	0.583	0.401
ν_{ℓ_1}	9394 cm^{-1}	9394 cm^{-1}	9394 cm^{-1}
$\Delta\nu_{\ell_1}$	4.73 cm^{-1}	4.53 cm^{-1}	4.80 cm^{-1}
I_{ℓ_2}	1.05	1.61	1.32
ν_{ℓ_2}	9397 cm^{-1}	9397 cm^{-1}	9397 cm^{-1}
$\Delta\nu_{\ell_2}$	5.03 cm^{-1}	4.95 cm^{-1}	5.46 cm^{-1}

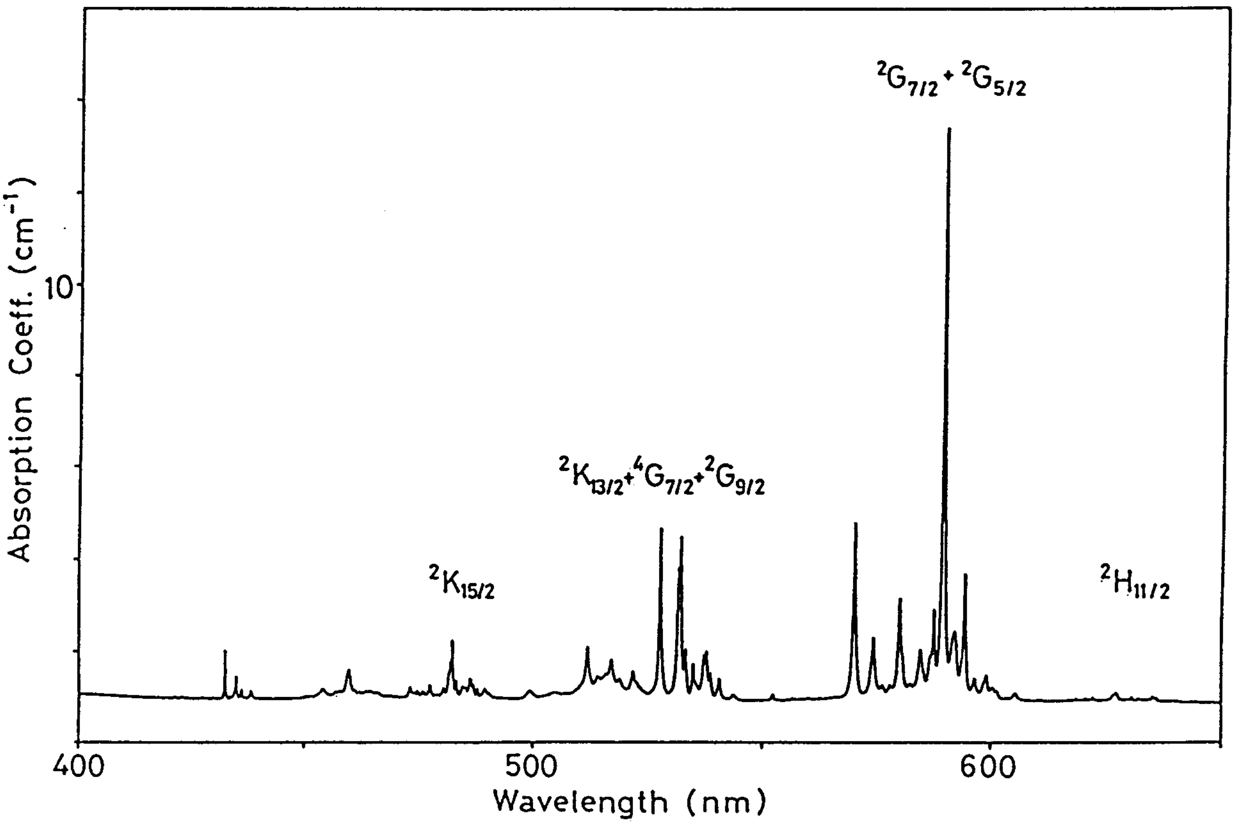

Fig. 8. Absorption spectrum of no. 8 single crystal Nd:YAG between 400 and 650 nm. Multiplets denote the final levels from the ground $^4I_{9/2}$ manifold.

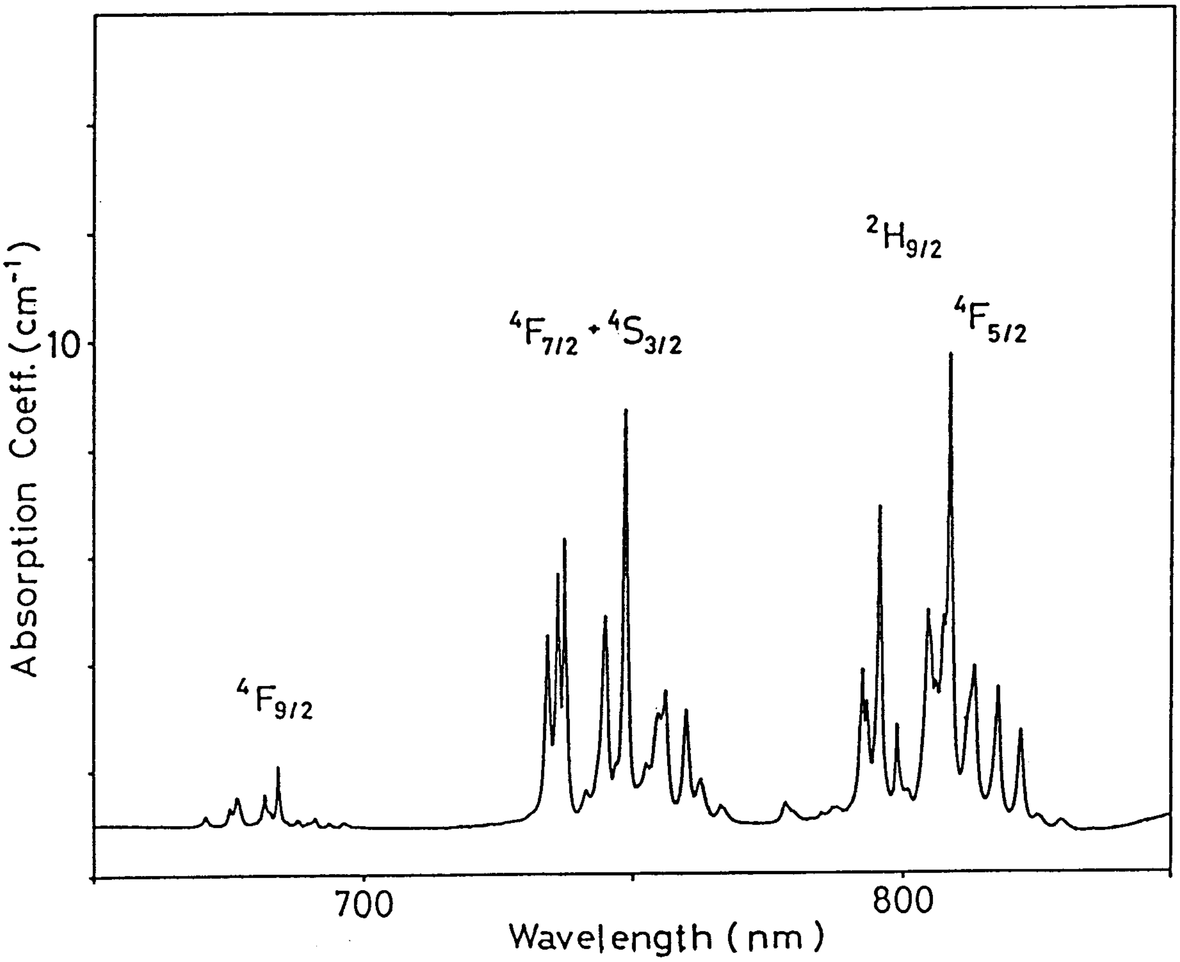

Fig. 9. Absorption spectrum of no. 8 single crystal Nd:YAG between 650 and 850 nm. Multiplets denote the final levels from the ground $^4I_{9/2}$ manifold.

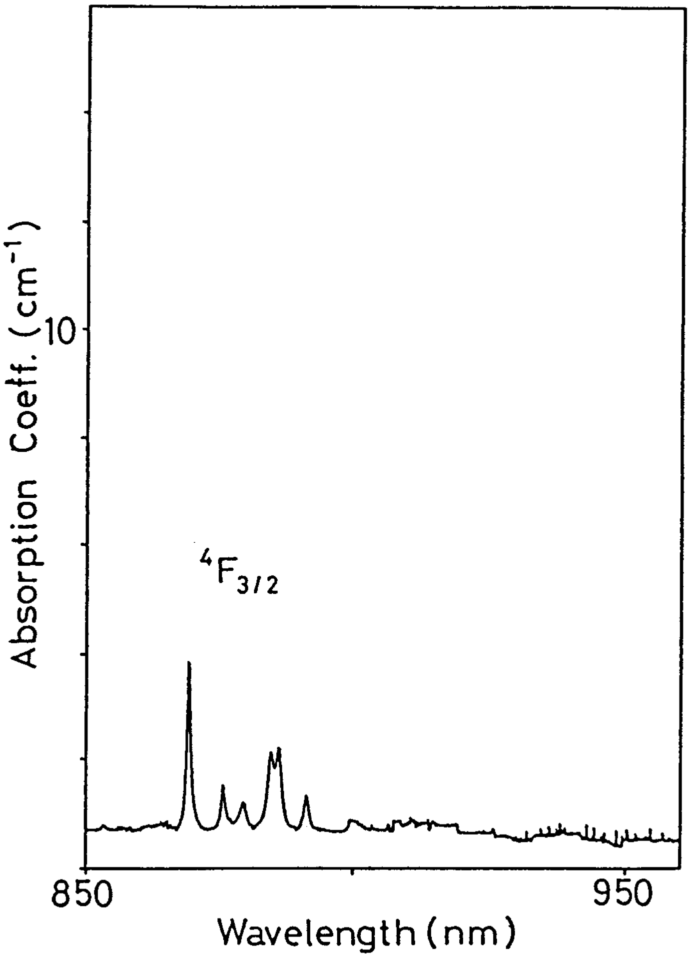

Fig. 10. Absorption spectrum of no. 8 single crystal Nd:YAG between 850 and 960 nm. Multiplet denotes the final level from the ground $^4I_{9/2}$ manifold.

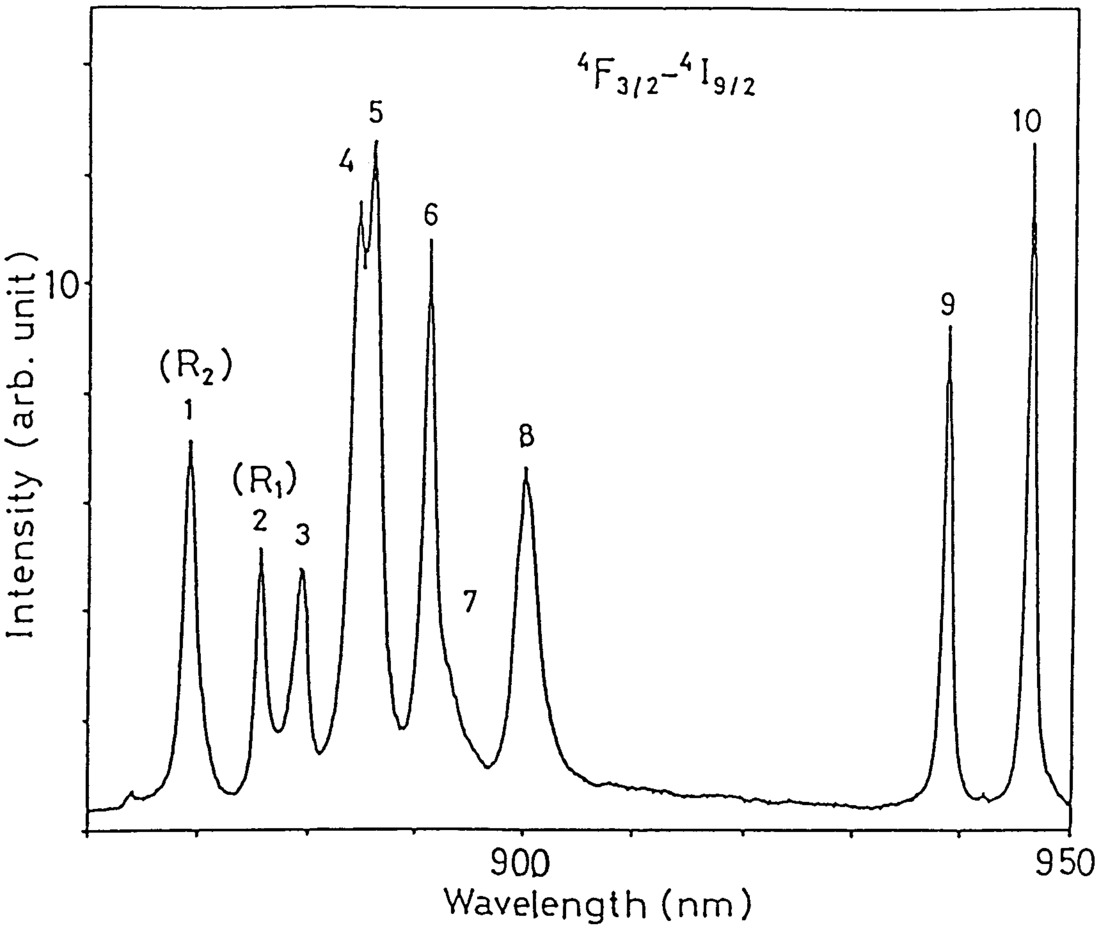

Fig. 11. Emission spectrum of no. 8 single crystal Nd:YAG from $^4F_{3/2}$ to $^4I_{9/2}$ multiplets. The peak numbers correspond to the transition numbers in Fig. 15.

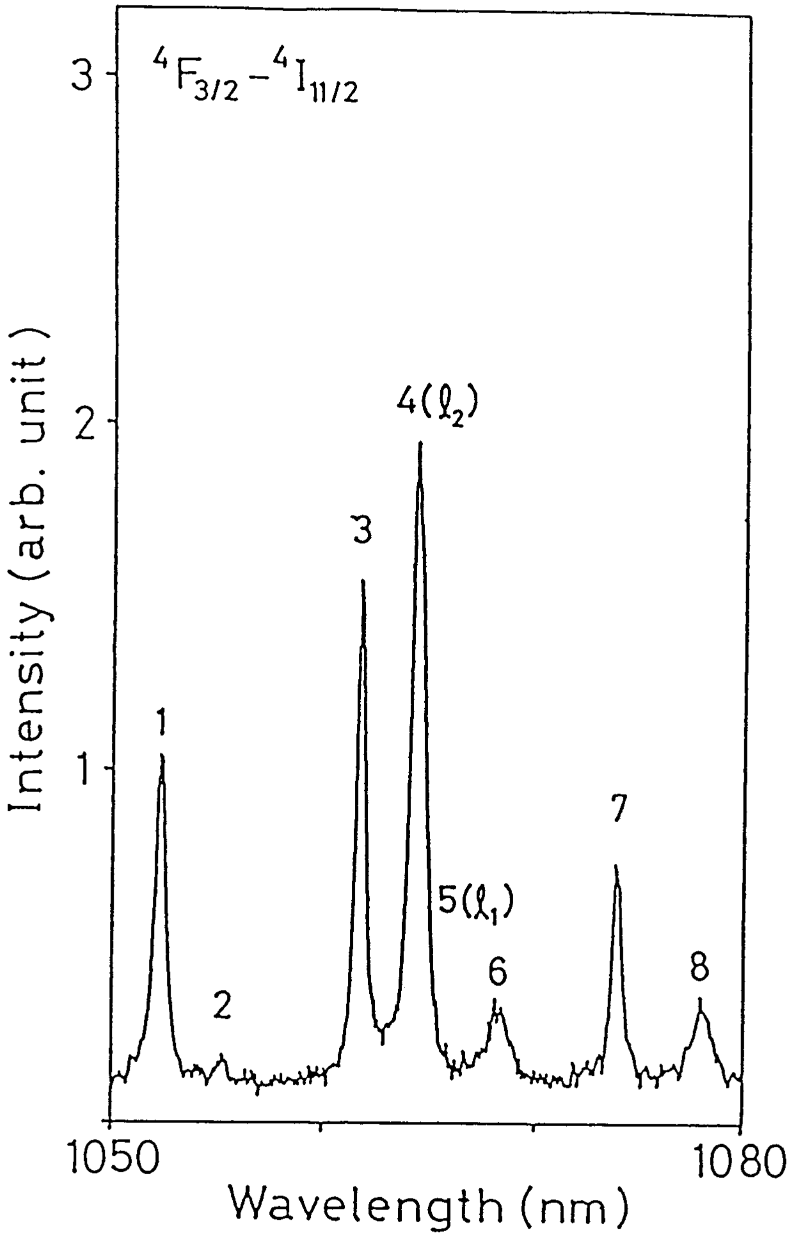

Fig. 12. Emission spectrum of no. 8 single crystal Nd:YAG from $^4F_{3/2}$ to $^4I_{11/2}$ multiplets. The peak numbers correspond to the transition numbers in Fig. 15.

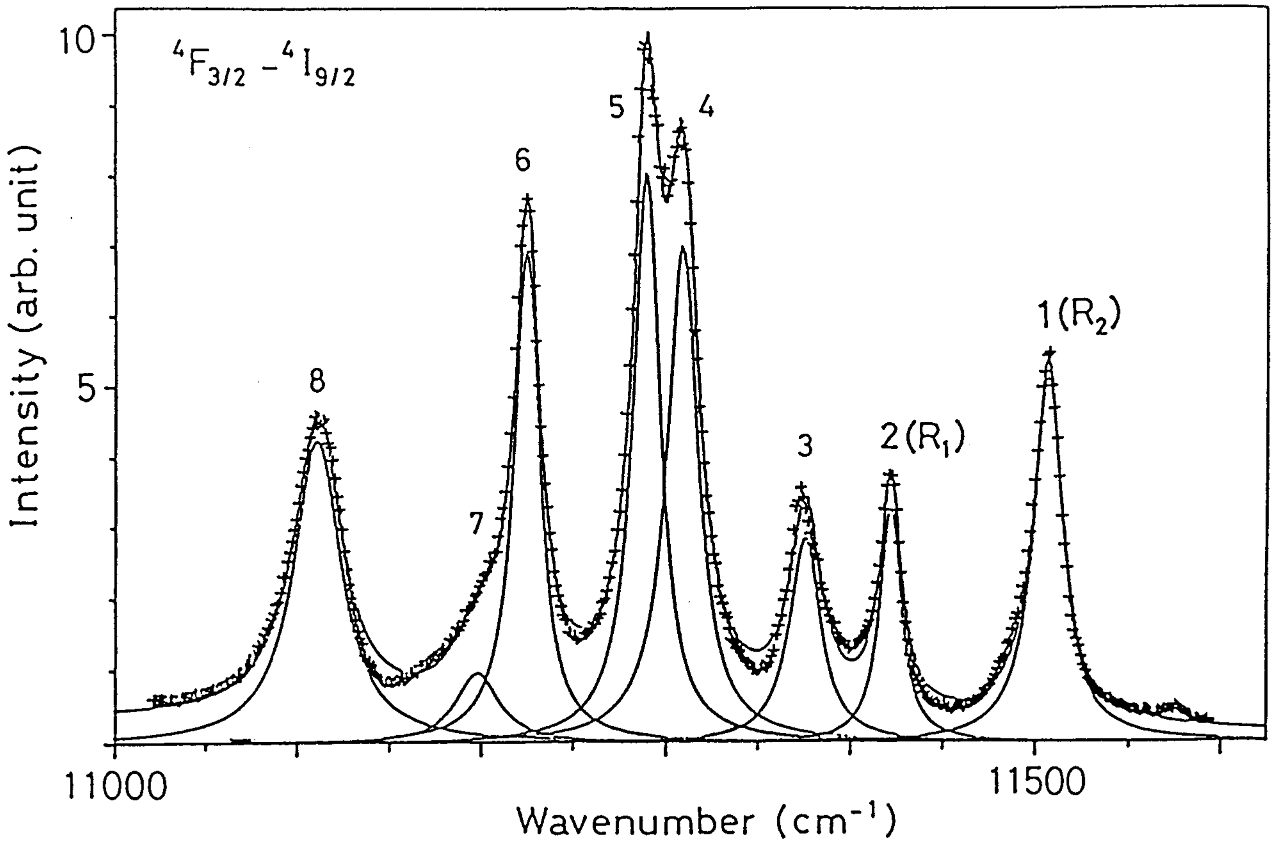

Fig. 13. Decomposition of the $^4F_{3/2}$ to $^4I_{9/2}$ transitions. The + marks denote the experimental data and the solid lines are the component Lorentzian line shape spectra and the composite spectrum. Peak numbers correspond to those in Fig. 11.

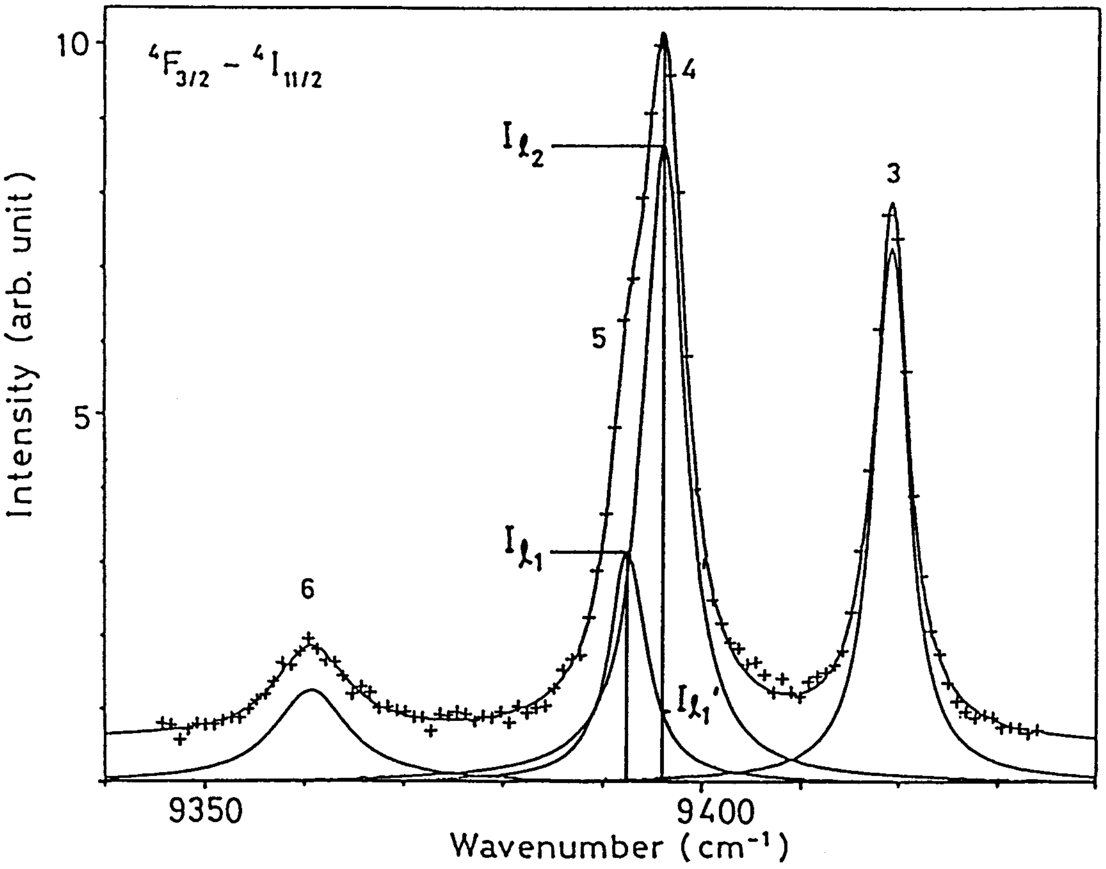

Fig. 14. Decomposition of the $^4F_{3/2}$ to $^4I_{11/2}$ transitions. The + marks denote the experimental data and the solid lines are the component Lorentzian line shape spectra and the composite spectrum. The peak numbers correspond to those in Fig. 12.

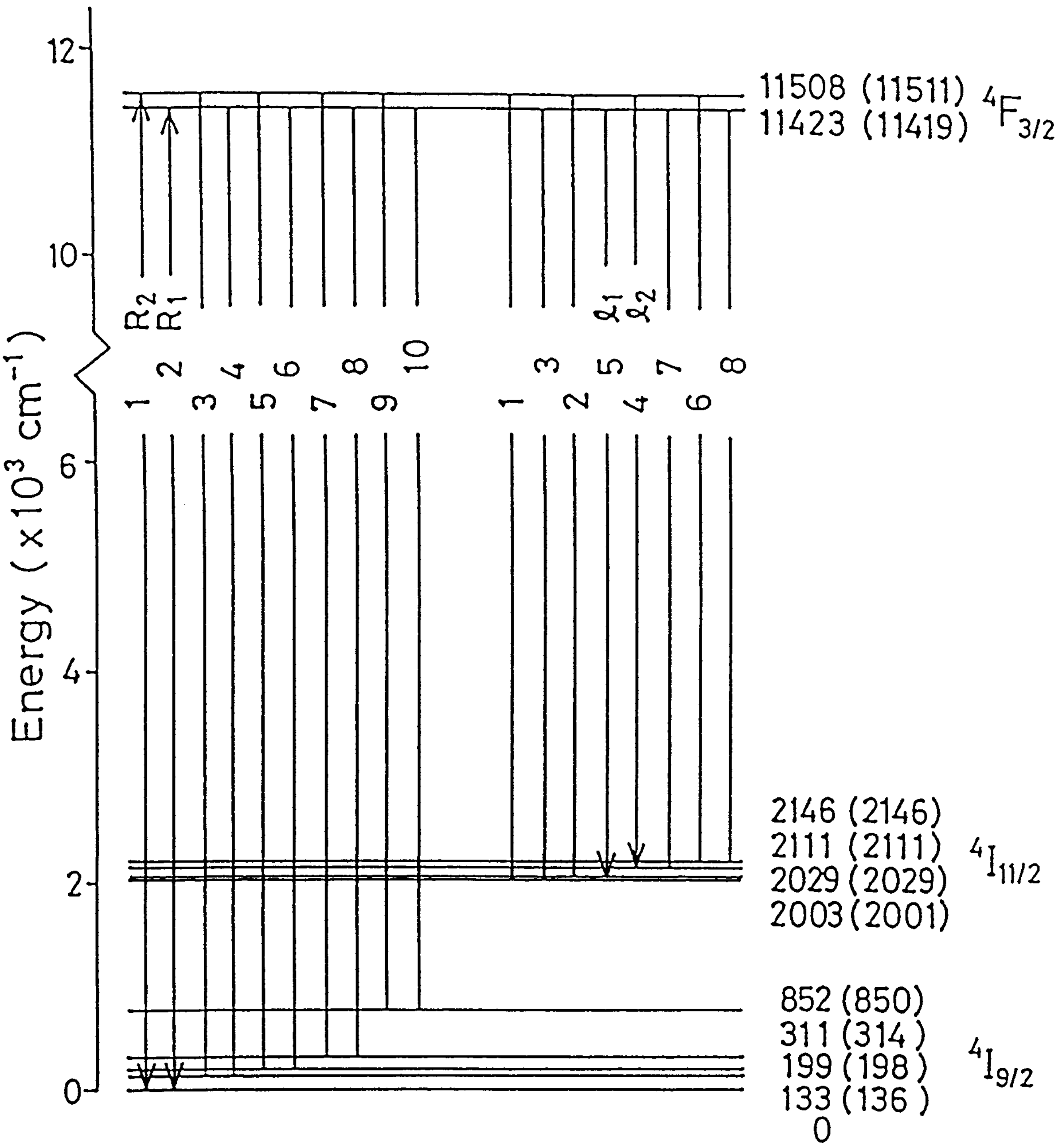

Fig. 15. Energy level structure of the $^4F_{3/2}$, $^4I_{11/2}$ and $^4I_{9/2}$ multiplets of Nd(1%):YAG single crystal. The energy values in parentheses are those reported by Koningstein and Geusic (Reference 28). The ℓ_1 and ℓ_2 are the transitions related to the laser transition.

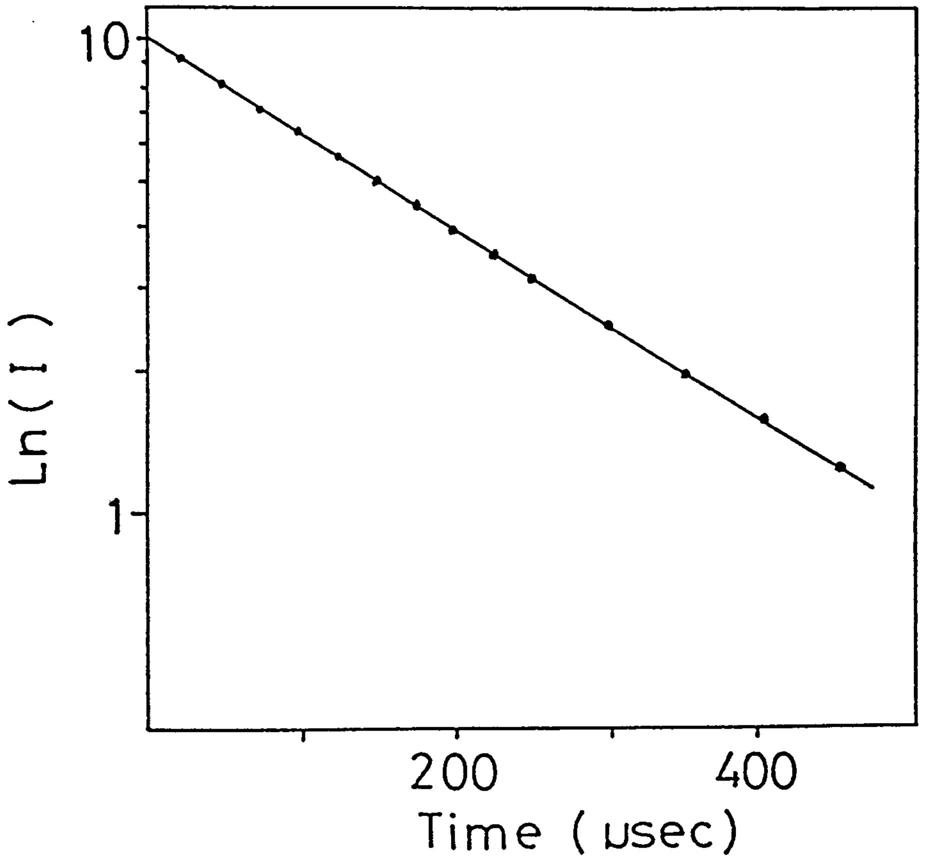

Fig. 16. Transient emission intensity of the $^4F_{3/2}$ to $^4I_{11/2}$ transition at 1064 nm. The emission decay is well expressed in single exponential function.

4.2 Optical spectra of transparent Nd:$Y_3Al_5O_{12}$ ceramics

Nd-doped $Y_3Al_5O_{12}$ (Nd:YAG) ceramics were prepared in two series of synthetic conditions. As described in section 3.1, the principal difference is the calcined conditions of 5 h at 1000 °C and 3 h at 1330 °C and the final sintering time of 3 h and 5 h at 1700 °C for the former and the latter syntheses, respectively. Although background absorption (absorption at non-absorbing wavelengths by Nd^{3+} ion) of the samples was considerably improved from the former synthetic conditions (3.5-4 cm^{-1}) to the latter ones (1.2 cm^{-1}), the optical properties such as line energies, linewidths, relative intensities, etc. in the absorption and emission spectra of the samples are exactly the same for both series of syntheses. Therefore, we will report and discuss the optical properties of Nd:YAG ceramics by the former synthetic conditions in this section. The investigation of further reduction of the background absorption is still in progressing stage, however, the optical properties are proved to be not affected by the reduction of the background absorption.

The urea precipitation method[13,14] provides almost transparent Nd:YAG ceramic disks with more than 99.99% relative density to a single-crystal Nd:YAG, with less than 100 ppm porosity, and with 10-μm grain size. This value of the grain size is about 1 order of magnitude larger than the transparent or translucent ceramics reported so far.[5,7-9,89,97] The background absorption coefficients of the disks were 3.5-4 cm^{-1}, which are far better than the values of 16 and 7 cm^{-1} reported by de With and van Dijk.[9] (The term of "absorption" coefficient used here will be discussed later.) However, Greskovich and Woods reported the absorption coefficient of about 1 cm^{-1} for the Nd-doped Y_2O_3-ThO_2 ceramics.[93] This value may be nearly the smallest limit of absorption coefficient in usual transmission measurements, which is mainly due to the Fresnel surface loss. In our measuring system, the background absorption coefficients are also about 1 cm^{-1} for the FZ single-crystal Nd:YAGs[88] and the other transparent single crystals. The difference between the background absorption coefficients of Nd:Y_2O_3-ThO_2 ceramics and our Nd:YAG ceramics may be mainly due to the difference in porosity.

Although the porosity of our Nd:YAG ceramics is as small as 100 ppm, that of Nd:Y_2O_3-ThO_2 ceramics is only a few ppm or less.[93]

The "absorption" coefficient α used so far is defined as follows:

$$\alpha = - L^{-1} \ln (I / I_0), \qquad (3)$$

where I denotes the transmitted light intensity through samples, I_0 is that of without samples, and L means the sample thickness. The "absorption" coefficient defined as above includes not only the Fresnel surface loss but also scattering at grain boundary, absorption by the other impurities, etc. in the ceramics for the transmission experiments. In this regard, a proper term for the definition of eq. (3) may be an "*attenuation*" coefficient. However, we will use the term "absorption" coefficient even for the spectra of the ceramics measured by the transmission experiments whose reference is the light source spectrum, because of difficulty for subtracting the above-mentioned effects from the measured spectra to obtain a net "absorption" coefficient. This will be discussed later in section 4.4.

The absorption spectra of 1-at.%-Nd-doped YAG [hereafter Nd(1%):YAG] ceramic are shown in Figs. 17 and 18 for the 400-850-nm and 850-960-nm wavelength regions, respectively. The absorption peaks were assigned to the multiplets of Nd^{3+} ion similar to the case of FZ single-crystal in Figs. 8 and 9 in section 4.1. Figure 19 shows the absorption spectra of the ceramic and FZ single-crystal Nd(1%):YAGs simultaneously. In the figure, "cer." denotes the spectrum of the ceramic Nd:YAG and "s.c." is that of FZ single-crystal. The principal features of the spectrum of the ceramic Nd:YAG such as fine structures, relative intensities, line sharpness, etc. are almost the same as those of the single-crystal except larger background absorption of the ceramic. This fact suggests that the optical properties at around Nd^{3+} ion in each grain of the ceramic is the same as those of FZ single-crystal Nd:YAG.

The emission spectra of Nd(1%):YAG ceramic for the 860-950-nm and 1050-1080-nm wavelength regions are shown in Figs. 20 and 21, respectively. The degeneracy is fully removed and all multiplets split into maximum J+1/2 Stark levels except the Kramers degeneracy due to the lower D_2 point symmetry as in the case of FZ single crystals. From these figures, one can also see that principal features are almost the same as those of the single crystal shown in Figs. 11 and 12. The peak numbers in the Figs. 20 and 21 correspond to the transition numbers in the energy-level structure for Nd^{3+} ion in the Nd:YAG ceramic as will be given in Fig. 24. In Figs. 22 and 23, the results of the computer analyses are shown for the decomposition of the emission from $^4F_{3/2}$ to $^4I_{9/2}$ and $^4I_{11/2}$ multiplets. In the figures, the + marks denote the experimental data, and the solid lines are the component and composite spectra. The agreement between experiment and calculation is good, and the spectra can be well decomposed by the Lorentzian line shape. As described in the preceding section, this fact suggests that the Nd^{3+} ions are also incorporated into a single site in each grain of Nd:YAG ceramics and the spectral linewidths are due to the homogeneous broadening mechanism. The meanings of the emission peaks denoted by ℓ_1, ℓ_2, R_1, and R_2 in the figures are the same as those of the FZ single-crystal in Figs. 13 and 14. The results of the decomposition for the Nd(1%):YAG ceramic are given in Table 2 together with the values obtained for the no. 8 sample of FZ single-crystal Nd(1%):YAG given in Table 1. The asymmetry of the number 8 peak is also observed in the ceramic Nd:YAG in Fig. 22 as discussed on the FZ single-crystal in the preceding section.

From the detailed absorption measurements at around 870 nm and the decomposition of the spectra, the transition energies from the ground level of $^4I_{9/2}$ to the two levels of $^4F_{3/2}$ multiplet were determined as 11432 and 11518 cm^{-1} (R_1 and R_2 transitions). These values equal to those from the decomposition of the emission spectra. The line positions given in Table 2 and the peak energies in the absorption spectra are in good agreement with the reported values for the CZ single-crystal[28] within about 10 cm^{-1}. The absorption coefficients α_1 and α_2 for the R_1 and R_2 transitions were simultaneously obtained from the decomposition of the absorption spectra. The values of the absorption coefficient and the emission intensity do not include the background absorption and emission in the table. The values of the absorption coefficient are about 20 % larger than those of FZ single-crystal as can be seen from the table. In the table, the spectral linewidths ($\Delta\nu$) for the R_1, R_2 (no. 2 and no. 1 peaks in Fig. 20), ℓ_1, and ℓ_2 (no. 15 and no. 14 in Fig. 21) transitions are determined to be 12.96, 17.57, 5.27, and 5.02 cm^{-1}, respectively. As for the FZ single-crystal, the corresponding linewidths are 14.00, 18.90, 4.53, and 4.95 cm^{-1}. Those for the ℓ_1 and ℓ_2 transitions of CZ single-crystal were reported as $\Delta\nu_{\ell_1} = 4.2$ cm^{-1} and $\Delta\nu_{\ell_2} = 5.2$ cm^{-1}, respectively.[15] Considering the uncertainty of the calculations with less than 0.42 cm^{-1}, the linewidths of Nd:YAG ceramic were in good agreement with those of FZ and CZ single crystals. This fact indicates that the grains in the Nd:YAG ceramic are well crystallized and the optical quality is good. For example, the background absorption coefficient is 3.5-4 cm^{-1} which is better than the reported values of 16 cm^{-1} for PLZT,[90] 4.2 cm^{-1} for $MgAl_2O_4$,[91] and 16 and 7 cm^{-1} for YAG[9] without subtracting the Fresnel surface loss. Although the background absorption coefficient of $Nd{:}Y_2O_3\text{-}ThO_2$ ceramic[6] is as small as about 1 cm^{-1}, the linewidths of Nd^{3+} absorption in the ceramic are as large as those of Nd^{3+} ion in glasses, which suggests that the ceramic is poorly formed.

From the results of the decomposition of the spectra, we can also construct the energy-level diagram of Nd^{3+} ion in the YAG ceramic for $^4F_{3/2}$ and lower $^4I_{9/2}$ and $^4I_{11/2}$ multiplets similar to the case of FZ single-crystal Nd:YAG. The result is shown in Fig. 24. The energies of the Stark levels of the multiplet were in good agreement with those of FZ single-crystal given in parentheses in the figure within 10 cm^{-1}. The numbers of transitions in the figure correspond to the peak numbers in Figs. 20-23. As for the energy separation of the two Stark levels of $^4F_{3/2}$ multiplet, the value for the Nd(1%):YAG ceramic is determined as 84 cm^{-1}, which is very close to the value of FZ single-crystal with 85 cm^{-1} and those reported for the CZ single crystals[15,28,42,65,69,105] with 84-86 cm^{-1}. There may be many micro-crystal strains in the grains of the ceramic, however, these facts suggests that the strains also do not affect the spectral properties of Nd^{3+} ion in the ceramic similar to the case of FZ single crystals. These facts indicate that the optical properties at around Nd^{3+} ion in the transparent ceramic YAGs are almost the same as those in the CZ and FZ single crystals.

The decay times were measured for the disks with six different Nd concentrations at laser transition wavelength (1064 nm). The excitation conditions were the same to the case of FZ single crystals. The decay curves fit well to a single exponential function as in the case of FZ single-crystal Nd:YAG shown in Fig. 16. This fact suggests that no energy migration also occurs among Nd^{3+} ions in the ceramics similar to the case of FZ single-crystal as discussed in the preceding section. The Nd concentration dependence of the lifetimes is shown in Fig. 25. The overall characteristic (i. e., the concentration quenching in lifetimes) is almost the same as that reported for the CZ single-crystal[105] as shown in broken line in the figure except that the lifetime with 270 ± 5 μs at the non-quenching concentrations of our Nd:YAG ceramics is slightly smaller than that with 280 μs for the CZ single-crystal Nd:YAG.[105] The decay time of Nd(1%):YAG ceramic at 1064-nm wavelength was 219 μs, which is also slightly smaller than the reported values[15,67-69,71,72] of 226-257 μs for the CZ single crystals and 226, 244, and 253 μs for the FZ single crystals by this study.

Table 2. Spectral parameters of transitions between $^4I_{9/2,11/2}$ and $^4F_{3/2}$ manifolds. These values are obtained from the decomposition of the absorption and emission spectra as shown in Fig. 22 and 23. N_0 denotes the Nd concentration, α the absorption and emission coefficients, L the sample thickness, I the peak intensities, ν the central energy of the Lorentzian line shape function and $\Delta\nu$ the full width at half maximum of the peak intensity.

	ceramic	single crystal	unit
N_0	1.4×10^{20}	1.4×10^{20}	cm^{-3}
α_{R_1}	0.952	0.74	cm^{-1}
α_{R_2}	3.76	2.98	cm^{-1}
L	0.1556	0.3114	cm
I_{R_1}	5.76	4.29	
ν_{R_1}	11432.24	11423	cm^{-1}
$\Delta\nu_{R_1}$	12.96	14.00	cm^{-1}
I_{R_2}	9.56	6.71	
ν_{R_2}	11518.36	11508	cm^{-1}
$\Delta\nu_{R_2}$	17.57	18.90	cm^{-1}
I_{ℓ_1}	0.886	0.583	
ν_{ℓ_1}	9400.1	9394	cm^{-1}
$\Delta\nu_{\ell_1}$	5.27	4.53	cm^{-1}
I_{ℓ_2}	2.05	1.61	
ν_{ℓ_2}	9403.6	9397	cm^{-1}
$\Delta\nu_{\ell_2}$	5.02	4.95	cm^{-1}

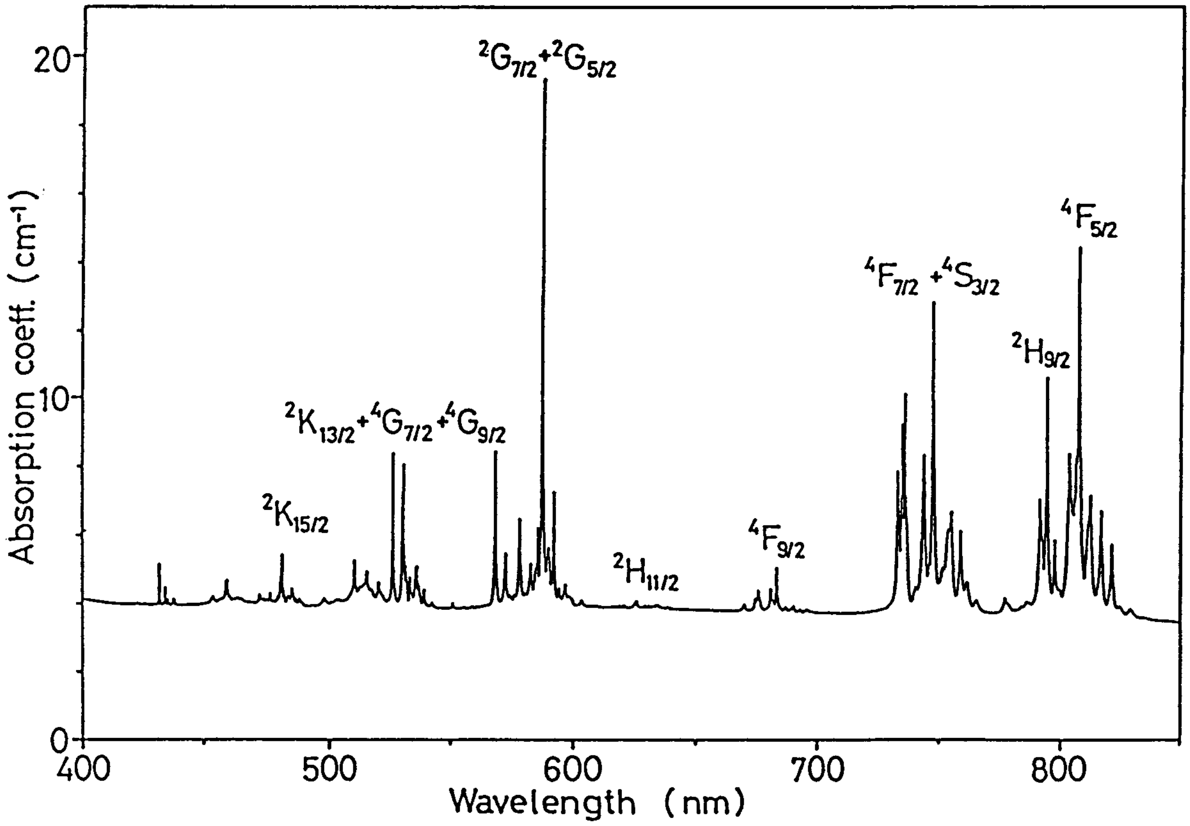

Fig. 17. Absorption spectrum of Nd(1%):YAG ceramic between 400 and 850 nm. Multiplets denote the final levels from the ground $^{4}I_{9/2}$ manifold.

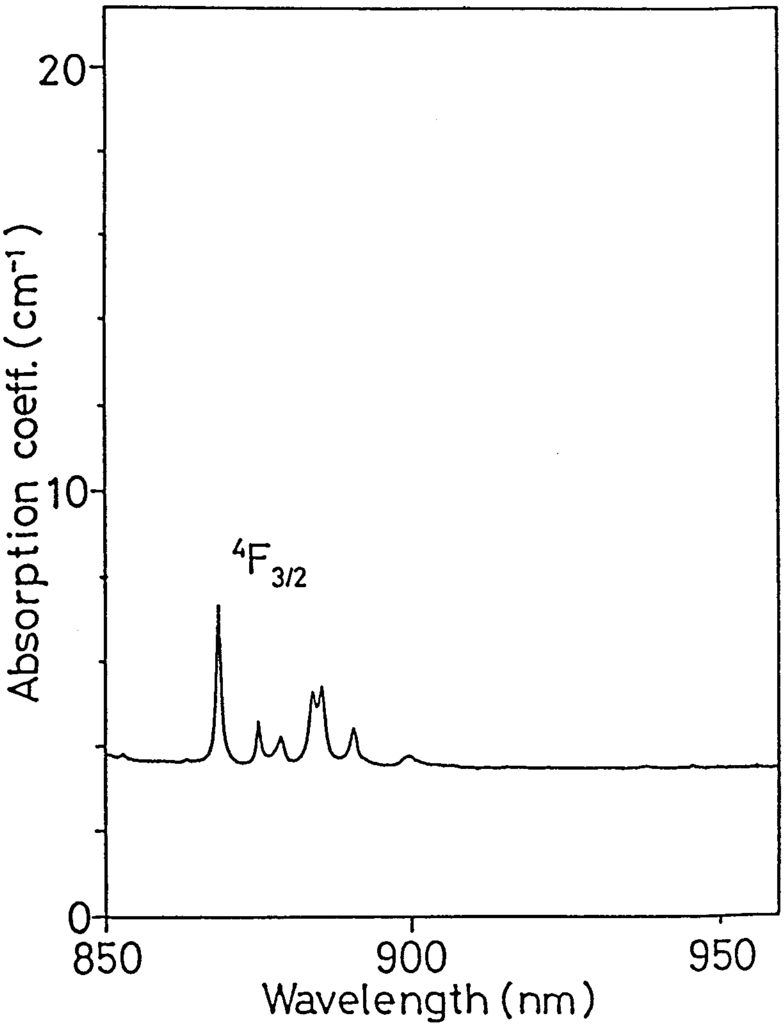

Fig. 18. Absorption spectrum Nd(1%):YAG ceramic between 850 and 960 nm. Multiplet denotes the final level from the ground $^4I_{9/2}$ manifold.

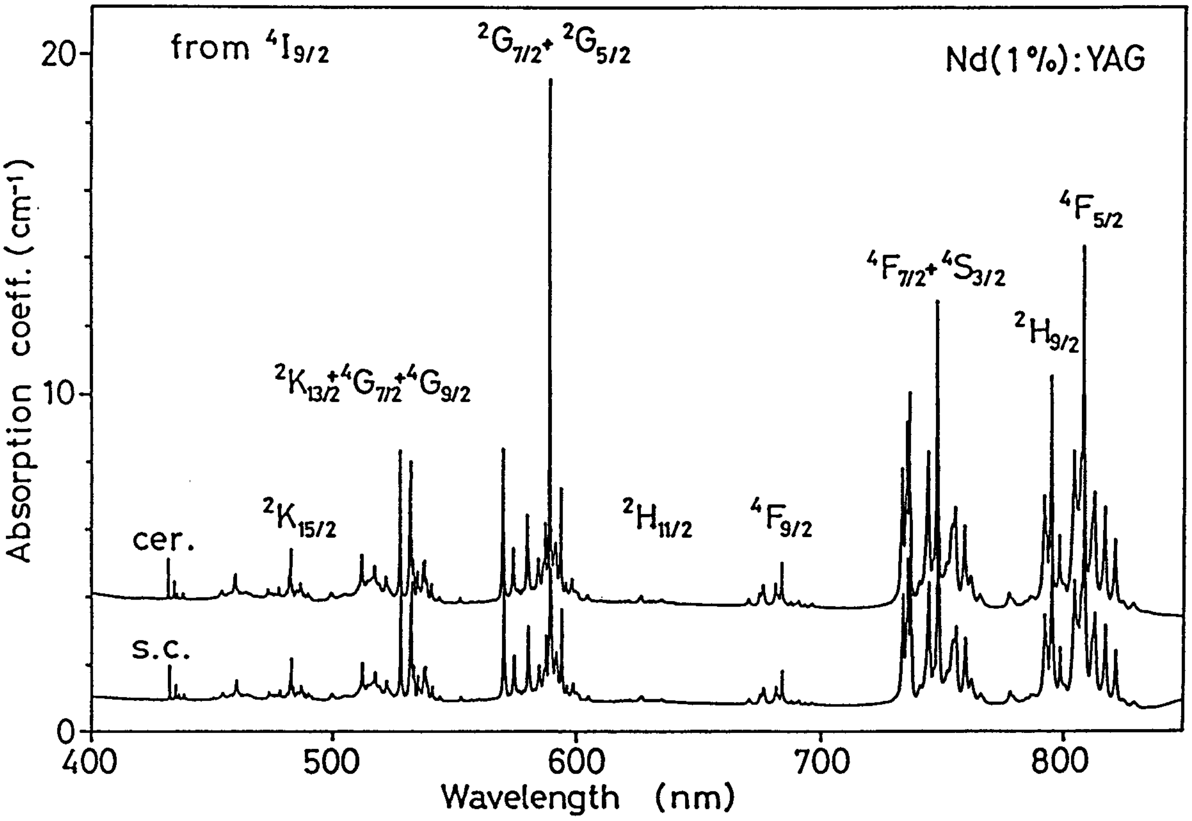

Fig. 19. The absorption spectra of ceramic Nd(1%):YAG and single crystal Nd(1%):YAG grown by floating zone method. The "cer." denotes the ceramic Nd:YAG spectrum and the "s.c." shows the single crystal spectrum.

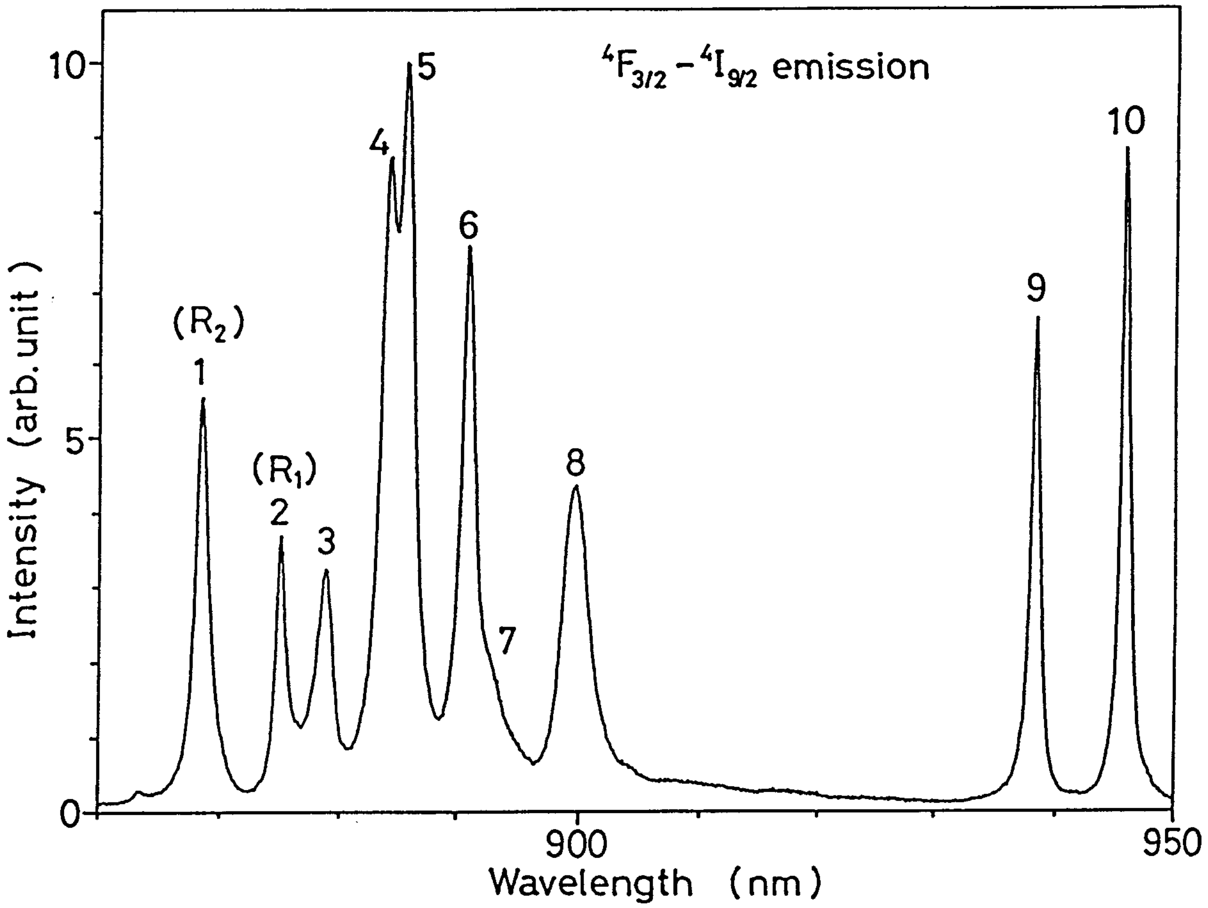

Fig. 20. Emission spectrum Nd(1%):YAG between 860 and 950 nm. These are transitions from $^4F_{3/2}$ to $^4I_{9/2}$ multiplets. The peak numbers correspond to the transition numbers in Fig. 24.

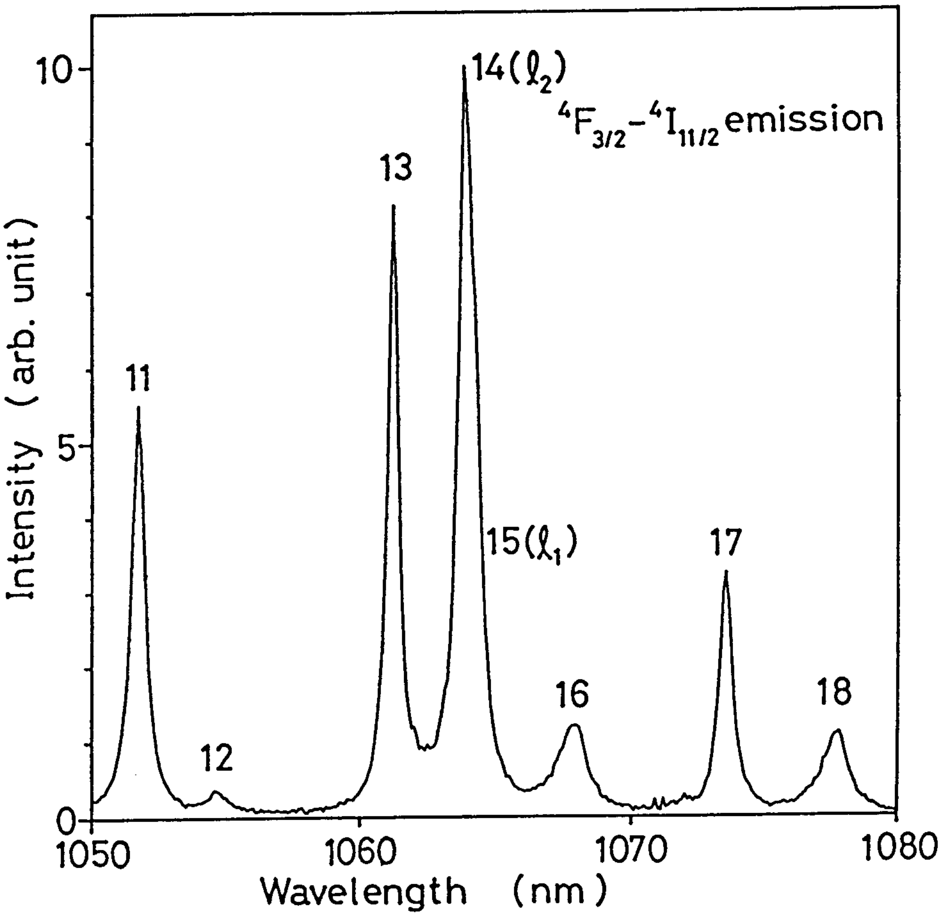

Fig. 21. Emission spectrum of Nd(1%):YAG between 1050 and 1080 nm. These are transitions from $^4F_{3/2}$ to $^4I_{11/2}$ multiplets. The peak numbers correspond to the transition numbers in Fig. 24.

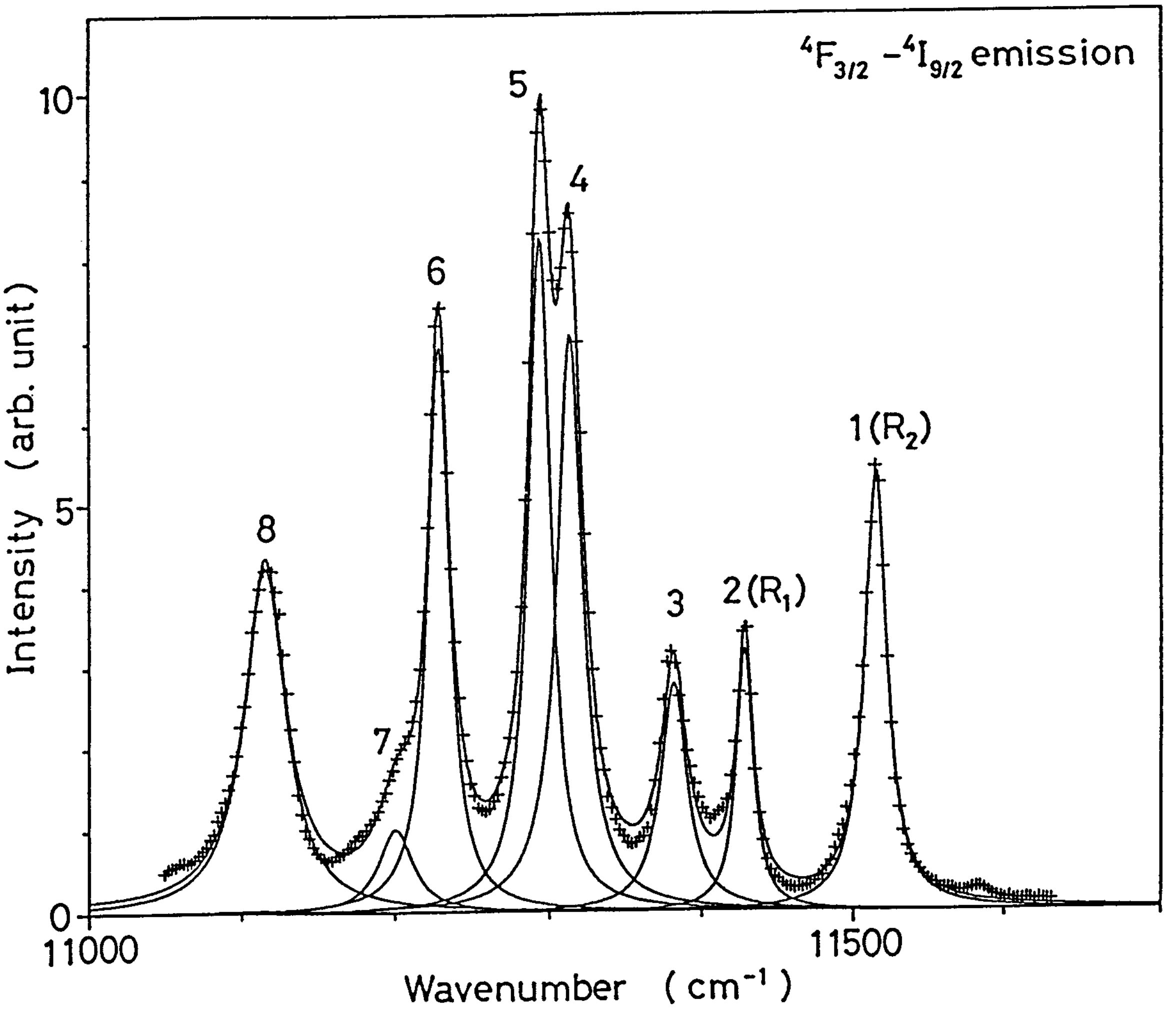

Fig. 22. Decomposition of the $^4F_{3/2}$ to $^4I_{9/2}$ transitions. The + marks denote the experimental data and the solid lines are the component Lorentzian line shape spectra and the composite spectrum. The peak numbers correspond to those in Fig. 20.

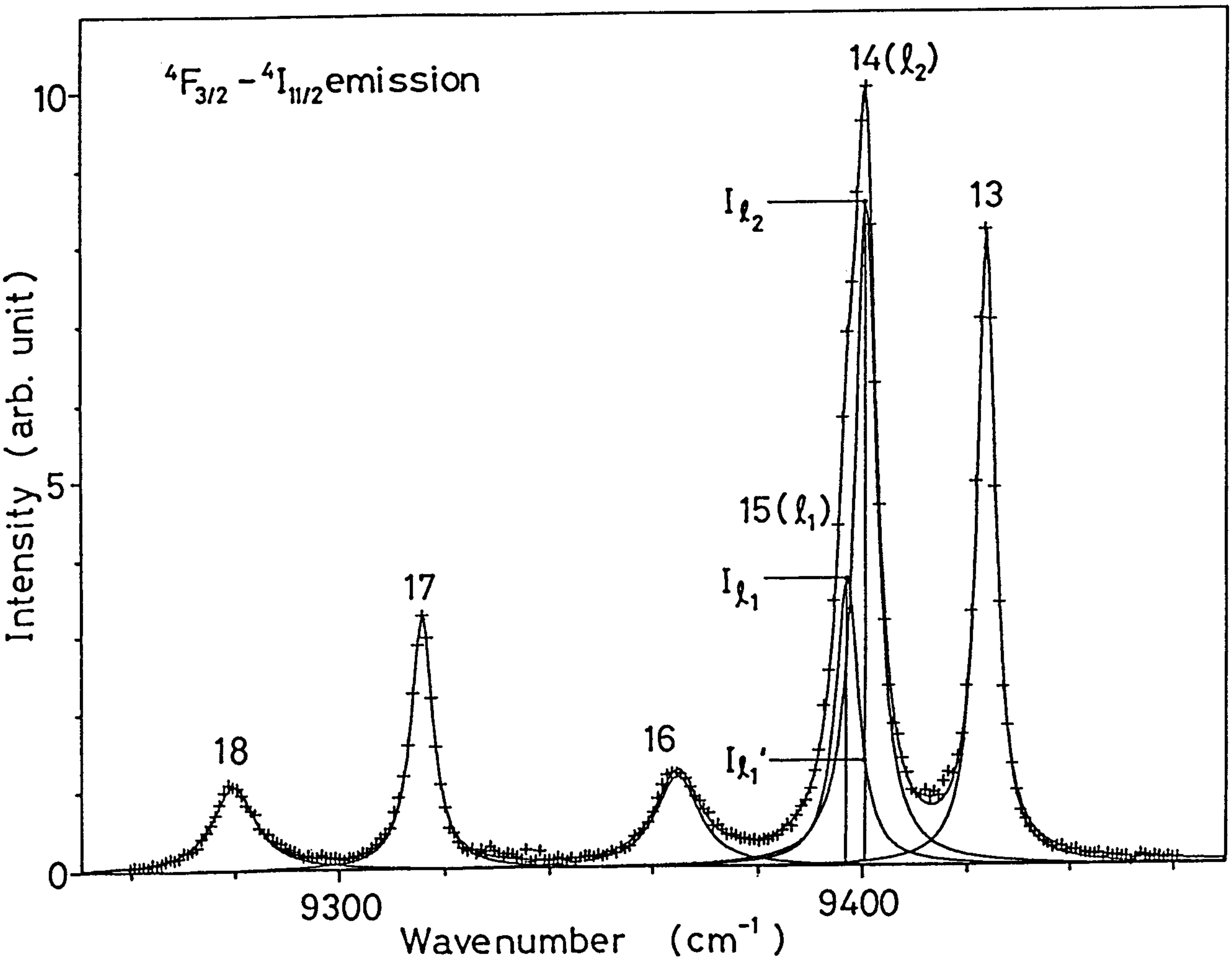

Fig. 23. Decomposition of the $^4F_{3/2}$ to $^4I_{11/2}$ transitions. The + marks denote the experimental data and the solid lines are the component Lorentzian line shape spectra and the composite spectrum. The peak numbers correspond to those in Fig. 21.

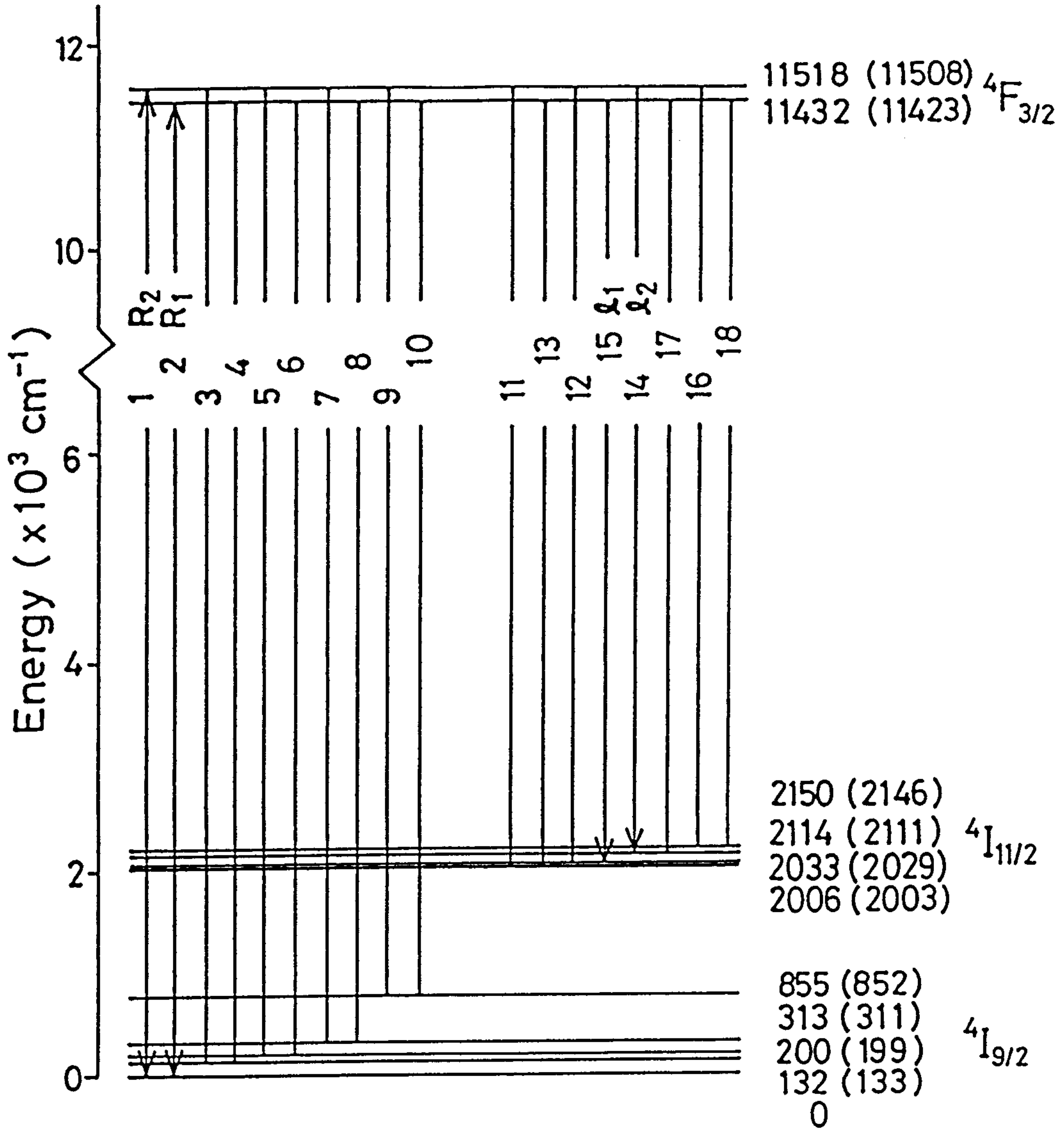

Fig. 24. Energy level structure of the $^4F_{3/2}$, $^4I_{11/2}$ and $^4I_{9/2}$ multiplets of Nd(1%):YAG ceramic. The energy values in parentheses are those of the single crystal grown by the floating zone method. The ℓ_1 and ℓ_2 are the transitions related to the laser transition.

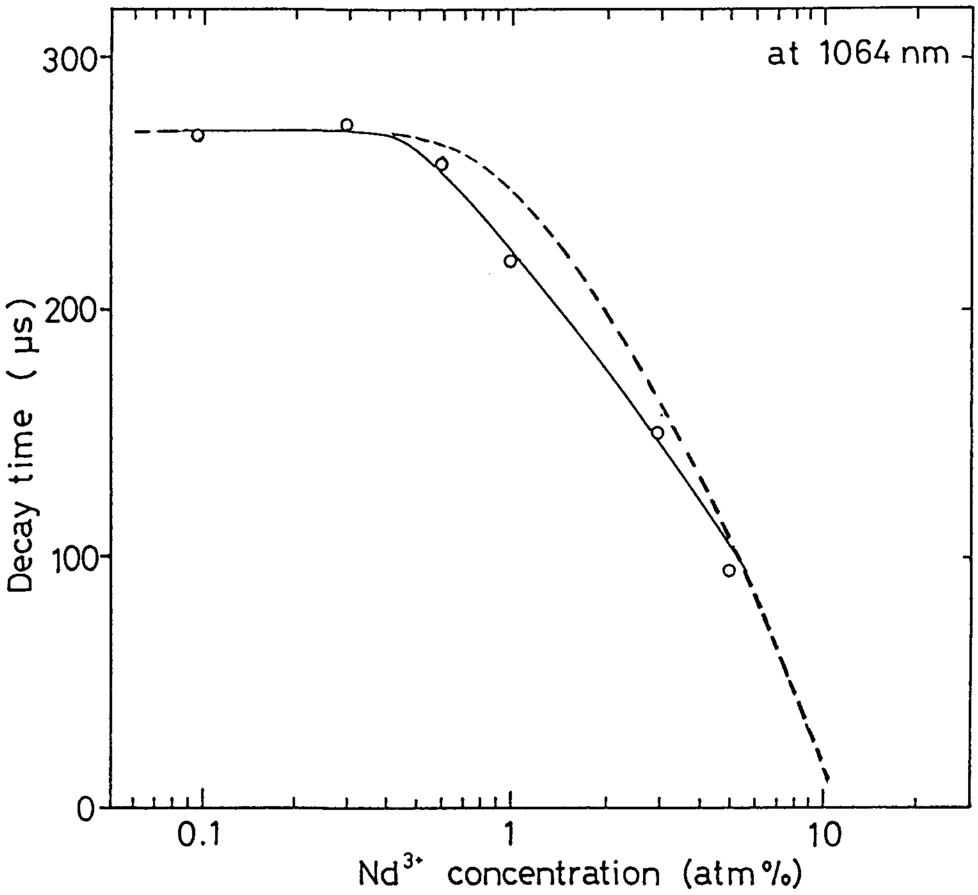

Fig. 25. Concentration dependence of the decay times at 1064 nm. Typical concentration quenching can be observed. The broken line is that of the single crystal Nd:YAG reported by Singh et al. (Reference 105).

4.3 Evaluation of induced emission cross sections

An induced emission cross section σ_ℓ^{in} is proportional to the gain of the laser media and is accordingly an important parameter to evaluate the materials as laser media. The quantitative evaluation of the σ_ℓ^{in} of Nd:YAG was first reported by Neeland and Evtuhov.[68] Since then extensive studies were made by various investigators[15,67-72] as reviewed in chapter 2. Today, there are three acceptable methods to evaluate σ_ℓ^{in}. First, based upon the spectroscopic measurements, σ_ℓ^{in} is evaluated by the intensity ratio of the laser transition to that of some reference line which can be observed in terms of both absorption and emission.[15,68,69] The second method stands on the basis of observation of the branching ratios and lifetime.[15,68,69] In the third method, the absorption from the final level of laser transition ($^4I_{11/2}$) to initial $^4F_{3/2}$ levels is directly observed.[110,111]

As for the second method, although the branching ratios of $^4I_{9/2}$ and $^4I_{11/2}$ final levels can be relatively accurately obtained, those of $^4I_{13/2}$ and $^4I_{15/2}$ final levels are difficult to obtain accurately since these transitions are in the medium infrared (IR) wavelength region where sensitive detectors are hardly available. As for the third method, it was tried first on a Nd-doped borate glass at 546 °K,[110] however, the result may be not so accurate since the population of $^4I_{11/2}$ multiplet, which resides by about 2000 cm^{-1} above the ground $^4I_{9/2}$ multiplet, by the Boltzmann distribution is still very small even at the higher temperature. The method was also applied to compounds such as $LiNdP_4O_{12}$ (Ref. 111) which contains the Nd^{3+} ion as a stoichiometric agent. In the case of Nd:YAG, it is not possible to evaluate σ_ℓ^{in} by this method, since it contains usually only 0.5-1.0 at.% Nd concentration, and the population of $^4I_{11/2}$ multiplet is only 7×10^{-5} times as small as that of the ground level at room temperature. This is way too small to yield the result of acceptable accuracy. In the first method, on the other hand, the spectra can be measured accurately and relatively easy. Therefore, we evaluate σ_ℓ^{in} for our crystals and ceramic Nd:YAGs by this method.

According to Kushida, Marcos, and Geusic,[15] the intensity ratio of a certain reference line (R_1 and R_2 in Figs. 15 and 24 for the FZ single-crystal and the transparent ceramic, respectively) to the laser transition (ℓ transition) for simple three-level system shown in Fig. 26 is given by

$$I_R / I_\ell = (n_R / n_\ell)^2 (\nu_R / \nu_\ell)^3 \sigma_R / \sigma_\ell, \qquad (4)$$

where I denotes intensity, n refractive index, ν the line energy in cm^{-1}, and σ the cross section. As for the refractive indices, the ratio is omitted in the original equation of eq. (2) by Kushida, Marcos, and Geusic[15] as reviewed in chapter 2. The values of the refractive indices from 400 nm to 1200 nm reported by Bond[112] were interpolated to the values at R_2 and ℓ_2 wavelengths by a seventh-order polynomial in wavelength, and we obtain 1.005 for the ratio $(n_R / n_\ell)^2$ in eq. (4). As shown in Fig. 26, the cross section (σ) consists of the induced emission cross section (σ_ℓ^{in}) and a spontaneous cross section (σ_ℓ^{sp}) terms. From the definition of the cross sections,[48] the induced emission cross section σ_ℓ^{in} is exactly the same as the absorption cross section σ_R^{abs}. The cross section for the R transition can be calculated from the absorption coefficient and concentration as $\sigma_R^{abs} = \alpha_R / N_0$, where N_0 denotes the Nd concentration.

To apply the relationship of eq. (4) to our FZ single-crystal and ceramic Nd(1%):YAGs, two phenomena must be taken into consideration. The first is reabsorption of R emission of which terminal level is the ground $^4I_{9/2}$ level. The reabsorption may occur by another Nd^{3+} ion in the ground state. Assuming that the Nd^{3+} ions are uniformly excited along the normal to the surface of sample (I_0), the following relation holds between the fraction of observed intensity (dI^{obs}) and the fraction of thickness (dx) at x from surface as $dI^{obs} = I_0 \{\exp(-\alpha x) - \exp[-\alpha(x + dx)]\}$. The correction of the reabsorption is expressed for a small absorption coefficient and sample thickness as

$$I_R = I_R^{obs} / (1 - \alpha_R \cdot L/2), \qquad (5)$$

where α_R denotes the absorption coefficient at the R line, and L is the sample thickness. Secondly, although the laser transition mainly occurs through the ℓ_2 transition in Figs. 14 and 23, the component of the ℓ_1 emission at ℓ_2 wavelength (denoted by I_{ℓ_1}' in Figs. 14 and 23) also contributes to the laser transition. Therefore, a correction has to be also made on this extra contribution. If the induced emission cross section of the ℓ_1 emission at the ℓ_2 wavelength is denoted by $\sigma_{\ell_1}{}^{in}(\ell_2)$, then $\sigma_{\ell_1}{}^{in}(\ell_2) = \sigma_{\ell_1}{}^{in} \times 0.312$, which can be calculated at the ℓ_2 wavelength from the Lorentzian line shape function with the peak intensity of the ℓ_1 transition. Using the population fraction of the R_1 level in thermal equilibrium denoted by a (=0.660 at 300 °K from the energy difference between two Stark levels of $^4F_{3/2}$ multiplet for Boltzmann distribution), we obtain the total induced emission cross section $\sigma_\ell{}^{in}$ in the form[15]

$$\sigma_\ell{}^{in} = \sigma_{\ell_1}{}^{in}(\ell_2)/a + \sigma_{\ell_2}{}^{in}. \qquad (6)$$

When applying these equations to the FZ single crystals and the ceramic Nd:YAGs, the multiplication factor of 58.7 as mentioned in section 3.2 must be taken into consideration of the spectral response of the measuring system for the emission intensity I given in Tables 1 and 2.

By making use of the results of the decomposition given in Table 1, the results of the calculations of the induced emission cross section for the FZ single crystals are given in Table 3 as 7.4×10^{-19}, 5.3×10^{-19}, and 7.0×10^{-19} cm^2 for the no. 0, no. 8, and no. 38 crystals, respectively. The ratios of eq. (4) are 20.7, 15.5, and 20.4 for the no. 0, no. 8, and no. 38 crystals, respectively. These values are in good agreement with the ratio of 21 ± 2 reported by Kushida, Marcos, and Geusic.[15] The values of the induced emission cross section reported so far are given in Table 4 together with lifetimes of CZ single-crystal Nd:YAGs[15,67-69,71,72] and related crystals.[113,114] The values given in the first three lines of Table 3 were obtained by assuming that the quantum efficiency of the R levels equals to unity.[75] As for the quantum efficiency, the values from 0.4 to about unity have been reported so far through direct and indirect measurements,[69,72,75,116-120] however, we decided that the value of unity reported by Kushida and Geusic[75] is the most reliable one as mentioned in section 2.1 and is used for the above calculations.

On the transparent Nd:YAG ceramic, we can obtain the induced emission cross section for the ℓ_2 transition as $\sigma_{\ell_2}{}^{in} = 4.42 \times 10^{-19}$ cm^2 from eqs. (4) and (5) by making use of the values of I_R, I_ℓ, ν_R, ν_ℓ, and the calculated value of $\sigma_R^{abs} = 2.69 \text{ X } 10^{-21}$ cm^2 from the results of the decomposition of the absorption spectrum of the ceramic as given in Table 2. We can similarly calculate the induced emission cross section as $\sigma_{\ell_1}^{in} = 1.02 \text{ X } 10^{-19}$ cm^2 from the values for the R_1 and ℓ transitions in Table 2. By making use of the values of $\sigma_{\ell_1}(\ell_2)^{in}$, $\sigma_{\ell_2}^{in}$, and the fraction a , we can finally obtain the total induced emission cross section by substituting these values into eq. (6) as $\sigma_{\ell}^{in} = 4.9 \text{ X } 10^{-19}$ cm^2. This value falls in the range of the reported values[15,67-69,71,72] for the CZ single-crystal Nd:YAGs from $2.7 \text{ X } 10^{-19}$ to $8.8 \text{ X } 10^{-19}$ cm^2 as given in Table 5.

From the results of section 4.1, the optical spectroscopic properties such as relative line intensities, line positions, linewidths, etc., the relevant energy-level, and the decay time constants of Nd^{3+} ion in the FZ single crystals can be concluded to be comparable to those of Nd:YAG single crystals grown by the conventional CZ method. Also the induced emission cross section of FZ single crystals have comparable values to those of CZ single crystals. As described in chapter 1, the FZ method requires relatively inexpensive apparatus and no Ir crucible which is a serious source for the contamination. Further, one of the most important advantages of FZ method is shorter growth time of single crystals than that of the conventional CZ method. From these facts, we can conclude that the FZ method is suitable for determining the optimum concentration of Nd^{3+} ion in not only the YAG single crystal but also the other possible host crystals for the Nd laser in shorter time than the CZ method.

As for the transparent Nd:YAG ceramics, the optical properties as mentioned above in the absorption and emission spectra of the ceramics are almost the same as those of CZ and FZ single crystals as discussed in the preceding section. The energy-level of Nd:YAG ceramics is also almost the same as those of CZ single crystals[15,67-69,71,72] and the FZ single-crystal[88] except the larger background absorption of the ceramics. The value of the induced emission cross section as calculated above for the ceramic is also comparable to the CZ and FZ single crystals, therefore the ceramic has a potential to become laser material. The larger grain size of our Nd:YAG ceramics than that of the other translucent or transparent ceramics may have great advantage of reducing the energy loss of reflection, scattering, etc. at grain boundaries while light amplification. However, the larger background absorption of the ceramics, which may be mainly due to larger porosity compared with the Nd:Y_2O_3-ThO_2 ceramics,[6] will prevent laser oscillation as a loss factor by light scattering at the pores.[48] Although the laser oscillation was observed in the Nd:Y_2O_3-ThO_2 ceramics, the threshold energies of the pulsed laser oscillation for the ceramics were 16, 21, and 30 J,[6] which are about 1 order of magnitude larger than those of CZ single-crystal Nd:YAG with 2.0 and 3.8 J.[1] This may be due to the disordered nature of Nd:Y_2O_3-ThO_2 ceramics, which results in larger absorption and emission linewidths of the ceramics, reducing the induced emission cross section. The degree of crystallization of each grain of our Nd:YAG ceramics is found to be very good and the grain size is larger than that of the Nd:Y_2O_3-ThO_2 ceramics[6] by about 1 order of magnitude for the Nd:YAG ceramics. If the porosity of our Nd:YAG ceramics can be decreased, it may be possible to reduce the threshold energy of a ceramic laser since the pores might be one of the most serious loss factors for laser amplification.[48]

Table 3. Induced emission cross section in the unit of cm^2 of three crystals calculated from the spectral data given in Table 1.

	no. 0	no. 8	no. 38
σ_{ℓ_2}	1.2×10^{-18}	8.8×10^{-19}	1.1×10^{-18}
σ_{ℓ_1}	1.4×10^{-19}	1.1×10^{-19}	1.3×10^{-19}
σ_{ℓ}	1.4×10^{-18}	1.0×10^{-18}	1.3×10^{-18}
calibrated σ_{ℓ}	7.4×10^{-19}	5.3×10^{-19}	7.0×10^{-19}

Table 4 Values of the induced emission cross sections and lifetimes reported so far for the Nd:YAG by CZ method and related single crystals, and those of the Nd:YAG grown by the FZ method calculated in section 4.3.

Crystal	Induced emission cross section ($\times 10^{-19}$ cm^2)	Life time (μs)	Reference
Nd:YAG	2.7	236	68
Nd:YAG	3.5	236	68
Nd:YAG	4.6	230	69
Nd:YAG	5.6	...	71
Nd:YAG	7.6	238-257	72
Nd:YAG	8.8	230	15
Nd:YAG	8.8	240	67
Nd:$YAlO_3$	12	65	113
Nd:$YAlO_3$	47	...	114
Nd:La_2O_2S	21	...	71
Nd:YAG	5.3-7.4	226-253	This section

Table 5. Reported values of the induce emission cross section and the decay times of Nd:YAG single crystals and those of the ceramic Nd:YAG.

	Induced emission cross section ($\times 10^{-19}$ cm^2)	Decay time (μs)	Reference
Crystal	2.7	236	68
Crystal	3.5	236	68
Crystal	4.6	230	69
Crystal	5.3-7.4	226-253	Table 4
Crystal	5.6	...	71
Crystal	7.6	238-257	72
Crystal	8.8	230	15
crystal	8.8	240	67
Ceramic	4.9	219	This section

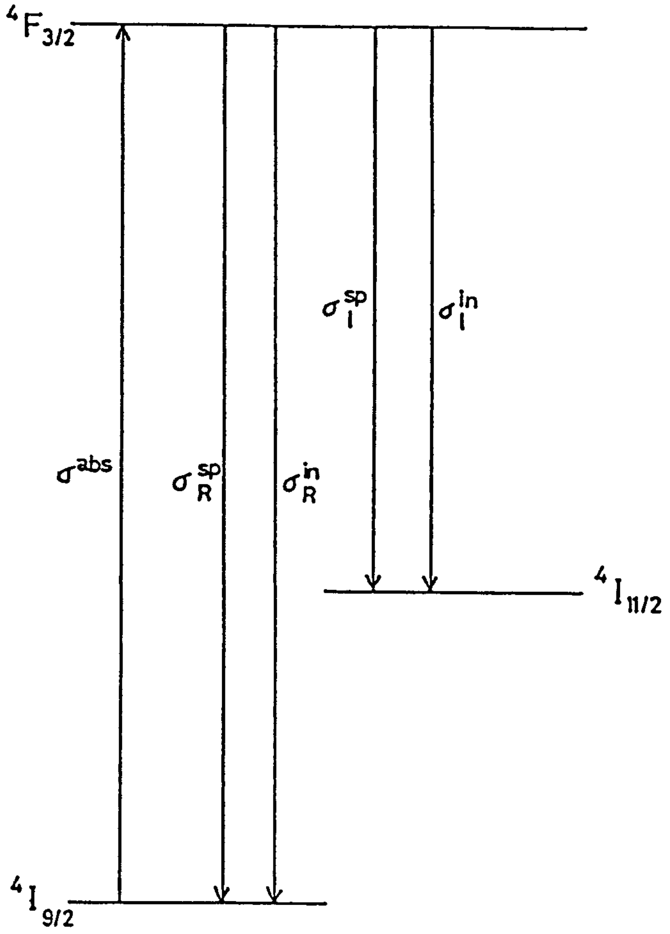

Fig. 26. Simplified level structure to describe the relationship between cross sections (sigma's).

4.4 Optical spectra of undoped and rare-earth-doped transparent $Y_3Al_5O_{12}$ ceramics

There have been almost no optical investigation on optically active ion-doped transparent ceramics so far only except the transmission spectrum of Nd:Y_2O_3-ThO_2 ceramics reported by Greskovich and Chernoch.[6] After the first success in synthesis of the transparent Nd:YAGs with about 4 cm^{-1} background absorption as discussed in the section 4.2 (see, e. g., Fig. 19), Haneda et al.[14] have successfully prepared an undoped, and rare-earth-(RE = Pr, Nd, Er, and Eu) doped $Y_3Al_5O_{12}$ (RE:YAG) ceramics with far smaller background absorption of about 1.2 cm^{-1}, of which value is almost comparable to that of FZ single-crystal. In this section, we will report and discuss the basic spectroscopic properties of the undoped and RE-doped YAG ceramics for the first time.

At first, we describe general characteristics of the undoped and RE:YAG ceramics under the latter synthetic condition as described in section 3.1. Although the Eu-doped ceramic YAG (Eu:YAG) was sintered at a different time under the same conditions, the undoped, Pr-, Nd-, and Er-doped ceramic YAGs were sintered simultaneously. Therefore, the final sintering conditions were strictly the same for latter four samples. The sample color was pale green, pale purple, and pale pink for Pr:YAG, Nd:YAG, and Er:YAG ceramics, respectively. The undoped and Eu:YAG ceramics were almost colorless.

Figure 27 shows a photograph of the transmission electron microscope (TEM) at around the grain boundary of the undoped ceramic YAG. Except a few layers distortion at around grain boundary, one can observe that the grains are uniform and almost no lattice distortion is shown in the photograph. Almost all stronger peaks in the RE:YAG ceramics have Lorentzian line shape and the linewidths are as narrow as those in corresponding RE-doped single-crystal YAGs. Together with the fact that the spectral characteristics of Nd:YAG ceramic are almost the same as those of FZ single-crystal as described in section 4.2, these facts suggest that the grains in the ceramic YAGs are well crystallized and the RE ion site is unique.[121] Absorption and emission spectra for Pr:YAG, Nd:YAG, and Er:YAG ceramics are shown in Figs. 28–30, respectively. To show each spectrum of RE:YAG ceramics clearly, the spectra of Nd:YAG and Er:YAG ceramics are drawn by shifting zero levels for the absorption and emission spectra and multiplying appropriate factors for the emission spectra, as will be stated in the following subsections.

For the absorption spectra of these Pr:YAG, Nd:YAG, and Er:YAG ceramics, the reference spectrum is *not* that of the light source, *but* that of the undoped ceramic YAG. As mentioned in section 4.2, the "absorption" coefficient (the "*attenuation*" coefficient) defined by eq. (3) includes different effects according to what we take as a reference spectrum. The absorption spectrum using that of a light source includes the Fresnel surface loss at the top and bottom surfaces, scattering at grain boundaries in the ceramics, absorption by the other impurity ions, etc. It may be difficult to separate these effects correctly from the spectra to obtain a net "absorption" coefficient. Therefore, the "absorption" coefficient defined by eq. (3) was used for the discussion in section 4.2 by taking a light source spectrum as a reference. Since the undoped ceramic YAG was sintered simultaneously with the Pr:YAG, Nd:YAG, and Er:YAG, such effects as mentioned above seems to be almost the same for these four YAG ceramics. It may be better to take the spectrum of the undoped YAG ceramic as a reference spectrum than that of the light source since this will give a net "absorption" coefficient for the RE:YAG ceramics, and may be suitable to reveal the spectroscopic properties of the doped RE ions from the optical spectra. In the following discussion, we consider only the spectra by taking the spectrum of undoped ceramic YAG as a reference, only except the Eu:YAG ceramic which will be discussed below. We will re-define the absorption" coefficient in the following subsection. The absorption coefficient at wavelengths where the doped ions have no absorption lines (the background absorption), is 0.15, 0.25, and 0.35 cm^{-1} for Pr:YAG, Nd:YAG, and Er:YAG ceramics, respectively. The background "*attenuation*" coefficient defined by eq. (3) of Pr:YAG, Nd:YAG, and Er:YAG ceramics is 1.03, 1.13, and 1.23 cm^{-1}, respectively.

The Eu:YAG ceramic was prepared by setting the same conditions to the other ceramic YAGs, but sintered at a different time as mentioned earlier. However, the real sintering conditions of Eu:YAG may not exactly the same as those of the other ceramic YAGs. Therefore, the absorption spectrum of Eu:YAG ceramic is drawn with reference to that of the light source (the "*attenuation*" coefficient). Further, the absorption is so weak for the Eu:YAG ceramic that the excitation spectrum was also measured. The emission spectrum and the absorption and excitation spectra of Eu:YAG ceramic are shown in Figs. 31 and 32, respectively.

4.4.1 Undoped $Y_3Al_5O_{12}$ ceramic

Table 6 shows the absorption coefficient of the undoped ceramic YAG together with the refractive index, the Fresnel loss factor, and the absorption coefficient of an undoped FZ single-crystal YAG at representative wavelengths. The refractive indices are the values reported by Bond[112] except those with an asterisk, which are interpolated by a polynomial function using the reported values. In the transmission measurement for the absorption spectra, the Fresnel surface loss must be taken into consideration. We will re-define the absorption coefficient in place of eq. (3) as

$$\alpha(\lambda) = -L^{-1} \ln [I(\lambda) / I_0(\lambda)\, T(\lambda)^2], \qquad (7)$$

where $I(\lambda)$ denotes transmitted light intensity through the sample at wavelength λ, $I_0(\lambda)$ is that of incident light, $T(\lambda)$ is the correction factor by Fresnel loss, and L denotes sample thickness. The Fresnel surface loss $\beta(\lambda)$ under the assumption of normal incidence and no absorption can be expressed as[122]

$$\beta(\lambda) = [(n(\lambda) - 1)^2] / [(n(\lambda) + 1)^2], \qquad (8)$$

where $n(\lambda)$ is the refractive index at wavelength λ. The correction factor $T(\lambda)$ is equal to $1 - \beta(\lambda)$.

The difference between the absorption coefficient of the undoped ceramic YAG, $\alpha_{YAG}(\lambda)$, with the correction of Fresnel loss of eq. (7) and that of FZ single-crystal YAG, $\alpha_{FZ}(\lambda)$, is almost constant with a mean value of 0.258 cm^{-1} and a standard deviation of 0.019 cm^{-1} for 2251 data points between 400 and 850 nm. This value of the absorption coefficient gives, e. g., transmittance of 97.5 % for a sample of 1 mm thickness.

The absorption coefficient $\alpha_{YAG}(\lambda)$ is almost independent of wavelengths. From this fact, Weber[123] suggests that the difference between the absorption coefficients of the ceramic and single-crystal YAGs is due to light scattering at grain boundaries in the ceramic. From the photograph of Fig. 27, one can observe a few layer distortions of the atomic arrangement at around the grain boundary. It is doubtless that some scattering occurs in the ceramics. In fact, by inserting the ceramic YAG into a He-Ne laser light path to surface normal, we can see the light path of the laser in the ceramic from the direction rectangular to the light path. On the other hand, the light path can almost not be seen for the single-crystal YAG. However, it is not clear that the background absorption is only due to the scattering at grain boundaries.

4.4.2 Pr:$Y_3Al_5O_{12}$ ceramic

Figure 28 shows the absorption spectrum of Pr-doped YAG (Pr:YAG) ceramic together with those of Nd:YAG and Er:YAG ceramics. (see Table 7.) Figure 29 displays the emission spectrum of ceramic Pr:YAG in the visible wavelength region between 400 and 700 nm [visible (VIS) spectrum] together with those of Nd:YAG and Er:YAG ceramics. The spectral response of the measuring system was corrected by making use of a standard lamp. The spectra were normalized against the strongest peak of Pr:YAG at 611.3 nm (16359 cm^{-1}). The broad shoulder at around 400 nm in the three spectra is due to leakage of the excitation light source. Figure 30 shows the emission spectrum of Pr:YAG ceramic in the region between 640 to 1100 nm [infrared (IR) spectrum] together with those of Nd:YAG and Er:YAG ceramics. These spectra were also corrected using the standard lamp. The spectra in the 640-700-nm wavelength region overlap with those in Fig. 29 and overall spectral intensities can be read out.

Optical spectra and energy-level structure of Pr^{3+} ion have been reported, for example, in $LaCl_3$,[124] YF_3,[125] $LiYF_4$,[126-128] CaF_2,[129] Y_2O_2S,[130] and $K(Pr,Y)P_4O_{12}$.[131] It is known that the Pr^{3+} ion is the most sensitive to host materials among trivalent RE ions except the Ce^{3+} ion.

The emission and absorption of Ce^{3+} ion are due to transitions between 4f and 5d configurations which largely depend on the host materials. In fact, some transition energies of Pr^{3+} ion differ, e.g., by 80–650 cm^{-1} between $LaCl_3$[124] and $LiYF_4$[127] hosts calculated from the reported energy-level structures. These differences for the Pr^{3+} ion are very large compared with the other trivalent RE ions whose transition energies generally agree within about 100 cm^{-1} for different host materials.

From the absorption and emission spectra, the energy of $^3P_0$ level is determined to be 20473 cm^{-1}, which is almost equal to the value of 20475 cm^{-1} for Pr:$LaCl_3$,[124] but differs significantly from 20860 cm^{-1} of Pr:$LiYF_4$[126] and 20790 cm^{-1} of Pr:CaF_2.[129] However, the energies of lower multiples are not necessarily close to those of Pr:LaF_3; e. g., the energies of the two Stark levels of $^3F_2$ multiplet are 5153 and 5330 cm^{-1} in the ceramic Pr:YAG, although those in Pr:LaF_3[129] are 4950 and 4922 cm^{-1}. Thus, the energy-levels of Pr^{3+} ion are very sensitive to the host materials. Overall assignment of the emission peaks in Figs. 29 and 30 is given in Table 8. This is rather tentative because comparable crystal-field calculations have not been available for the Pr^{3+} ion in YAG. Depending on the Stark-splitting of multiplets, some transition energies between the Stark levels of the multiplets may fall in the wavelength region of the other group of the transitions between different multiplets.

By assuming closure principles and multiplet-splitting of excited-state configurations being negligible compared with the energies of the $4f^n$ configurations as a whole, Judd[63] and Ofelt[64] presented a theory which determines the relative intensities of peaks in an emission spectrum in terms of only three parameters using tensor operator algebra (Judd-Ofelt theory) as mentioned in chapter 2. According to the Judd-Ofelt theory,[63,64] the matrix element of an electric dipole transition is proportional to the summation of terms such as

$$\begin{pmatrix} 1 & t & k \\ p & -q-p & q \end{pmatrix} \cdot \begin{pmatrix} J & t & J' \\ -J_z & +q+p & J_z' \end{pmatrix} \cdot T(t), \qquad (9)$$

where parenthesis denotes a three-j symbol, J is total angular momentum, k and q correspond to those in the crystal-field parameter B_{kq}, p is polarization of transition, and T(*t*) is a tensor operator related to the electric dipole transition probability. From the nature of the three-j symbol, the summation of eq. (9) conveys itself selection rules such that the electric- dipole transitions from the multiplet with total angular momentum J = 0 to multiplets with odd J momentum are forbidden and to those with even J are allowed.[63] This is a guiding principle to assign the peaks to the transitions in $4f^2$ configuration of Pr^{3+} ion together with the reported energy-level structures. In fact, the transition intensities are strong from $^3P_0$ to $^3H_4$ (at around 487 nm), to $^3H_6$ (at around 610 nm) in Fig. 29 and to $^3F_2$ (at around 710 to 740 nm) in Fig. 30, although those are weak from $^3P_0$ to $^3H_5$ (at around 550 nm) and to $^3F_3$ (at around 690 nm) in Fig. 29. In Pr:Y_2O_2S, the transitions to odd J multiplets were reported to be fairly strong, however, Hoshina[130] concluded that this is due to strong J mixing effect of Pr^{3+} ion in the Y_2O_2S host. Since the emission intensities to odd J levels are weak for Pr:YAG ceramic in Fig. 29 and 30, the J mixing effect seems to be small in the ceramic.

4.4.3 Nd:$Y_3Al_5O_{12}$ ceramic

The absorption spectrum of Nd-doped ceramic YAG is shown also in Fig. 28 by shifting the zero level by 2 cm^{-1} from the horizontal axis. The emission spectrum at around VIS-wavelength region is shown in Fig. 29 together with Pr:YAG and Er:YAG ceramics, and the zero level of emission spectrum is also shifted by one vertical division to show the spectrum clearly. The spectrum is so weak compared with the Pr:YAG ceramic that it is drawn multiplied by a factor of 10. The emission spectrum at the IR-wavelength region is shown in Fig. 30 by shifting the zero emission level by one vertical division and multiplied by a factor of 2. The resultant zero levels are shown as short horizontal bars in the figures.

The peak positions, linewidths, and relative peak intensities in Figs. 28-30 are almost exactly the same as those of the spectra of the Nd:YAG ceramics under former synthetic conditions as described in section 4.2. This fact shows good reproducibility of our ceramics and that the value of the induced emission cross section is comparable to those of CZ and FZ single crystals as discussed in section 4.3. However, the background absorption has been considerably reduced from 3.5–4 cm^{-1} of the ceramics under former synthetic conditions[121] to 1.2 cm^{-1} of this ceramic[132] without subtracting Fresnel surface loss, etc. It is noted that the spectrum in Fig. 28 is drawn with reference to the spectrum of the undoped ceramic YAG as discussed at the beginning of this section, and the value of the background absorption coefficient is 0.25 cm^{-1} after subtracting the Fresnel loss. A detailed discussion on the spectroscopic properties such as line number of transitions, line shapes, assignment of the peaks, etc. was described in section 4.2 and will not be discussed further.

Here, we will briefly discuss the comparison of the observed energy-level structure of lower multiplets of our Nd:YAG ceramic with that reported for the CZ single-crystal Nd:YAG by Koningstein and Geusic.[28] As described in chapter 2, they used a Hamiltonian proposed by Dillon and Walker[36] for the crystal-field calculations as

$$\begin{aligned} H_{cryst} = \alpha \cdot [\, A_2^{0} \cdot Y_2^{0} \; + \; A_2^{2} \cdot (Y_2^{+2} + Y_2^{-2}) \,] \\ + \beta \cdot A_4^{0} \cdot [\, Y_4^{0} + 5\delta \cdot (Y_4^{+4} + Y_4^{-4}) \,] \\ + \gamma \cdot A_6^{0} \cdot [\, Y_6^{0} - 21\varepsilon \cdot (Y_6^{+4} + Y_6^{-4}) \,], \end{aligned} \qquad (10)$$

where Y_k^q are spherical harmonics, coefficients α, β, and γ denote operator equivalent constants defined by Stevens, Elliot, and Judd.[20-22] A_k^q is related to the crystal-filed parameter B_{kq} through $A_k^q = \langle r^n \rangle B_{kq}$ with radial integral $\langle r^n \rangle$. The constants δ and ε are defined as

$$\delta = A_4^4 / 5 \cdot A_4^0 \text{ and } \varepsilon = A_6^4 / 21 \cdot A_6^0.$$

They made crystal-field calculations using the Hamiltonian by solving secular equations for $^4F_{3/2}$, $^4I_{9/2}$, and $^4I_{11/2}$ multiplets, and optimized the parameters A_k^q to obtain best overall fit between the observed and calculated Stark-splitting for the single-crystal Nd:YAG.[28] We compared our Stark-splitting schemes (denoted by "obs") of the ceramic Nd:YAG with their calculations expressed as "calc" in Fig. 31, in which the splitting is calculated from the drawings in their publication[28] since no numerical values are available. Although their calculations, of course, were made to optimize their measured values, fit of our splitting scheme to their calculations is found to be almost the same as or slightly better than the fit of their data to the calculations. It is well known that the B_{20} parameter is proportional to the crystal-field strength at the doped-ion site, however, the physical meanings of the other B_{kq} parameters in the crystal-field calculations are not so clear. Therefore, we will give no further discussion on this problem.

Next, we consider the population inversion threshold of simple Fabry-Pérot-type laser oscillator for the ceramic and single-crystal YAGs. According to Yariv,[133] population inversion condition is expressed as

$$\Delta N_t = 8\pi n^2 \cdot t_{spont} \, [\alpha - ln\,(r_1 \cdot r_2)/L\,]/\lambda^2, \tag{11}$$

where t_{spont} is spontaneous emission lifetime, α is the absorption coefficient, r_1 and r_2 are square roots of the reflectivity of the cavity mirrors, L is a laser resonator length, and λ denotes laser oscillation wavelength. For pulsed laser oscillation, the reflectivity of the mirrors is typically taken as 1.00 and 0.96 and results in $ln(r_1 \cdot r_2) = -0.020$. For a typical laser rod of 4 mmϕ and 60 mm long, the second term in the brackets of eq. (11) becomes 0.0034 cm^{-1}.

As for the FZ single-crystal Nd:YAG,[88] the background absorption coefficient α is calculated to be 0.022 cm^{-1}. This value of 0.022 cm^{-1} for the single-crystal Nd:YAG is larger than the reflective loss by about 1 order of magnitude. Therefore, the population inversion condition is mainly governed by the background absorption. The background absorption coefficient of the ceramic Nd:YAG is 0.25 cm^{-1} as described earlier. By adding the difference of the absorption coefficients between the undoped ceramic YAG and the single-crystal YAG of 0.258 cm^{-1}, the total absorption coefficient of the ceramic Nd:YAG becomes 0.51 cm^{-1}. Thus, the threshold of the population inversion of the ceramic Nd:YAG becomes about 25 times larger than that of the single-crystal Nd:YAG.

As discussed at the beginning of this section, the "absorption" coefficient re-defined by eq. (7) includes not only the absorption by impurities, but also light scattering, etc. The light scattering plays an important role in the attenuation of the ceramic YAGs because they consist of many microcrystals with grain boundaries at which light scattering may occur.[123] It is concluded that further reduction of scattering of the ceramic Nd:YAG is necessary to realize a comparable laser oscillation threshold to single-crystal Nd:YAG. However, preliminary measurement of the thermal conductivity of the ceramic YAG is found to be very close to that of single crystal. Therefore, this Nd:YAG ceramic may be able to be used, for example, as a laser amplifier in place of Nd glass, even for the present degree of transparency.

4.4.4 Er:$Y_3Al_5O_{12}$ ceramic

The absorption spectrum of Er-doped ceramic YAG is also shown in Fig. 28 together with Pr:YAG and Nd:YAG ceramics, but the zero level is shifted by 4 cm^{-1} to show the spectrum separately. The emission spectra of VIS- and IR-wavelength regions are shown in Figs. 29 and 30 by shifting the zero levels by two vertical divisions. The resultant zero levels are shown as short horizontal bars in the figures. Since the VIS emission intensity is weak compared with that of Pr:YAG ceramic, the spectrum is drawn by multiplying to the original one by a factor of 5.

Together with the Nd^{3+} ion, the spectra and energy-level structures of Er^{3+} ion in various solids and liquids have been intensively investigated to establish crystal-field theory by the operator equivalent method[20-23] and the tensor operator technique[24-33] as described in chapter 2. The Er^{3+} ion has 11 4f electrons, but the configuration is complementary to the $4f^3$ of Nd^{3+} ion and is accordingly simple to treat theoretically. Different from the Pr^{3+} ion, the energy levels of Er^{3+} ion are not so affected by host materials such as $LaCl_3$,[24-26,134] YAG,[30] $Er_3Al_5O_{12}$,[31], KY_3F_{10},[32] $Er_2Ge_2O_7$,[33], Y_2O_3,[135,136] and $LiYF_4$.[128,137] The energy levels of Er^{3+} ion in these host materials agree with each other within 94 cm^{-1}, which value is common for the trivalent RE ions, except the Ce^{3+} and Pr^{3+} ions as mentioned earlier.

Assignment of the peaks in Fig. 28 to the transitions in $4f^{11}$ configuration is given in Table 11 for the absorption of Er^{3+} ion in the ceramic YAG. As discussed in section 4.1, the degeneracy of the multiplets is completely removed and the number of Stark levels becomes J+1/2 except the Kramers doublet due to the lower D_2 site symmetry.[138]

However, one can see the numbers of transitions between some multiplets and the ground $^4I_{15/2}$ multiplet are more than expected J+1/2 in the table. This is simply because that the experiments were carried out at room temperature. Using the transition energies from the ground $^4I_{15/2}$ and the excited $^4S_{3/2}$ multiplets, the energies of the second- and third-lower Stark levels of the ground multiplet are calculated to be 19 and 79 cm^{-1} from the lowest level, respectively. At room temperature, the electron population of the third-lower Stark level is still 0.68 time as large as that of the lowest level of the ground $^4I_{15/2}$ multiplet. Therefore, the transitions from the lowest-, second-lowest, and even third-lowest Stark levels can be observed at room temperature. The transition energies from the lowest ground level are in good agreement with the values of the single-crystal Er:YAG[30] within 30 cm^{-1} considering the latter was measured at 4.2 °K.

Assignment of the emission peaks in Figs. 29 and 30 to the transitions in $4f^{11}$ configuration is given in Table 12 for the emission of Er^{3+} ion in the ceramic YAG. The peak energies of the transitions between multiplets are also given in the table in the unit of cm^{-1}. These values of the peak energies are in good agreement with the reported values for the other hosts[24-26,30-33,128,134-137] within 100 cm^{-1}. The Stark-splitting is largely dependent on the site symmetry of the host materials. Fortunately, the Stark-splitting of Er^{3+} ion in single-crystal YAG has been reported by Koningstein and Geusic.[30] We will construct Stark-splitting scheme for Er^{3+} ion in the ceramic YAG and compare with that of the single-crystal Er:YAG.[30] Since the spectra were measured at every 0.1 nm, the uncertainty of the peak energies is less than 4 cm^{-1} at 500 nm.

Together with the absorption peak energies in Table 12, we can construct the energy diagram of the Stark levels for some multiplets of Er^{3+} ion. The results are shown in Figs. 32 and 33. In the figures, "obs" denotes the experimental values and "calc" is the values of the crystal-field calculation made by Koningstein and Geusic.[30] The Stark-splitting of $^4S_{3/2}$, $^4F_{9/2}$, $^4I_{9/2}$, and $^4I_{15/2}$ is determined in consistent with the transition energies in both absorption and emission spectra. The discrepancy of the calculation is less than 3 cm^{-1}, which is within the uncertainty of measurements of 4 cm^{-1}. That of the other multiplets can be calculated from the emission or absorption spectra using the determined energies of $^4I_{15/2}$ Stark levels. The energies of each zero level of the multiplets from the lowest-level of the ground $^4I_{15/2}$ multiplet are 22202, 20483, 19084, 18348, 15284, 12313, 10252, and 6775 cm^{-1} for $^4F_{5/2}$, $^4F_{7/2}$, $^2H_{11/2}$, $^2S_{3/2}$, $^4F_{9/2}$, $^4I_{9/2}$, $^4I_{11/2}$, and $^4I_{13/2}$ multiplets, respectively. The corresponding energies reported for the single crystal[30] are 22230, 20520, 19100, 18406, 15290, 12298, 10252, and 6766 cm^{-1}, respectively. Thus, the energies of the lowest Stark levels in the ceramic are in good agreement with those of the single crystal within about 30 cm^{-1}.

The energies of the Stark-splitting of some multiplets in the single crystal were reported not in numerical values but in drawings[30] similar to the case of the single-crystal Nd:YAG. Comparing with them, the overall feature of the Stark-splitting of the ceramic Er:YAG is very close to that reported for the single-crystal Er:YAG.[30] The Stark-splitting energy between two levels of $^4S_{3/2}$ multiplet, for example, is 66 cm^{-1}, which is slightly smaller than the reported value of 70 cm^{-1} for the single-crystal Er:YAG calculated from the drawing.[30] The other Stark-splittings of the multiplets are in fairly good agreement with those reported for the single-crystal Er:YAG at 4.2 °K.[30]

4.4.5 Eu:$Y_3Al_5O_{12}$ ceramic

Finally, we will report and discuss the optical spectra of Eu-doped ceramic YAG. Figure 34 shows the emission spectrum of Eu:YAG ceramic in the 570-720-nm wavelength region. The optical investigation on single-crystal Eu:YAG was done by Koningstein,[29] but visual spectra were not reported. We cannot compare the overall spectrum of Eu:YAG ceramic with that of the single crystal. The assignment of stronger peaks to the transitions in 4f^6 configuration is shown in the figure and the detailed assignment of the emission peaks is given in Table 13. The observed transition energies are in good agreement with those of the single-crystal Eu:YAG[29] within 8 cm^{-1}.

Figure 35 shows the absorption spectrum of the Eu:YAG ceramic (lower spectrum). It is noted that the true expression for the vertical axis may be "*attenuation*" coefficient from the reasons discussed at the beginning of this section, however, the "absorption" coefficient is used for simplicity. As mentioned earlier, the excitation spectrum was also measured. The detection wavelengths for the excitation spectra were 590 nm ($^5D_0$ to $^7F_1$ transition of Eu^{3+} ion) and 610 nm ($^5D_0$ to $^7F_2$ transition). Both spectra were the same except relative peak intensities, and only the spectrum with 590-nm detection is shown in the figure by shifting the zero emission level (upper spectrum).

Comparing the absorption and excitation spectra, many missing or weak peaks in the absorption spectrum appear in the excitation spectrum. However, the linewidths are very broad in the excitation spectrum compared with those in the absorption spectrum. This is mainly due to larger slit widths with 60-90 μm for the excitation measurements. The light intensity from the Xe arc lamp through the monochromator was so weak that it was necessary to enlarge the slit widths. At the same time, a phonon-assisted transition might be also another reason for line broadening in the excitation spectrum. Peak energies in the excitation and absorption spectra and the assignment of the peaks are given in Table 14. They are in very good agreement with those reported for the single-crystal Eu:YAG by Koningstein[29] within 3 cm^{-1}.

In general, a crystal-field calculation of Eu^{3+} ion is rather difficult because the number of basis functions of $4f^6$ configuration is as many as 119.[45] Further, the lower-site symmetry of Eu^{3+} ion in YAG results in a larger number of crystal-field parameters. The calculation may have many local minima. Koningstein made the crystal-field calculation assuming that the Eu^{3+} ion site had higher tetragonal symmetry (D_{2d}) with only six crystal-field parameters.[29] Agreement between the observed and calculated levels was not so good. At present, we can only make a crystal-field calculation of $4f^3$ (and the complementary $4f^{11}$) configuration for the restricted point symmetries. We could not recalculate the crystal-field calculation of Eu^{3+} ion in YAG for the true symmetry of C_2.[35]

Because of the difficulty of the crystal-field calculation, higher-energy levels at the ultraviolet-wavelength region could not be assigned to the transitions in $4f^6$ configuration in the Table 14.

In the emission spectrum, it is noteworthy that the emission intensity of $^5D_0$ to $^7F_1$ (0-1) transitions is about three times as large as that of $^5D_0$ to $^7F_2$ (0-2) transitions and the emission intensity is considerably intense for the $^5D_0$ to $^7F_4$ (0-4) transition. It is known that the 0-1 transition is due to a magnetic-dipole transition[64] and almost insensitive to the local-site symmetry of Eu^{3+} ion. On the other hand, the latter 0-2 and 0-4 transitions are due to a forced electric-dipole transition[64] and the transition probability is largely dependent on the local symmetry of Eu^{3+} ion. When a Eu^{3+} ion site has an inversion symmetry, the 0-2 transition becomes weak, although it becomes strong without any inversion symmetry. In fact, the 0-2 emission intensity of Eu^{3+} ion in $InBO_3$, $ScBO_3$, and $LuBO_3$[139] is extremely small since the Eu^{3+} ion occupies C_{3i} site with inversion symmetry. On the contrary, the 0-2 emission intensity of Eu^{3+} ion is larger than or comparable to the 0-1 emission intensity in Y_2O_3 (C_2 site symmetry),[140,141] in YPO_3 (D_{2d}),[142] in Y_2O_2S (D_{2d}),[130] and in KY_3F_{10} (C_{4v})[32] without inversion. Although the site symmetry was not clearly stated, the 0-1 emission intensity of Eu^{3+} ion is even larger than the 0-2 intensity in Gd_2O_3-B_2O_3 solid solutions[143] and in $NaInO_2$[144] similar to the emission spectrum of the ceramic Eu:YAG.

In the absorption spectrum, an increase of the absorption coefficient can be seen in Fig. 35 at around 280 nm. We have measured the absorption spectrum from 250 nm to 580 nm and found a broad peak from 265 to 305 nm with a 280-nm peak. This broad peak cannot be observed in the excitation spectrum. There could be two possible explanations for this broadband absorption with an about 2-cm^{-1} peak absorption coefficient. First is a charge-transfer state (CTS) of the trivalent Eu ion (Eu^{3+}) to which the oxygen 2p electron is transferred from the ligand. Jørgensen, Pappalardo, and Rittershaus[145] discussed this CTS and the $4f^n5d$ configuration energies for mixed RE_2O_3 (RE = rare-earth ions from Ce to Yb) and the other oxides, and concluded that the $4f^n5d$ energy is smaller than the CTS energy only except Eu and Yb ions.

Blasse[146–148] made extensive investigations of CTS of many oxides and some halides. Although he found that the peak energy of CTS of Bi^{3+} ion decreases with an increase of covalency of Bi^{3+}-ion site in the series of YPO_3, YBO_3, $YAl_3B_4O_{12}$, $CaYBO_4$, $LiYSiO_4$, and Y_2O_3,[148] no systematic change of the CTS energies was found for the Eu^{3+} ion. Ropp[149] reported the stronger CTS excitation bands for the Eu^{3+} ion than the intra-$4f^6$ transitions at 257, 237, and 265 nm for $Eu:LaPO_4$, $Eu:YPO_4$, and $GdPO_4$, respectively. Nakazawa and Shiga[150] carried out detailed experiments in the vacuum-ultraviolet-wavelength region from 100 to 300 nm for the Eu^{3+} ion in YPO_4. They found that diffused reflectance begins to decrease at around 250 nm and there are strong 230-nm and weak 270-nm peaks in the excitation spectrum for the Eu^{3+} ion. As for the garnet host, the peaks at 220 and 235 nm have been only reported for $Y_3Ga_5O_{12}$ crystal.[147]

In general, the CTS band for the trivalent Eu ion is observed in strong and broad band in the excitation spectra together with minima in the diffused reflectance spectra. The peak energy of CTS ranges from about 200 to 430 nm, and the CTS band is generally broad with a larger intensity than intra-$4f^n$ transitions in the excitation spectra. For the ceramic Eu:YAG, the broadband was observed only in the absorption spectrum and no such strong broadband was observed in the excitation spectrum for the trivalent Eu ion.

Another possibility is due to the transition from $4f^7$ to $4f^6 5d$ configurations of the divalent Eu ion (Eu^{2+}). This is because the Eu ion has the tendency to become divalent and the final sintering of the ceramics was done in vacuum, i. e., reduced atmosphere. There have been a number of investigations in the literature concerning the optical spectra of Eu^{2+} ion. Blasse et al.[151,152] have made extensive investigations on the emission, diffused reflectance, and excitation spectra of Eu^{2+} ion in many oxides. The excited state of Eu^{2+} ion is $4f^6 5d$ configuration, which interacts strongly with the surrounding host lattice. Therefore, the emission, absorption or diffused reflectance, and excitation spectra become broadbands and the peak position depends largely on the hosts as well as the CTS bands.

Similar energies of excitation peaks to the absorption peak in the ceramic Eu:YAG have been reported in some oxides. Blasse, Bril, and de Vries[152] reported the 290- and 260-nm excitation peaks for 380-nm emission of Eu:$BaBPO_5$. Machida et al.[153,154] observed excitation peaks of the 250- and 308-nm for 368-nm emission, 250- and 302-nm peaks for 367-nm emission, and 249- and 303-nm peaks for 432-nm emission for the Eu^{2+} ion in SrB_2O_4, SrB_4O_7, and SrB_6O_{12}, respectively. We could not observe any broadband emission peak which may be due to the Eu^{2+} ion in the Eu:YAG ceramic, and no excitation spectrum could be measured for the divalent Eu ion in the ceramic.

Therefore, it is difficult to conclude the origin of the broadband absorption peak at around 280 nm. Although the CTS band for the Eu^{3+} ion is generally observed with stronger intensities in the excitation spectrum for the 0-1 and 0-2 transitions of the trivalent Eu ion, there is no such broad and strong peak in the excitation spectrum of Eu:YAG ceramic. Considering that the sintering condition for preparation of the ceramic YAGs is reduced atmosphere (vacuum), the broadband peak in the absorption spectrum at around 280 nm is presumably due to the transitions from $4f^7$ to $4f^65d$ configurations of Eu^{2+} ion.

Table 6. Optical constants of the undoped ceramic YAG. λ denotes the wavelength in nm. n is the refractive index reported by Bond (Reference 112) and the values with an asterisk (*) are calculated values by the polynomial interpolation. α_{YAG} is absorption coefficient. β is the calculated value of Fresnel surface loss through the refractive index. α_{FZ} denotes the absorption coefficient of undoped single-crystal YAG.

λ (nm)	$n(\lambda)$	$\alpha_{YAG}(\lambda)$ (cm^{-1})	$\beta(\lambda)$	$\alpha_{FZ}(\lambda)$ (cm^{-1})
400	1.8650	1.102	0.0912	0.844
450	1.8532	1.073	0.0984	0.838
500	1.8450	1.084	0.0882	0.837
550	1.8391*	1.072	0.0874	0.834
600	1.8347	1.093	0.0867	0.832
650	1.8316*	1.081	0.0863	0.833
700	1.8285	1.108	0.0858	0.829
750	1.8270*	1.104	0.0855	0.830
800	1.8245	1.107	0.0852	0.828
850	1.8232*	1.090	0.0850	0.827

Table 7. Assignment of the absorption peaks of Pr:YAG ceramic. The spectrum is shown in Fig. 28.

Wavelength (nm)	Peak energy (cm^{-1})	Assignment (from ground $^3H_4$)
443-453	22563, 22292, 22252, 22099, 22060	to $^3P_2$
457-463	21863, 21801, 21659, 21608	to $^1I_6$
473-481	21142, 21106, 21030, 20982, 20790	to $^3P_1$
487-488	20525, 20475	to $^3P_0$
581-611	17215, 17036, 16880, 16829, 16410, 16388, 16356	to $^1D_2$

Table 8. Assignment of the emission peaks of Pr:YAG ceramic. The spectral intensity of the Pr–, Nd– and Er–doped ceramic YAGs is normalized against the most intense peak with an asterisk in the table. The intensity for the group is abbreviated as S for strong, M for medium and W for weak. The spectra are shown in Fig. 29 and 30.

Wavelength (nm)	Peak energy (cm^{-1})	Intensity	Assignment
473-483	21139, 21110, 21033, 20982, 20792, 20725, 20691	W	$^3P_1$ to $^3H_4$
487-488	20532, 20473	S	$^3P_0$ to $^3H_4$
492-509	20292, 20206, 20178, 20133, 20076, 19942, 19885, 19829, 19668	W	$^3P_2$ to $^3H_5$
529-542	18880, 18836, 18755, 18737, 18681, 18580, 18448	W	$^3P_1$ to $^3H_5$
546-552	18318, 18227, 18182, 18126	W	$^3P_0$ to $^3H_5$
557-566	17945, 17912, 17762, 17663	W	$^3P_2$ to $^3F_2$
580-603	17218, 17036, 16880, 16827, 16787, 16573	W	$^1D_2$ to $^3H_4$
607-612	16450, 16412, 16392, 16359*	S	same above
614-630	16268, 16219, 16186, 16116, 16075, 15960, 15884	M	$^1D_2$ to $^3H_4$
637-639	15679, 15662	W	$^3P_1$ to $^3F_2$
650-664	15379, 15202, 15161, 15076	M	$^3P_0$ to $^3F_2$
688-709	14529, 14469, 14331, 14288, 14266, 14233, 14200, 14168, 14136, 14110	W	$^3P_0$ to $^3F_3$
713-763	14023, 14002, 13965, 13931, 13825, 13714, 13691, 13641, 13556, 13493, 13426, 13396, 13224, 13184, 13111	S	$^3P_0$ to $^3F_4$

Table 8. (cont'd)

Wavelength (nm)	Peak energy (cm^{-1})	Intensity	Assignment
820-840	12097, 12065, 11947, 11837	M	$^1D_2$ to $^3F_2$
900-960	11074, 11024, 10993, 10960, 10922, 10811, 10730, 10520, 10457	W	$^1D_2$ to $^3F_3$
1002-1044	9974, 9922, 9905, 9782, 9717, 9609, 9606, 9577	W	$^1D_2$ to $^3F_4$

Table 9 Assignment of the absorption peaks of Nd:YAG ceramic. The spectrum is shown in Fig. 28

Wavelength (nm)	Peak energy (cm^{-1})	Assignment (from ground $^4I_{9/2}$)
481	20755	to $^2K_{15/2}$
516-538	19365, 19183, 18972, 18811, 18615	to $^2K_{13/2}$ + $^4G_{7/2}$ + $^2G_{9/2}$
569-599	17562, 17431, 17256, 17120, 16984	to $^2G_{7/2}$
	16906, 16846, 16714, 15959	+ $^2G_{5/2}$
627	15959	to $^2H_{11/2}$
670-684	14912, 14815, 14784, 14676, 14622	to $^4F_{9/2}$
730-764	13624, 13589, 13565, 13492, 13425	to $^4F_{7/2}$
	13358, 13250, 13226, 13518, 13113	+ $^4S_{3/2}$
777-796	12847, 12617, 12569	to $^2H_{9/2}$
799-814	12516, 12424, 12404, 12364, 12296	to $^4F_{5/2}$

Table 10. Assignment of the emission peaks of Nd:YAG ceramic. The spectra are shown in Fig. 29 and 30.

Wavelength (nm)	Peak energy (cm^{-1})	Assignment (from excited $^4F_{3/2}$)
869-947	11505, 11420, 11371, 11305, 11287	to $^4I_{11/2}$
	11221, 11110, 10653, 10562	
1052-1078	9504, 9477, 9420, 9396, 9361	to $^4I_{9/2}$
	9312, 9277	

Table 11. Assignment of the absorption peaks of Er:YAG ceramic. The wave-length range with an asterisk (*) denotes the peaks not drawn in Fig. 28.

Wavelength (nm)	Peak energy (cm^{-1})	Assignment (from ground $^4I_{15/2}$)
354-358*		to $^2G_{7/2}$
362-368*		to $^2G_{9/2}$
380-383*	26288, 26247, 26205, 26178, 26123	to $^4G_{11/2}$
404-407	24752, 24710	to $^2H_{9/2}$
440-442	22650, 22573	to $^4F_{3/2}$
449-451	22252, 22202	to $^4F_{5/2}$
483-488	20670, 20619, 20542, 20483	to $^4F_{7/2}$
517-526	19335, 19298, 19283, 19260, 19142, 19106, 19084, 19066, 19026, 19011	to $^4H_{11/2}$
542-546	18450, 18430, 18382, 18308	to $^2S_{3/2}$
645-658	15509, 15489, 15466, 15446, 15389, 15352, 15333, 15301, 15284, 15263, 15249, 15230, 15207	to $^4F_{9/2}$
780-812	12821, 12818, 12314	to $^4I_{9/2}$

Table 12. Assignment of the emission peaks of Er:YAG ceramic. The spectrum is shown in Fig. 29 and 30.

Wavelength (nm)	Peak energy (cm^{-1})	Assignment
518-526	19279, 19260, 19033, 19013	$^2P_{3/2}$ to $^4I_{9/2}$
542-561	18450, 18431, 18384, 18308, 18282, 18038, 18028, 17971, 17960, 17928, 17883, 17816	$^4S_{3/2}$ to $^4I_{15/2}$
644-680	15512, 15493, 15463, 15446, 15434, 15350, 15333, 15319, 15307, 15288, 15284, 15263, 15249, 15225, 15056, 14896, 14885, 14873, 14862, 14743, 14717	$^4F_{9/2}$ to $^4I_{15/2}$
780-819	12813, 12795, 12566, 12545, 12515, 12494, 12488, 12357, 12333, 12313, 12293, 12232, 12210	$^4I_{9/2}$ to $^4I_{15/2}$
839-869	11908, 11857, 11850, 11843, 11792, 11786, 11675, 11655, 11609, 11590, 11575, 11509	$^4S_{3/2}$ to $^4I_{13/2}$
960-1033	10413, 10409, 10395, 10390, 10367, 10355, 10348, 10334, 10298, 10292, 10281, 10265, 10252, 10233, 10225, 10208, 10177, 10002, 9946, 9939, 9933, 9888, 9846, 9789, 9687	$^4I_{11/2}$ to $^4I_{15/2}$

Table 13. Assignment of the emission peaks of Eu:YAG ceramic. The spectrum is shown in Fig. 34.

Excitation peak wavelengths (nm)	Absorption peak wavelengths (nm)	Assignment
288.4, 299.9		cannot be assigned
316.4, 320.9, 323.0, 329.4	328.5, 329.4	$^7F_0$ to $^5H_3$
363.2, 367.1	362.5, 363.4	$^7F_0$ to $^5D_4$
375.8, 378.2, 380.4, 382.8, 383.6, 385.0, 386.0, 387.6, 389.7	377.3, 380.3, 382.6, 383.9, 385.0, 385.9, 387.1, 388.9, 389.8	cannot be assigned
395.3, 396.0, 396.9, 398.4, 398.9	394.3, 395.0, 395.8, 396.4, 398.0	$^7F_0$ to $^5L_6$
404.4, 406.2, 407.0	404.9, 405.2, 405.8	$^7F_0$ to $^5D_3$
411.0, 411.8		$^7F_1$ to $^5D_3$
465.4, 466.0, 466.8, 468.2, 469.0	465.6, 466.1, 466.45, 468.05	$^7F_0$ to $^5D_2$
525.8, 526.2, 527.2, 527.7, 528.1, 528.8	526.5, 527.5	$^7F_0$ to $^5D_1$

Table 14. Assignment of the excitation and emission peaks of Eu:YAG ceramic. The spectra are shown in Fig. 35.

Wavelength (nm)	Peak energy (cm^{-1})	Assignment
590.65- 596.55	16391, 16908, 16763	$^5D_0$ to $^7F_1$
595.8 - 597.8	16784, 16728	$^5D_1$ to $^7F_3$
610.0 - 630.8	16393, 16321, 16210, 16197, 15853	$^5D_0$ to $^7F_4$
621.1 - 636.95	16100, 16093, 15999, 15820, 15810, 15700	$^5D_1$ to $^7F_4$
649.8 - 666.6	15389, 15378, 15305, 15260, 15225, 15216, 15002	$^5D_0$ to $^7F_3$
696.1 - 715.7	14366, 14356, 14263, 14085, 14073, 13972	$^5D_0$ to $^7F_4$
715.5 - 718.6	13976, 13926	$^5D_1$ to $^7F_6$

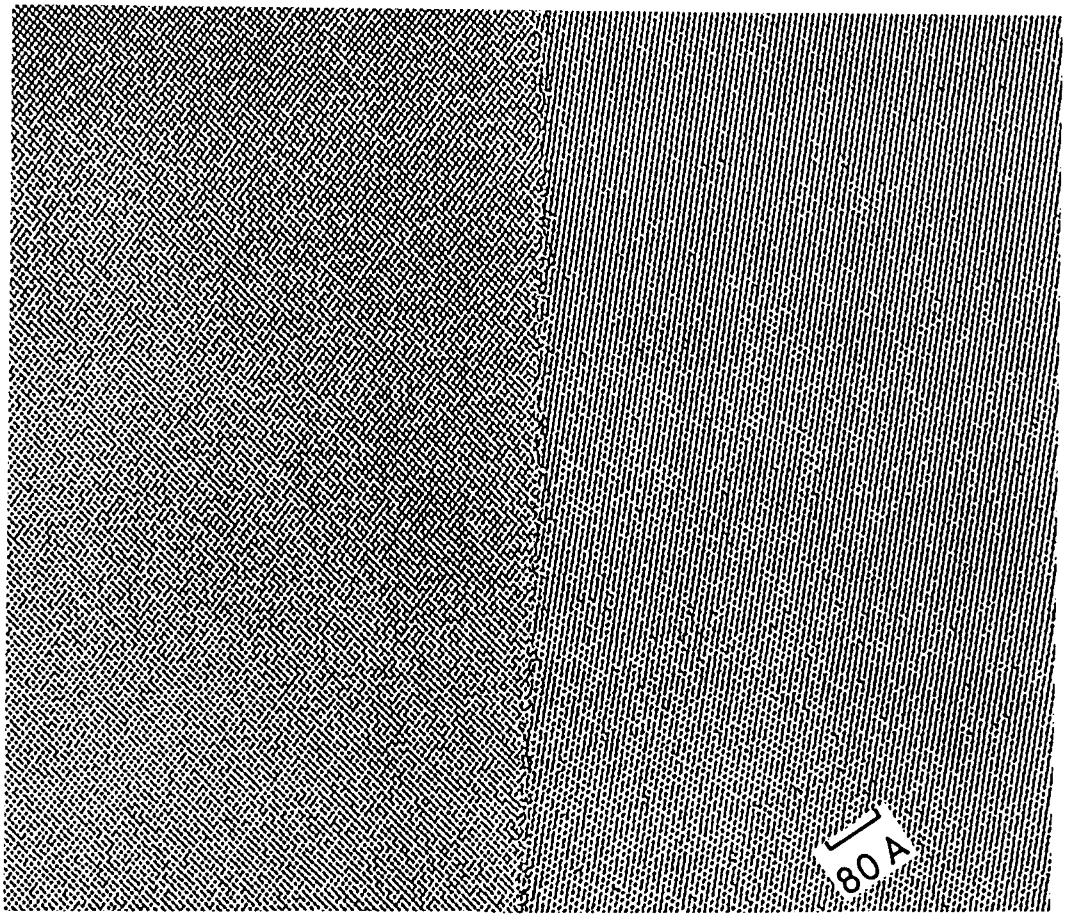

Fig. 27. Transmission electron microscope (TEM) photograph of undoped ceramic YAG at around grain boundary. Dot distance is approximately 8 A and the scale is shown in the photograph. A few layers distortion can be observed at grain boundary.

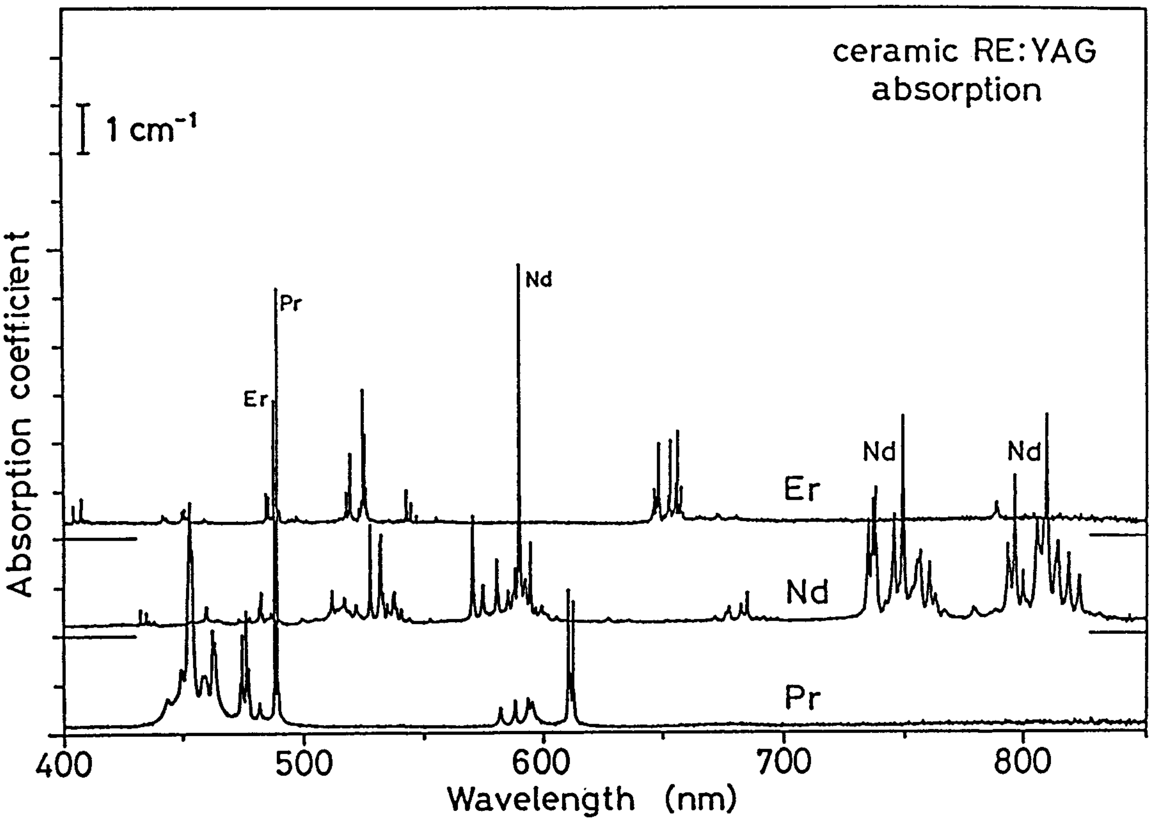

Fig. 28. Absorption spectra of the Pr–, Nd– and Er–doped YAG ceramics at around visible–wavelength region. To show the spectra clearly, the spectra of Nd:YAG and Er:YAG ceramics are shifted the zero levels by 2 and 4 cm^{-1} from that of ceramic Pr:YAG, respectively. The zero levels of both spectra are shown as short horizontal bars in the figure. One division of the vertical scale equals to a 1-cm^{-1} absorption coefficient. It is noted that the spectra are drawn for that of an undoped ceramic YAG as a reference spectrum.

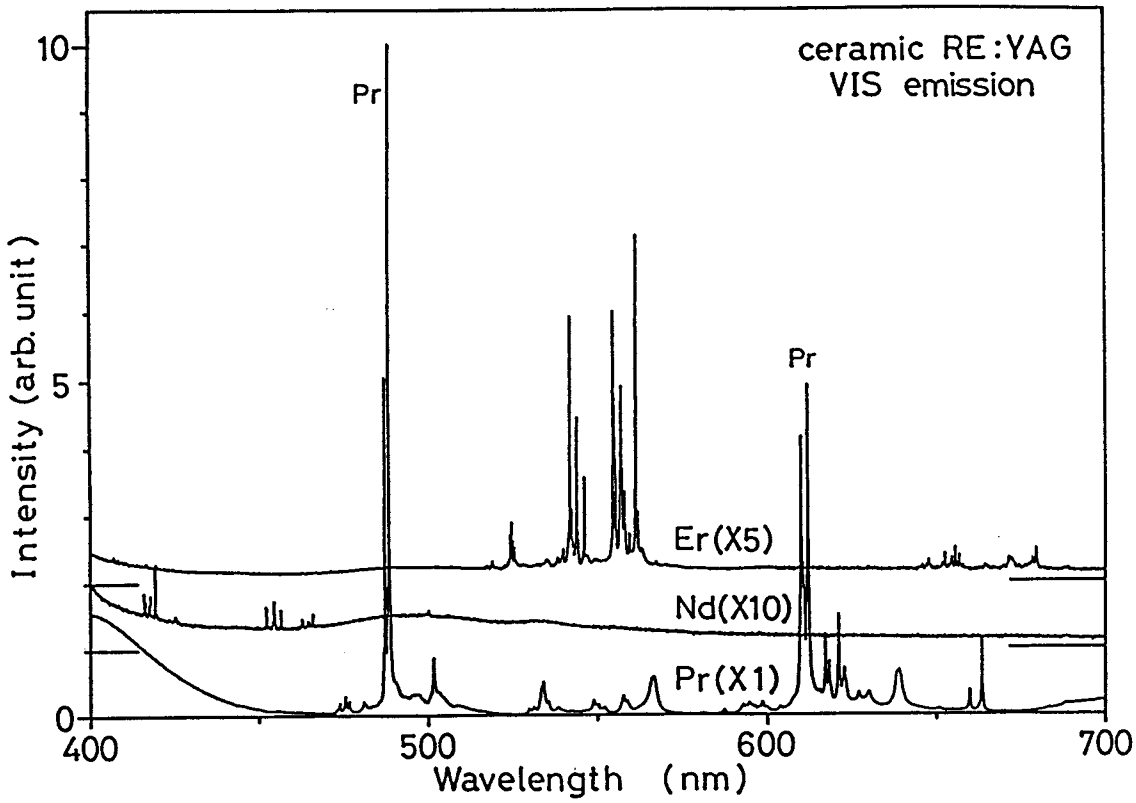

Fig. 29. Emission spectra of the Pr–, Nd– and Er–doped YAG ceramics at around visible–wavelength region. To show the spectra clearly, the zero levels of the spectra of Nd:YAG and Er:YAG ceramics are shifted by one and two vertical divisions from the zero level (short horizontal bars) of the ceramic Pr:YAG, respectively. Intensities are normalized to the most intense peak of the Pr:YAG ceramic. Since the intensities of Nd:YAG and Er:YAG are weak, the spectra are drawn by multiplying the original spectra by factors 10 and 5, respectively. The Spectral response of measuring system was corrected using a standard lamp.

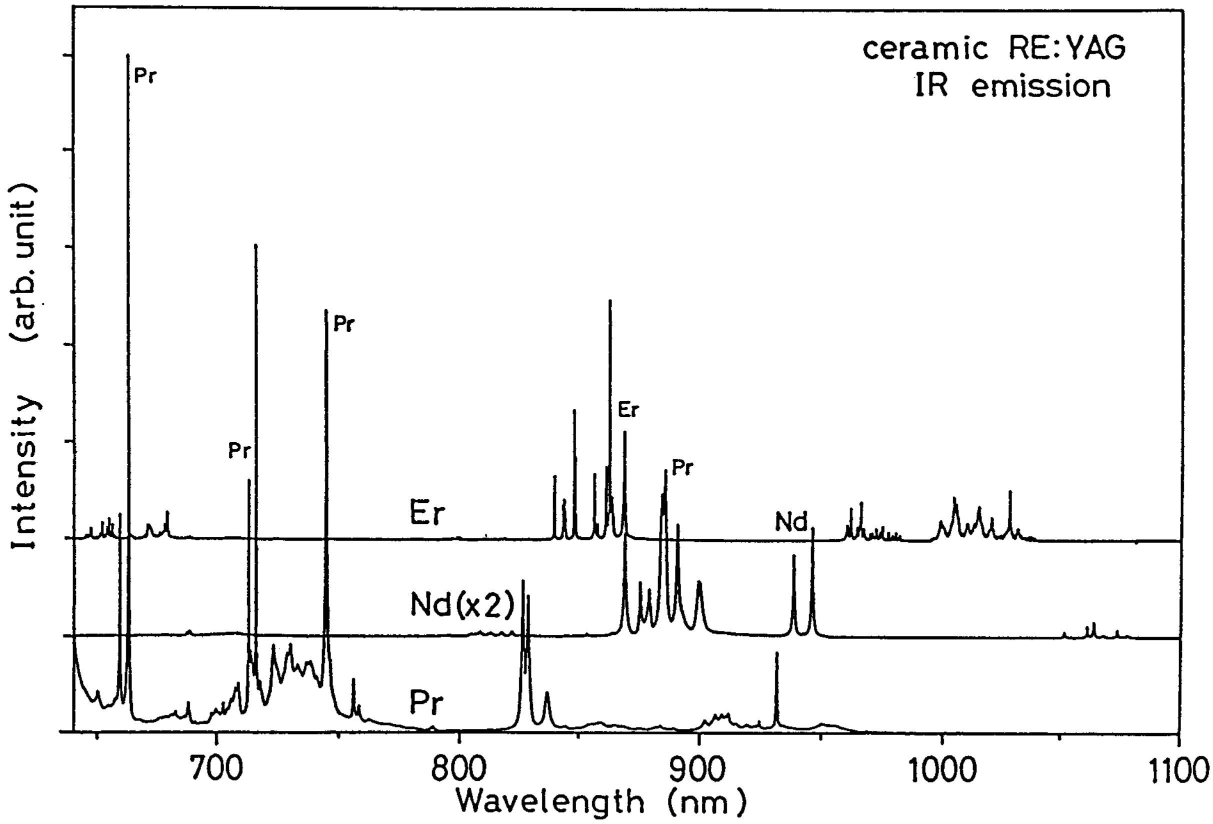

Fig. 30. Emission spectra of the Pr-, Nd- and Er-doped YAG ceramics at near-infrared-wavelength region. The spectra of Nd:YAG and Er:YAG ceramics are shifted by one and two vertical divisions from the zero level (short horizontal bars) of the ceramic Pr:YAG, respectively. Intensities are normalized to the most intense peak of the Pr:YAG ceramic. Since the intensities of Nd:YAG is weak, the spectrum drawn by multiplying the original spectrum by factors 2. The spectral response of the measuring system was corrected using a standard lamp.

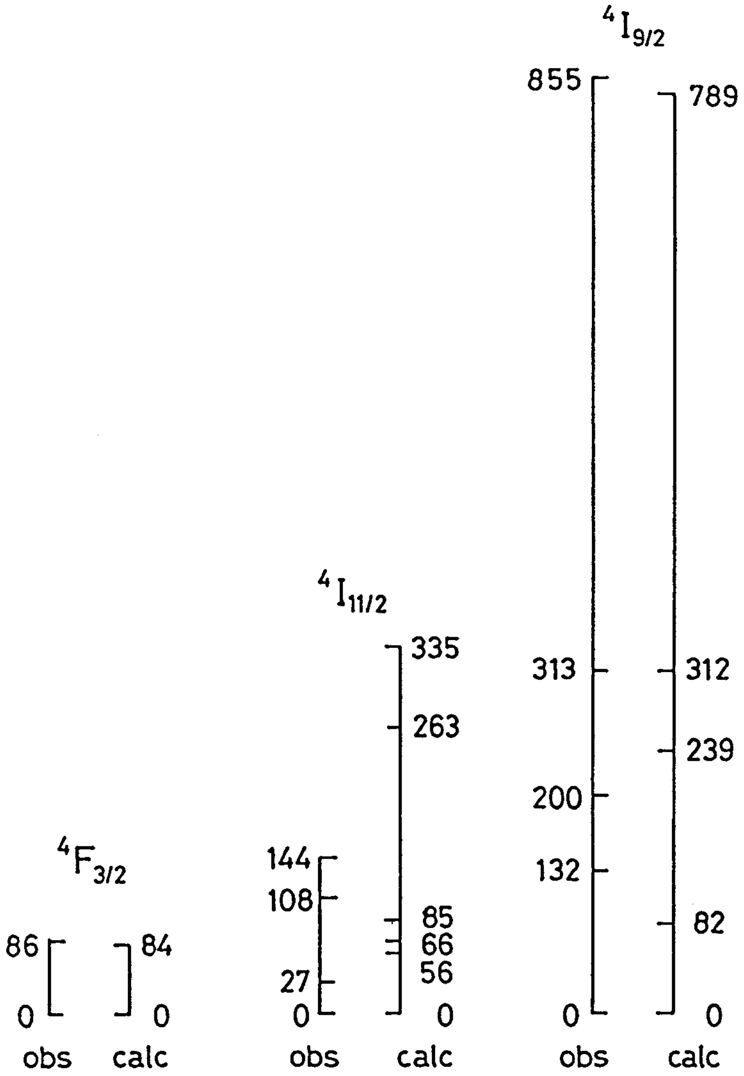

Fig. 31. Stark splitting of some multiplets of ceramic Nd:YAG determined in consistent with peak energies of the absorption and emission spectra. The "obs" denotes the experimental values and the "calc" is the values of crystal field calculation carried out by Koningstein and Geusic (Reference 28).

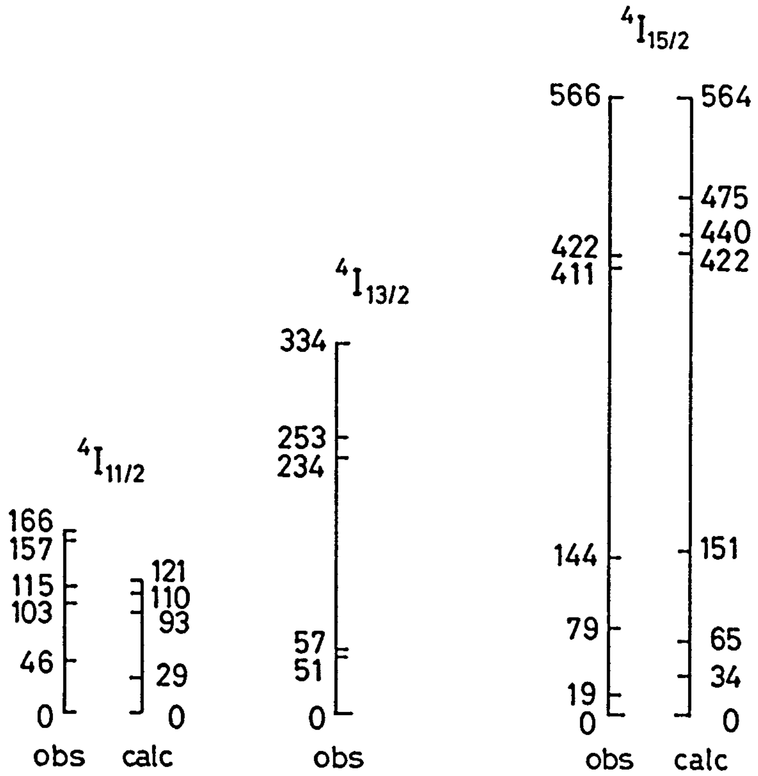

Fig. 32. Stark splitting of ^4I_J multiplets of ceramic Er:YAG. The energies are determined in consistent with peak energies of the absorption and emission spectra. The "obs" denotes the experimental values and the "calc" is the values of crystal field calculation carried out by Koningstein and Geusic (Reference 30).

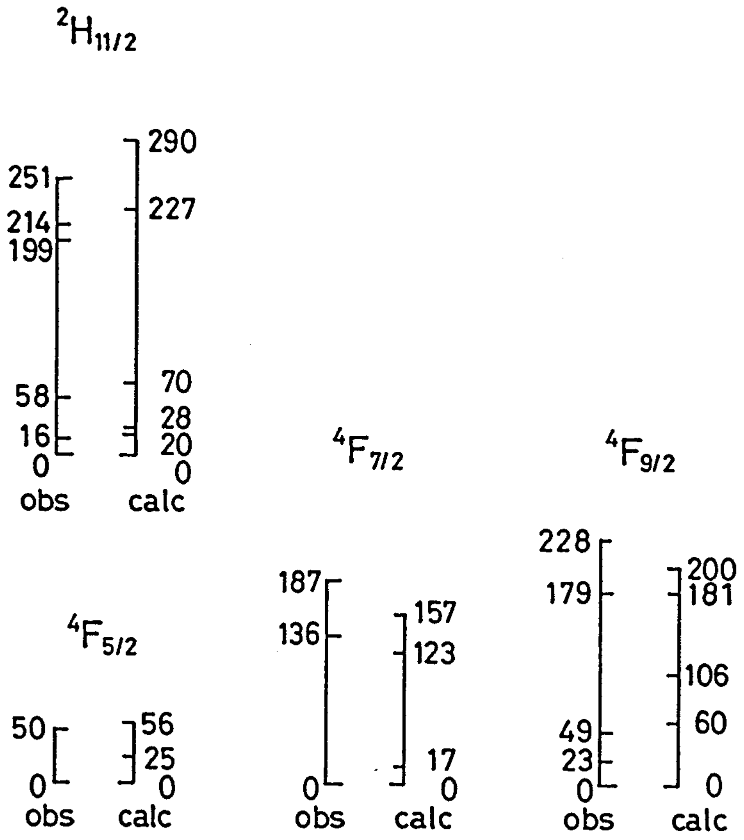

Fig. 33. Stark splitting of $^2H_{11/2}$ and ^4F_J multiplets of ceramic Er:YAG. The energies are determined in consistent with peak energies of the absorption and emission spectra. The "obs" denotes the experimental values and the "calc" is the values of crystal field calculation carried out by Koningstein and Geusic (Reference 30).

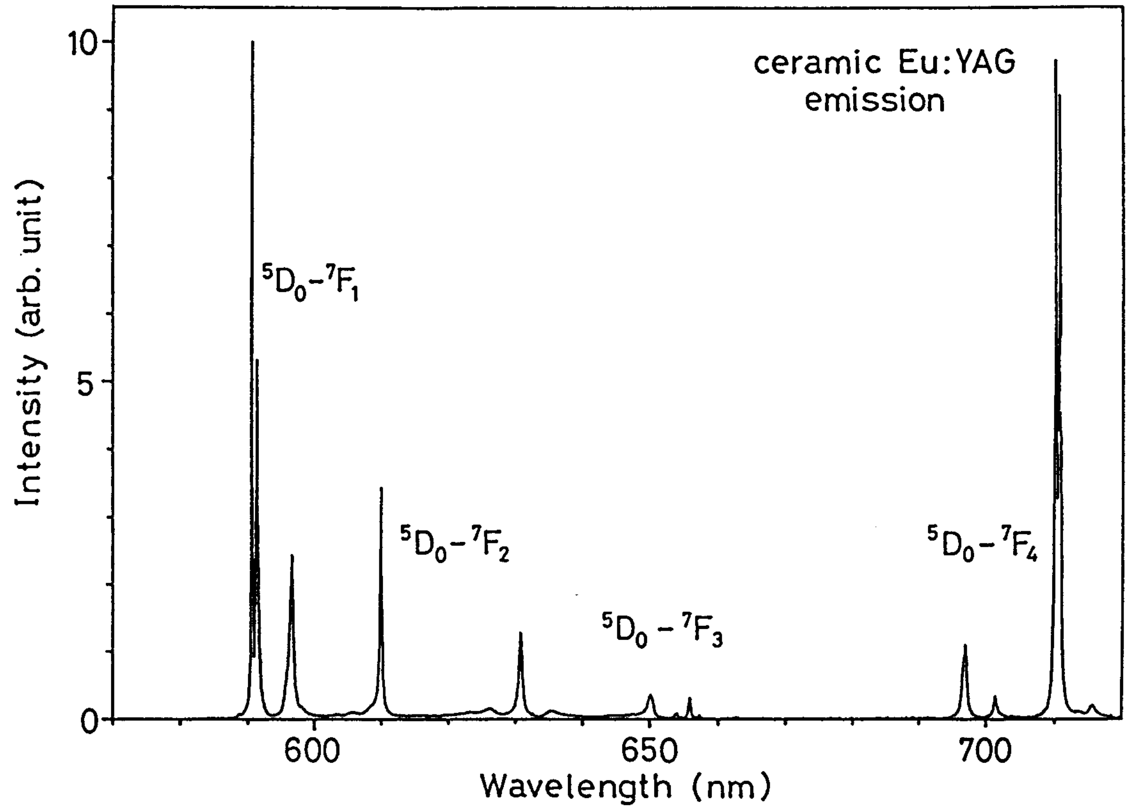

Fig. 34. Emission spectrum of the Eu:YAG ceramic from 580 to 780 nm. The spectral response was corrected by using a standard lamp.

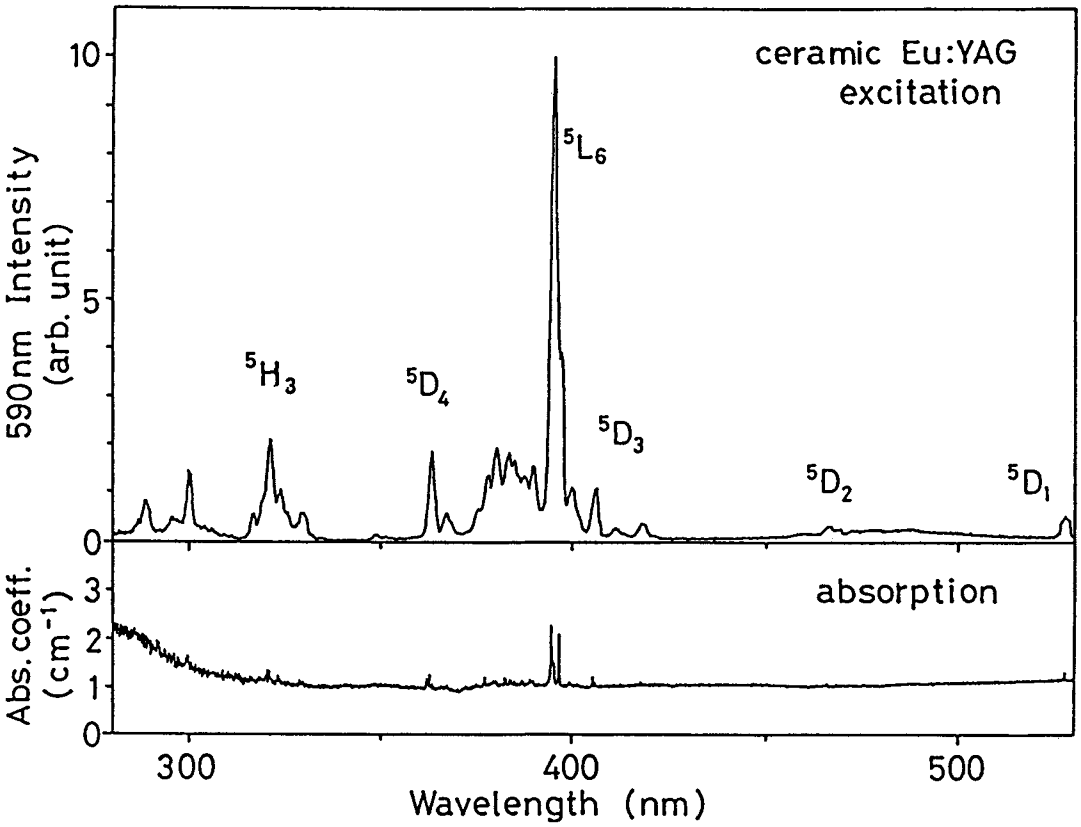

Fig. 35. Excitation and absorption spectrum of the Eu:YAG from 280 to 530 nm. Upper spectrum is an excitation spectrum for the center wavelength of detection at 590 nm ($^5D_0$ to $^7F_1$ transition). Horizontal line denotes the zero level of emission intensity of the 590 nm detection. Spectral response of the measuring system was corrected except that of the detector of an HTV R928 PMT for 280 to 530 nm. Lower one is an absorption spectrum of ceramic Eu:YAG. Blank spectrum is taken as a reference. The background absorption is about 1 cm^{-1}, which includes the Fresnel surface loss, etc.

Chapter 5. Conclusions

In this study, we have reported and discussed two subjects. One is to investigate the effects of the crystalline environment of the YAG hosts on the optical properties of the doped Nd ion in the single crystals grown by the FZ method using the optical image furnace and the transparent ceramics prepared by the urea precipitation method which have been newly developed for the sample preparation. In both cases, the crystal-strain may affect line broadening and line energies of the Nd-ion spectra. The crystal-strain can be introduced through the large temperature gradient at around crystal-melt interface for the single-crystal and the degree of the crystallization of each grain for the transparent ceramics.

No appreciable difference, however, has been observed between the FZ single-crystal and transparent ceramic Nd:YAGs and the conventional CZ single-crystal Nd:YAGs in the measured linewidths, line energies, and the energy-level structures for the Nd^{3+} ion constructed through the decomposition of the absorption and emission spectra. The line shape of the decomposed peaks is well expressed by Lorentzian, which indicates that the Nd ion site is unique in both the FZ single-crystal and the ceramic Nd:YAGs. Also from the decomposition, the induced emission cross sections of three FZ single crystals and the ceramic with 1-at.% Nd concentration are calculated to be 5.3, 7.0, 7.5, and 4.9 X 10^{-19} cm^2, respectively. These values are found to fall in the range of the reported values from 2.7 to 8.8 X 10^{-19} cm^2 for the CZ single crystals. The concentration quenching phenomenon is observed in the concentration dependence of the lifetimes of Nd:YAG ceramics with six different Nd concentrations, and found to be similar to that in the single crystals. The decay times of Nd(1%):YAGs at the 1064-nm laser wavelength are determined to be 226, 244, and 253 μs for the single crystals and 219 μs for the ceramic. The lifetime of the ceramic is slightly smaller than the reported values of 226 to 257 μs for the CZ single crystals and those measured for the FZ single crystals.

From these facts, we can conclude that the optical properties of the FZ single-crystal and ceramic Nd:YAGs are almost the same as those of the conventional CZ single-crystal Nd:YAGs. Thus, the FZ method may become an alternative technique of single-crystal growth to the conventional CZ method. On the ceramic Nd:YAG, we can conclude that the grains in the Nd:YAG ceramics are well crystallized and also comparable to the CZ and FZ single crystals.

Another subject is to study the basic optical spectra of the undoped and rare-earth-(Pr, Er, Nd, and Eu) doped transparent ceramic YAGs, since almost no investigation has been reported so far on the optically active ions in the transparent or translucent ceramics.

The absorption coefficient of the undoped YAG is found to be 0.258 cm^{-1} and almost independent of wavelength, whose value gives, for example, transmittance of 97.5 % for a disk of 1 mm thickness. The peaks in the absorption and emission spectra of the transparent rare-earth-doped ceramic YAGs have been assigned to the transitions in the corresponding $4f^n$ (n = 2, 3, 6, and 11) configurations. As for the Nd:YAG and Er:YAG ceramics, the Stark splitting schemes of Nd^{3+} and Er^{3+} ions have been compared with those reported for the Nd:YAG and Er:YAG single crystals. The observed splittings are in fair agreement with the reported ones calculated by the crystal-field calculations for the single crystals.

In the Pr:YAG ceramic, the transitions from the multiplets with total angular momentum J = 0 to those with even J momentum are observed to be strong as predicted by the Judd-Ofelt theory. Another Nd:YAG ceramics was prepared under improved synthetic conditions and the background absorption (attenuation) coefficient has been considerably reduced from 3.5-4 to 1.2 cm^{-1}. The overall and detailed spectroscopic features of the Nd:YAG ceramic used for the above-mentioned optical studies is exactly the same as those of the ceramics prepared earlier. The population inversion threshold of the ceramic is calculated and found to be about 25 times larger than that of the single-crystal. Although the background absorption coefficient is reduced considerably by the improved synthesis, it is concluded that the value is still large to realize a comparable ceramic laser to the single-crystal Nd:YAG laser.

On the Er:YAG ceramic, the transition energies agree well with those reported for the single-crystal Er:YAG and the other hosts within 30 cm^{-1}. The transition energies in the absorption and emission spectra of the Eu:YAG ceramic are found to be in very good agreement with those of the single crystal within 3 and 8 cm^{-1}, respectively. A broadband absorption is observed at around 280 nm. This band is presumably due to the f-d transition of the divalent Eu ion. However, further experiments in the ultraviolet- and vacuum-ultraviolet-wavelength region are necessary to elucidate the origin of the broadband absorption.

From this study, a quantitative basis has been provided for the procedure of the studies on Nd ion laser materials through the optical spectroscopic method currently used widely in the world; at first, to synthesize Nd-doped single crystals with varying the Nd concentrations by the FZ method which requires far shorter time to prepare single-crystal than the CZ method, to determine the optimum Nd concentration by evaluating the crystals through the optical spectroscopic measurements, and finally to grow a large scale single crystal by the conventional CZ method for actual laser oscillation experiments.

On the transparent ceramic YAGs, the detailed optical investigation is carried out for the first time in this work. Although we can conclude that the basic optical properties of the rare-earth ions in the transparent YAG ceramics are almost the same as those in the corresponding single crystals, the research on the transparent ceramics is even at the beginning stage. Therefore, much more investigations are expected to be done to elucidate the detailed optical properties and relevant electronic structures of optically active ions in the transparent ceramics such as systematic studies on the relationship between spectroscopic properties and synthetic conditions, investigation of the effect of the grain boundary on the background absorption, etc.

References

1. J.E. Geusic, H.M. Marcos, and L.G. van Uitert, *Appl. Phys. Lett.* 4,182 (1964).

2. K. Kitamura, S. Kimura, and K. Watanabe, *J. Cryst. Growth* 57, 475 (1982).

3. S. Kimura and I. Shindo, *J. Cryst. Growth* 41, 192 (1977).

4. S. Kimura, *Res. Rep. on High Performance Laser Sensing System,* p.40, S.T.A. (1985) (in Japanese).

5. R.L. Coble, *U.S. Patent* 3026210 (1962).

6. C. Greskovich and J.P. Chernoch, *J. Appl. Phys.* 44, 4599 (1973).

7. G.H. Haertling and C.E. Land, *J. Amer. Ceram. Soc.* 54, 1 (1971).

8. G.E. Gazza and S.K. Dutta, *U.S. Patent* 3767745 (1973).

9. G. de With and H.J.A. van Dijk, *Mat. Res. Bull.* 19, 1669 (1984).

10. C.A.M. Mulder and G. de With, *Solid State Ionics,* 16, 81 (1985).

11. G. de With and J.E.P. Parren, *Solid State Ionics,* 16, 87 (1985).

12. G. de With, *Philips J. Res.* 42, 119 (1987).

13. H. Haneda, S. Shirasaki, S. Matsuda, A. Watanabe, Y. Matsumoto, and T. Yanagitani, *Jpn. Patent Pending,* 63-242890 (1988).

14. H. Haneda, S. Shirasaki, S. Matsuda, A. Watanabe, M. Sekita, T. Kuroki, and T. Yanagitani, *Jpn. Patent Pending,* 1-106664 (1989).

15. T. Kushida, H.M. Marcos, and J.E. Geusic, *Phys. Rev.* 167, 289 (1968).

16. W. Tolksdorf, *Landorf-Börnstein*, ed. by K.-H. Hellwege and A.M. Hellwege, (Springer, Berin, 1978), 10, 1.

17. T.H. Mainman, *Brit. Commun. Electron.* 7, 674 (1960).

18. Z.J. Kiss and R.C. Duncan, *Appl. Phys. Lett.* 5, 200

(1964).

19. E. Okamoto, M. Sekita, and H. Masui, *Phys. Rev.* B11, 5103 (1975); review on the energy transfer phenomena is given in, for example, E. Okamoto, *Ph. D. Thesis, Osaka University*, (1975).

20. K.W.H Stevens, *Proc. Phys. Soc. (London)* A **65**, 209 (1952).

21. R.J. Elliott and K.W.H. Stevens, *Proc. Roy. Soc. (London)* A **218**, 553 (1953).

22. B.R. Judd, *Proc. Roy. Soc. (London)* A **227**, 552 (1955).

23. E.H. Erath, *J. Chem. Phys.* **34**, 1985 (1961).

24. J.D. Axe and G.H. Dieke, *J. Chem. Phys.* **37**, 2364 (1962).

25. J.C. Eisenstein, *J. Chem. Phys.* **39**, 2128 (1963).

26. W. Krupke and J.B. Gruber, *J. Chem. Phys.* **39**, 1024 (1963).

27. W. Krupke and J.B. Gruber, *J. Chem. Phys.* **41**, 1225 (1964).

28. J.A. Koningstein and J.E. Geusic, *Phys. Rev.* **136**, A711 (1964).

29. J.A. Koningstein, *Phys. Rev.* **136**, A717 (1964).

30. J.A. Koningstein and J.E. Geusic, *Phys. Rev.* **136**, A726 (1964).

31. K.H. Hellwedge, S. Hüfner, M. Schinkman, and H. Schmidt, *Phys. Kondens. Mat.* **4**, 397 (1966).

32. P. Porcher and P. Caro, *J. Chem. Phys.* **65**, 89 (1976).

33. M. Wardzynska and B.M. Wanklyn, *Phys. Status Solidi* A **40**, 663 (1977).

34. S. Geller and M.A. Gillo, *J. Phys. Chem. Solids* **3**, 30 (1957).

35. F. Sayetat, *J. Appl. Phys.* **46**, 3619 (1975).

36. J.F. Dillon, Jr. and L.R. Walker, *Phys. Rev.* **124**, 1401 (1961).

37. R.A. Buchanan, K.A. Wickersheim, J.J. Pearson, and G.F.

Herrmann, *Phys. Rev.* **159**, 245 (1967).

38. J.J. Pearson, G.F. Herrmann, K.A. Wickersheim, and R.A. Buchanan, *Phys. Rev.* **159**, 251 (1967).

39. P. Grünberg, S. Hüfner, E. Orlich, and J. Schmitt, *Phys. Rev.* **184**, 285 (1969).

40. V. Nekvasil, *J. Phys. C Solid State Phys.* **7**, L246 (1974).

41. C.A. Morrison, D.E. Wortman, and N. Karayianis, *J. Phys. C Solid State Phys.* **9**, L191 (1976).

42. V. Nekvasil, *Phys. Status Solidi* B **87**, 317 (1978).

43. S. Hüfner, *Optical Spectra of Transparent Rare Earth Compounds* (Academic Press, New York, 1978), p.64.

44. V. Nekvasil, *Phys. Status Solidi* B **94**, K41 (1979).

45. M. Sekita, *J. Luminesc.* **22**, 335 (1981).

46. W.M. Yen, W.C. Scott, and A.L. Schawlow, *Phys. Rev.* **136**, A271 (1964).

47. T. Kushida, *Phys. Rev.* **185**, 500 (1969).

48. B. DiBartolo, *Optical Interactions in Soilds* (Wiley, New York, 1968), Chapter 15; and the references in the literature.

49. J.M. Pellegrino and W.M. Yen, *Phys. Rev.* **B24**, 6719 (1981).

50. M.T. Hutchings and W.P. Wolf, *J. Chem. Phys.* **41**, 617 (1964).

51. J.S. Stroud, *Appl. Opt.* **7**, 751 (1968).

52. W.D. Partlow and H.W. Moos, *Phys. Rev.* **157**, 252 (1967).

53. M.J. Weber, *Phys. Rev.* **156**, 231 (1967).

54. M.J. Weber, *Phys. Rev.* **157**, 262 (1967).

55. L.A. Reiseberg, W.B. Gandrud, and H.W. Moos, *Phys. Rev.* **159**, 262 (1967).

56. L.A. Reiseberg and H.W. Moos, *Phys. Rev. Lett.* **19**, 1423 (1967).

57. M.J. Weber, *Phys. Rev.* **171**, 283 (1968).

58. L.A. Reiseberg and H.W. Moos, *Phys. Rev.* **174**, 429 (1968).

59. G.M. Zverev, G. Ya. Kolodnyi, and A.M. Onishchenko, *Sov.*

Phys. JETP, 33, 497 (1971).

60. T. Förster, *Z. Naturforsch.* **49**, 321 (1949).

61. D.L. Dexter, *J. Chem. Phys.* **21**, 836 (1953).

62. H.G. Danielmeyer and M. Blätte, *Appl. Phys.* **1**, 269 (1973).

63. B.R. Judd, *Phys. Rev.* **127**, 750 (1962).

64. G.S. Ofelt, *J. Chem. Phys.* **37**, 511 (1962).

65. R.K. Watts, *J. Opt. Soc. Amer.* **61**, 123 (1971).

66. W.F. Krupke, *IEEE J. Quantum Electron.* **QE7**, 153 (1971).

67. M. Birnbaum and J.A. Gelbwachs, *J. Appl. Phys.* **43**, 2335 (1972).

68. J.K. Neeland and V. Evtuhov, *Phys. Rev.* **156**, 244 (1967).

69. S. Singh, R.G. Smith, and L.G. Van Uitert, *Phys. Rev.* **B10**, 2566 (1974).

70. P. Mauer, *Appl. Opt.* **3**, 433 (1964).

71. R.V. Alves, R.A. Buchanan, K. Wickersheim, and E.A.C. Yates, *J. Appl. Phys.* **42**, 3043 (1971).

72. M. Birnbaum, A.W. Tucker, and C.L. Fincher, *J. Appl. Phys.* 52, 1212 (1981).

73. U. Deserno, D. Röss, and G. Zeidler, *Phys. Lett.* **28A**, 422 (1968).

74. R.W. Wallace and S.E. Harris, *Appl. Phys. Lett.* **15**, 111 (1969).

75. T. Kushida and J.E. Geusic, *Phys. Rev. Lett.* **21**, 1172 (1968).

76. R.P. Poplawsky and J.E. Tomas, *Rev. Sci. Instr.* **31**, 1303 (1960).

77. K. Kitazawa, K. Nagashima, T. Mizutani, K. Fueki, and T. Mukaibo, *J. Cryst. Growth* **39**, 211 (1977).

78. J.S. Shah and H.H. Wills, *Crystal Growth*, ed. by B.R. Pamplin, (Pergamon, Oxford, 1975), p.326.

79. I. Shindo, N. Kimizuka, and S. Kimura, *Mater. Res. Bull.* 11, 637 (1976).

80. S. Kimura, I. Shindo, K. Kitamura, Y. Mori, and H. Takamizawa, *J. Cryst. Growth* **44**,6211 (1978).

81. K. Kitamura, N. Ii, I. Shindo, and S. Kimura, *J. Cryst. Growth* **46**, 277 (1979).

82. I. Shindo, N. Ii, K. Kitamura, and S. Kimura, *J. Cryst. Growth* **46**, 307 (1979).

83. K. Kitamura, S. Kimura, and S. Hosoya, *J. Cryst. Growth* **48**, 469 (1980).

84. H.M. O'Bryan, Jr. and P.B. O'Connor, *Cer. Bull.* **45**, 571 (1966).

85. W. Class, *J. Cryst. Growth* **3/4**, 241 (1968).

86. C.A. Buruss and J. Stone, *Appl. Phys. Lett.* **26**, 318 (1975).

87. A.M. Balbashov and S.K. Egorov, *J. Cryst. Growth* **52**, 479 (1981).

88. M. Sekita and S. Kimura, *J. Appl. Phys.* **54**, 3415 (1983).

89. M.W. Benecke, N.O. Olson, and J.A. Pask, *J. Amer. Ceram. Soc.* **50**, 365 (1967).

90. Y. Moriyoshi, O. Maruyama, T. Ikegami, H. Yamamura, A. Watanabe, and S. Shirasaki, *Z. Phys. Chemie Neue Folge* **122**, 225 (1980).

91. Y. Moriyoshi, O. Maruyama, T. Ikegami, H. Yamamura, and A. Watanabe, *Z. Phys. Chemie Neue Folge* **125**, 107 (1981).

92. P.J. Jorgensen and R.C. Anderson, *J. Amer. Ceram. Soc.* **50**, 553 (1967).

93. C. Greskovich and K.N. Woods, *Cer. Bull.* **52**, 473 (1973).

94. R.J. Bratton, *J. Amer. Ceram. Soc.* **57**, 283 (1874).

95. B.E. Yoldas, *Cer. Bull.* **54**, 286 (1975).

96. H. Yamamura, S. Kuramoto, H. Haneda, A. Watanabe, and S. Shirasaki, *Yogyo-kyokai-shi*, **94**, 470 (1986) (in Japanese).

97. H. Yamamura, S. Kuramoto, H. Haneda, A. Watanabe, and S. Shirasaki, *Yogyo-kyokai-shi*, **95**, 545 (1986) (in Japanese).

98. H. Yamamura, H. Nakanishi, S. Shirasaki, and M. Sugimoto,

NIRIM Rep. **49**, 9 (1986) (in Japanese).

99. H. Haneda, *NIRIM Rep.* **49**, 38 (1986) (in Japanese).

100. Y. Moriyoshi, *NIRIM Rep.* **49**, 50 (1986) (in Japanese).

101. S. Matsuda, *NIRIM Rep.* **49**, 56 (1986) (in Japanese).

102. A. Watanabe, *NIRIM Rep.* **50**, 48 (1987) (in Japanese).

103. M. Sekita and T. Kobayashi, *Phys. Status Solidi* A **73**, 61 (1982).

104. R.L. Jennrich and P.F. Sampson, *Technometrics* **10**, 63 (1968).

105. S. Singh, W.A. Bonner, W.H. Grodkiewicz, M. Grass, and L.G. van Uitert, *Appl. Phys. Lett.* **29**, 343 (1976).

106. M. Sekita, A. Fujimori, A. Makishima, T. Shimohira, and H. Ohashi, *J. Non-Cryst. Solids* **76**, 399-407 (1985).

107. H. Ohashi and M. Sekita, *J. Jpn. Assoc. Min. Petr. Econ. Geol.* **77**, 455-459 (1982).

108. H. Ohashi and M. Sekita, *J. Jpn. Assoc. Min. Petr. Econ. Geol.* **78**, 239-245(1983).

109. M. Sekita, H. Ohashi, and S. Terada, *Phys. Chem. Minerals* **15**, 319-322 (1988).

110. P. Mauer, *Appl. Opt.* **3**, 433 (1964).

111. J. Nakano, K. Kubodera, T. Yamada, and S. Miyazawa, *J. Appl. Phys.* **50**, 6492 (1979).

112. W.L. Bond, *J. Appl. Phys.* **36**, 1674 (1965).

113. Kh.S. Bagadasarov and A.A. Kaminskii, *JETP Lett.* **9**, 303 (1969).

114. M.J. Weber and T.E. Varitimos, *J. Appl. Phys.* **42**, 4996 (1971).

115. A. Yariv, *Quantum Electronics* (Wiley, New York, 1975), p. 141.

116. C.J. Kennedy and J.D. Barry, *Appl. Phys. Lett.* 31, 91 (1977).

117. T.S. Lomheim and L.G. DeShazer, *J. Opt. Soc. Amer.* **68**, 1575 (1978).

118. R.C. Powell, D.P. Neikrik, and D. Sarder, *J. Opt. Soc. Amer.* **70**, 486 (1980).

119. A. Rosencwaig and E.A. Hildum, *Phys. Rev.* **B23**, 3301 (1981).

120. H.P Christensen, D.R. Gabbe, and H.P. Jensen, *Phys. Rev* **B25**, 1467 (1982).

121. M. Sekita, H. Haneda, T. Yanagitani, and S. Shirasaki, *J. Appl. Phys.* **67**, 453 (1990).

122. L.D. Landau and E.M. Lifshitz, *Electromagnetism of Continuous Media* (Pergamon, Oxford, 1975), p.272.

123. M.J. Weber, private communication.

124. E.D. Doran, *J. Chem. Phys.* **44**, 2910 (1966).

125. W.W. Piper, J.A. DeLuca, and F.S. Ham, *J. Luminesc.* **8**, 344 (1974).

126. H.H. Caspers and H.E. Rast, *J. Luminesc.* **10**, 347 (1975).

127. L. Esterowitz, F.J. Bartoli, and R.E. Allen, *J. Luminesc.* **21**, 1 (1979).

128. G.M. Renfro, J.C. Windscheif, and W.A. Sibley, *J. Luminesc.* **22**, 51 (1980).

129. J. Chrysochow, P.W.M. Jacobs, and M.J. Stillman, *J. Luminesc.* **28**, 177 (1983).

130. T. Hoshina, *Sony Research Center Reports*, *Supplement* (SONY Corporation, Yokohama, 1983) (in Japanese).

131. M. Malinowski, R. Wolski, and W. Wolinski, *J. Luminesc.* **35**, 1 (1986).

132. M. Sekita, H. Haneda, S. Shirasaki, and Yangitani, *J. Appl. Phys.* **69**, 3709 (1991).

133. A. Yariv, *Quantum Electronics* (Wiley, New York, 1975), p. 179.

134. W.T Canall, P.R. Fields, and R. Sarup, *J. Chem. Phys.* **57**, 43 (1972).

135. P. Kisliuk, W. Krupke, and J.B. Gruber, *J. Chem. Phys.* **40**, 3606 (1964).

136. N.C. Chang, J.B. Gruber, R.P. Leavitt, and C.A. Morrison, *J. Chem. Phys.* **76**, 3877 (1982).

137. M.V. Petrov and A.M. Tgachuk, *Opt. Spectrosc.* **45**, 81 (1979).

138. G.F. Koster, J.O. Dimmock, R.G. Wheeler, and H. Statz, *Properties of the thirty-two point group* (M.I.T. Press, Cambridge, 1963).

139. F.J. Avella, O.J. Sovers, and C.S. Wiggins, *J. Electrochem. Soc.* **114**, 613 (1967).

140. N.C. Chang, *J. Appl. Phys.* **34**, 3500 (1963).

141. K.A. Wickersheim and R.A. Lefever, *J. Electrochem. Soc.* **111**, 47 (1964).

142. C. Brecher, H. Samelson, R. Riley, and A. Lempicki, *J. Chem. Phys.* **49**, 3303 (1968).

143. A. Bril and W.L. Wanmaker, *J. Electrochem. Soc.* **111**, 1363 (1964).

144. G. Blasse and A. Bril, *J. Chem. Phys.* **45**, 3327 (1966).

145. C.K. Jørgensen, R. Pappalardo, and E. Rittershaus, *Z. Naturforsch.* **20a**, 54 (1964).

146. G. Blasse, *Solid State Commun.* **4**, 373 (1966).

147. G. Blasse, *J. Chem. Phys.* **45**, 2356 (1966).

148. G. Blasse, *J. Solid State Chem.* **4**, 52 (1972).

149. R.C. Ropp, *J. Electrochem. Soc.* **115**, 841 (1968).

150. E. Nakazawa and F. Shiga, *J. Luminesc.* **15**, 255 (1977).

151. G. Blasse, W.L. Wanmaker, J.W. ter Vrugt, and A. Bril, *Philips Res. Rep.* **23**, 189 (1968).

152. G. Blasse, A. Bril, and J. de Vries, *J. Inorg. Nucl. Chem.* **31**, 568 (1969).

153. K. Machida, G. Adachi, and J. Shiokawa, *J. Luminesc.* **21**, 101 (1979).

154. K. Machida, G. Adachi, J, Shiokawa, M. Shimada, and M. Koizumi, *J. Luminesc.* **21**, 233 (1980).

Acknowledgement

The author would like to express his most sincere gratitude to Prof. T. Kushida for critical reading of this manuscript and stimulating discussions. Discussions with Dr. K. Era were especially invaluable. It is pleasure to give specials thanks to Prof. S. Ibuki and the members of the old Ibuki Laboratory, especially Dr. K. Sato and Dr. H. Masui. He would like to thank Dr. N. Kimizuka, Dr. T. Chiba, Dr. T. Akahane, and Dr. T. Gomibuchi for their encouragements during this investigation.

The author is indebted to Dr. S. Kimura, Dr. Y. Miyazawa, Dr. H. Haneda, and Mr. T. Yanagitani for preparing the single crystals and the transparent ceramics. His thanks are also extended to his colleagues in his institute who helped directly and indirectly to this research.